TOWARD A PRECISION COSMOLOGICAL TEST OF GRAVITY FROM REDSHIFT-SPACE BISPECTRUM BASED ON PERTURBATION THEORY

A DISSERTATION

SUBMITTED TO THE DEPARTMENT OF PHYSICS,

KYOTO UNIVERSITY

IN PARTIAL FULFILLMENT OF THE REQUIREMENTS

FOR THE DEGREE OF

DOCTOR OF SCIENCE

By

Ichihiko Hashimoto

January 17, 2018

Acknowledgments

In the first place, I would like to express the deepest appreciation to my supervisor Associate Prof. Atsushi Taruya for his continuous encouragements and advices. He introduces me to the field of observational cosmology, and shows what the researcher is from his attitude for the research. He helps me for the every aspect of my Ph.D.course and gives a lot of contributions to complete my work. I also express my sincere gratitude for Yann Rasera for providing the data of N-body simulation. Without his generous support on simulation technique and productive discussion, this thesis would not have been possible. I have greatly benefited from Takahiro Nishimichi. He teaches me the skills of simulation, and gives me the useful codes which is indispensable for this thesis. I would like to acknowledge my collaborators, Shuichiro Yokoyama, Shuntaro Mizuno, Takahiko Matsubara and Toshiya Namikawa for their helps and valuable discussions. I also appreciate insightful comments and suggestions by Stéphane Colombi, Takashi Ishikawa and Shun Saito. I would like to offer my thanks to all the member in the Yukawa Institute for Theoretical Physics (YITP) and the Theoretical Astrophysics Group of Kyoto University for providing me a comfortable research environment. In particular, I share the most of time of my Ph.D.course with Joseph Matthew Fedrow, Guillem Doménech, Hidekazu Tsukiji, Shyuichi Yokoyama and Yuki Kamiya in office K501 and Ippei Obata, Mao Iwasa and Tatsuya Matsumoto in the seminar or colloquium. They always work very hard, and it encourage me quite a lot.

Numerical computation of this thesis were in part carried out on Cray XC30 at Center for Computational Astrophysics, CfCA, of National Astronomical Observatory of Japan and XC40 at YITP in Kyoto University.

Finally, I wish to specially thank my family for their endless support and encouragement.

Abstract

Despite the success of the standard cosmological model that consistently explains the observation of the cosmic microwave background and large scale structure traced by galaxies, cosmology still faces several fundamental problems. One such problem is the origin of late-time cosmic acceleration. To clarify this, in precision cosmology era, a gigantic data will be obtained from upcoming surveys, and measurement of statistical quantities will be made very precisely. Toward future cosmological analysis, improving the accuracy of theoretical template is rather essential for robust constraint and/or parameter estimation.

So far, the cosmological constraints on gravity and/or dark energy, obtained from large-scale structure observations, has been mainly made with the theory and measurement of the two-point statistics. However, the large-scale galaxy distribution in the late-time universe exhibits gravity-induced non-Gaussianity, and the bispectrum, three-point cumulant is expected to contain significant cosmological informations together with power spectrum. In particular, the measurement of the bispectrum helps to tighten the constraints on dark energy and modified gravity through the redshift-space distortions (RSD). In this thesis, extending the work by Taruya, Nishimichi & Saito (2010, Phys.Rev.D **82**, 063522), we present a perturbation theory (PT) based model of redshift-space bispectrum that can keep the non-perturbative damping effect under control. Characterizing this non-perturbative damping by a univariate function with single free parameter, the PT model of the redshift-space bispectrum is tested against a large set of cosmological N-body simulations, finding that the predicted monopole and quadrupole moments are in a good agreement with simulations at the scales of baryon acoustic oscillations (well beyond the range of agreement of standard PT). The validity of the univariate ansatz of the damping effect is also examined in the case of matter bispectrum, and with the PT calculation at next-to-leading order, the fitted values of the free parameter is shown to consistently match those obtained from the PT model of power spectrum by Taruya, Nishimichi & Saito (2010).

Toward a practical application of our template, we have also developed several techniques suited for cosmological data analysis, i.e., fast bispectrum estimation with fast Fourier transform and accelerated calculations for PT template. Applying these methods to the matter and halo catalogs and employing the Markov-chain Monte Carlo technique, we demonstrate that our improved bispectrum template reproduces the fiducial value of the growth rate, the key parameter to probe gravity on cosmological scales, well within 3% accuracy. Combining the bispectrum data with power spectrum data, the constraint on the growth rate is shown to be tightened, compared to the cases with power spectrum or bispectrum alone.

Contents

Acknowledgments **iii**

Abstract **iv**

1 Introduction **1**

2 A primer on standard cosmological model and observational effect **5**

2.1 Basics of the expanding universe 5

2.1.1 Basic equations 5

2.1.2 ΛCDM model 8

2.2 Linear theory for large scale structure formation 9

2.2.1 Generation and evolution of perturbations 10

2.2.2 Gravitational evolution of the perturbations 12

2.2.3 Transfer function 15

2.3 Redshift-space distortions 16

2.3.1 Redshift-space and real space 16

2.3.2 Kaiser effect 19

3 Non-linear theory of the evolution of large scale structure **20**

3.1 N-body simulation 20

3.1.1 Initial conditions 20

3.1.2 Solving the Poisson Equation 22

3.2 Standard perturbation theory 24

3.2.1 SPT in real space 24

3.2.2 SPT in redshift space 26

3.3 The perturbative calculation of power spectrum and bispectrum up to 1-loop level 28

3.4 Comparison between N-body simulation and SPT 30

4 Precision modeling of redshift-space bispectrum 32

4.1 Motivation 32

4.2 Exact formula of power spectrum and bispectrum in redshift space 35

4.3 An improved modeling of redshift-space bispectrum 37

4.4 Comparison with N-body simulations 43

4.4.1 N-body simulations and measurement of the bispectrum 43

4.4.2 Results in real space 46

4.4.3 Results in redshift space 49

4.4.4 Testing the ansatz of damping function 57

5 Testing improved bispectrum template against simulation catalogs 60

5.1 Fast measurement of the bispectrum 60

5.2 Fast calculation for improved bispectrum template 63

5.3 Constructing mock catalogs from N-body simulations 64

5.4 Likelihood Analysis 65

5.5 Results in matter fields 68

5.6 Results in halo fields 73

5.6.1 Linear bias model 75

5.6.2 Results 76

6 Discussion and conclusion 84

A Perturbative calculations for D_1 and D_2 terms 97

A.1 D_1 term 98

A.2 D_2 term 99

B Multipole expansion of redshift-space bispectrum 100

C Review of TNS model 102

Chapter 1 Introduction

Long time ago, clarifying the nature and history of the Universe has been limited to an armchair speculation. Over the last decade, observational cosmology as a physical science has been rapidly progressed thanks to the development of technology and improvement of the observational skills. One important milestone has been the establishment of the standard cosmological model that emerged very recently. The so-called Lambda cold dark matter (ΛCDM) model describes both the expansion history and structure formation of the Universe consistently only with 6 parameters. Now, with the improved measurement of cosmic microwave background anisotropies by Planck, the cosmological model parameters are tightly constrained, and the modern picture of the Universe has been further reinforced. The observations of large-scale structure through the galaxy redshift surveys such as Baryon Oscillation Spectroscopic Survey (BOSS) of Sloan Digital Sky Survey-III (SDSS-III) also provide a consistent result with prediction by ΛCDM model.

Despite the considerable successes of ΛCDM model, there nevertheless remain several fundamental problems. One such issue is the origin and nature of late-time cosmic acceleration, which has been first discovered by observations of distant type Ia supernovae. In the ΛCDM model, the cosmic acceleration is explained by the presence of mysterious energy component called dark energy. However, the nature of the dark energy has not yet been clarified. Alternatively, cosmic acceleration may be realized via the modification of gravity from General relativity (GR) on cosmological scales. The theory of gravity have been constrained at the scales from solar system [1] to cluster [2], and the constraints are consistent with GR in high precision. However, these constraints are still limited to small scale and constraints get weaker on large scales. In this respect, there still remains a wide range of parameter space for modified gravity models that are observationally viable. Further precision observation is thus essential to tightly constrain the possible deviation of gravity.

With the advent of precision cosmology era, ongoing and upcoming galaxy redshift surveys aim at measuring statistical quantities such as power spectrum and correlation function with unprecedented precision, which provide a way to perform a more severe test of gravity. In such a situation, of particular importance toward a robust cosmological data analysis is to

develop theoretical tools to accurately predict statistical quantities of large-scale structure, keeping any systematics and small uncertainties under control. Among various sources of systematics, nonlinear gravitational evolution is the most dominant physical effect in the large-scale structure observations, and the effect becomes significant as decreasing redshifts. This severely restricts the applicable range of the established linear theory of structure formation. On large scales accessible with on-goring and upcoming surveys, however, gravity evolution becomes mild, and an accurate theoretical model is made possible with analytic treatment with perturbation theory.

So far, the two-point statistics of galaxy clustering, i.e. power spectrum or two point correlation function, has been the major statistical quantities to constrain the cosmology with LSS observations. However, it is widely known that the nonlinearity of gravity generically incorporates the non-Gaussian statistical nature into the large-scale structures, and a part of the cosmological information initially encoded in the two-point statistics is leaked to the higher-order statistics. In this respect, the combination of the tree-point statistics, i.e. bispectrum or three point correlation function, with two-point statistics in the cosmological data analysis is a natural next step to efficiently extract the cosmological information from the large-scale structures.

Toward practical application of three-point statistics to the test of gravity, one has to develop theoretical template taking account of not only the nonlinear gravity but also the redshift-space distortions (RSD). Indeed, the cosmological test of gravity has been demonstrated by measuring the anisotropies of galaxy clustering induced by RSD. The RSD arises from the contamination of redshift measurement for each galaxy by the peculiar velocity of galaxies via Doppler effect. The RSD (e.g., Refs. [3, 4, 5, 6, 7]) manifestly, break the statistical isotropy, and make the statistical quantities anisotropic. While the RSD complicates the interpretation of the galaxy clustering data, it now attracts much attention as a probe of gravity on cosmological scales. This is because, on large scales, the effect is accounted by the linear theory, and the size of the anisotropies is related to the growth of structure (e.g., Refs. [4, 5]). Combining the RSD with the measurement of baryon acoustic oscillations (BAO), which is the characteristic pattern imprinted on galaxy clustering (e.g., [8, 9, 10]), we can simultaneously constrain both the geometric distances and growth of structure (e.g., [11, 12, 13, 14]), from which we are able to scrutinize the theory of gravity that accounts for cosmic expansion and structure formation (e.g., Refs. [15, 16, 17, 18, 19]).

Theoretically, RSD is described by the non-linear mapping formula from real to redshift

spaces. While the formula is simple, it involves the cross talk between small and large scales. Hence, modeling the RSD on the statistical quantities needs a careful investigation. In fact, writing the expression of redshift-space power spectrum in terms of real-space quantities, we will find a rather intricate statistical relation for which a naive perturbative calculation becomes inapplicable even at large scales. Hence, a sophisticated treatment of bispectrum is needed for a reliable theoretical template even in the weakly nonlinear regime [11, 20, 21, 22, 23, 24, 25, 26]. Although modeling the bispectrum with RSD effect has been already investigated based on fitting formula [27, 28] and halo model (e.g., Refs. [29, 30]), analytical treatment would be certainly powerful in characterizing the anisotropies of the bispectrum (see e.g., [31] for discussion on resummed purtavative treatment).

Primary goal of this thesis is to develop on improved bispectrum model based on the perturbative calculation at the next-to-leading order, called one-loop. Extending the work by Taruya, Nishimichi & Saito (2010) [11] on power spectrum we consistently incorporate the effect of small-scale virial motion into bispectrum. Albeit its limitation, the perturbative modeling deserves further consideration, and we present, for the first time, monopole and quadrupole moments of the redshift-space bispectrum at one-loop order, which agree well with N-body simulations at BAO scales. We qualitatively study the validity of our treatment on small-scale virial motion. Then, toward practical application of our improved PT template to further surveys, we develop a fast estimation method for redshift-space bispectrum and study how well one can accurately estimate the growth of structure using our improved model through mock catalog of matter and halo catalogs constructed with N-body simulations. Finally, we demonstrate the impact of combining power spectrum and bispectrum for constraining the gravity.

This thesis is organized as follows. In Chap. 2, we begin by reviewing the standard cosmological model and growth of structure in linear theory. we also describe the relation between real and redshift spaces, and derive the linear formula of power spectrum in redshift space. Then, in Chap. 3, we describe the treatment to deal with non-linear evolution of large scale structure, namely, N-body simulation and standard perturbation theory. Based on the standard perturbation theory, the expressions for redshift-space bispectrum at one-loop order are also presented. In Chap. 4, we present an improved PT model of redshift-space bispectrum. Writing down the exact formulas in terms of the cumulants, we follow the approach by Ref. [11], and develop the improved model of redshift-space bispectrum based on perturbation theory, which consistently includes both the one-loop order

perturbative corrections and non-perturbative damping effect coming from the small-scale virial motion. Our improved model is quantitatively tested against a large set of cosmological N-body simulations, and the validity of the assumption is checked in detail. In Chap. 5, toward future practical application of the improved model of redshift-space bispectrum developed in previous chapter to real galaxy surveys, we study how well we can get a robust and tight constraint on the growth rate parameter both from the power spectrum and bispectrum. We also present a fast estimation method for bispectrum. Finally, Chap. 6 is devoted to discussion and conclusion on our important findings.

Throughout the thesis, the speed of light is set to unity, $c = 1$.

Chapter 2 A primer on standard cosmological model and observational effect

In this chapter, we describe standard cosmological model and evolution of large scale structure (LSS) based on linear perturbation theory. We first review the background history and basic equations of the expanding universe. Then, we consider the linear evolution of matter fluctuation driven by gravity. As important observational systematics, we consider redshift-space distortions, which are crucial to interpret LSS data.

2.1 Basics of the expanding universe

2.1.1 Basic equations

In the theory of general relativity, space-time itself has the dynamical degree of freedom, and coevolve with energy components, such as dark-matter or radiation. Here we introduce basic equations to describe the homogeneous-isotropic universe. Space-time metric of the homogeneous-isotropic universe is given by the Robertson-Walker metric:

$$ds^2 = -dt^2 + a^2(t)\left[\frac{dr^2}{1-Kr^2} + r^2 d\Omega^2\right]. \tag{1}$$

Here, a and K represent the scale factor of the universe and spatial curvature, respectively. We define the comoving radial distance χ as follow:

$$d\chi \equiv \frac{dr}{\sqrt{1-Kr^2}}, \tag{2}$$

and then metric is rewritten with

$$ds^2 = -dt^2 + a^2(t)\left[d\chi^2 + S_K^2(\chi)^2(d\theta^2 + sin^2\theta d\phi^2)\right] \tag{3}$$

$$S_K(\chi) = \begin{cases} \frac{\sinh(\sqrt{-K}\chi)}{\sqrt{-K}} & (K<0) \\ \chi & (K=0) \\ \frac{\sin(\sqrt{K}\chi)}{\sqrt{K}} & (K>0). \end{cases} \tag{4}$$

Below, we normalize the scale factor a to unity at present time $a(t_0) = 1$, and consider the flat universe, i.e. $K = 0$. Then, the radial coordinate defined by $\int_t^{t_0} dt/a(t)$ is equal to a comoving distance χ.

The evolution of space-time metric is described by Einstein equation:

$$G^{\mu}_{\ \nu} + \Lambda\delta^{\mu}_{\ \nu} = 8\pi G T^{\mu}_{\ \nu}. \tag{5}$$

Left- and right-hand side of the equation describe the geometric structure of the space-time and energy-momentum components, respectively. Λ is the cosmological constant which can be regarded as a specific dark energy. In the homogeneous-isotropic universe, energy-momentum must have the form of perfect fluid:

$$T^{\mu}_{\ \nu} = \begin{pmatrix} -\rho & 0 & 0 & 0 \\ 0 & p & 0 & 0 \\ 0 & 0 & p & 0 \\ 0 & 0 & 0 & p, \end{pmatrix} \tag{6}$$

where, ρ is energy density and p is pressure. The property of the fluid including dark energy is characterized by its equation of state:

$$p = w\rho. \tag{7}$$

For non-relativistic matter components (i.e., cold dark matter and baryon), we have $w = 0$, and for relativistic components (i.e., radiation), we have $w = 1/3$. On the other hand, cosmological constant is equivalent to the fluid with $w = -1$. Substituting the Robertson-Walker metric Eq.(1) and energy-momentum tensor of perfect fluid Eq.(6) into Einstein equation Eq.(5), we obtain

$$\left(\frac{1}{a}\frac{da}{dt}\right)^2 = \frac{8\pi G}{3}\rho + \frac{\Lambda}{3}, \tag{8}$$

$$\frac{1}{a}\frac{d^2a}{dt^2} = \frac{4\pi G}{3}(\rho + 3p) + \frac{\Lambda}{3}. \tag{9}$$

Eq.(8) is called the Friedmann equation. On the other hand, from the conservation law of energy momentum tensor, $T^{\mu}_{\nu;\mu} = 0$, we obtain,

$$\frac{\partial\rho}{\partial t} = -3\frac{1}{a}\frac{da}{dt}(\rho + p), \tag{10}$$

which is compatible with Eqs.(8) and (9).

Eqs.(8),(9) and (10) imply that time evolution of scale factor is determined by the feature of energy density ρ. These equations are the basic equations for the homogeneous-isotropic universe which we want to explain in this section.

For the rest of this section, we introduce several useful parameters to describe the universe. To characterize the expansion rate of the universe, we introduce the Hubble parameter:

$$H \equiv \frac{1}{a}\frac{da}{dt}. \tag{11}$$

Hubble parameter gives the characteristic scale of the causally connected regions, i.e., the Hubble horizon. It is defined by

$$d_H(t) \equiv \frac{1}{H}. \tag{12}$$

The Hubble horizon gives the natural boundary above which the general relativistic treatment becomes important in describing evolution of matter fluctuations.

From Eq.(8), the total energy density of the present universe is described by

$$\rho_{\rm cr0} = \frac{3H_0^2}{8\pi G}, \tag{13}$$

where $\rho_{\rm cr0}$ is the critical energy density and H_0 is the Hubble parameter at present time. A dimensionless parameter h ($H_0 = 100\,h$ km s^{-1} Mpc^{-1}) is also used.

In terms of Hubble parameter, the Friedmann equation for the flat Universe composed of radiation, matter and cosmological constant is rewritten as,

$$H(z) = H_0\sqrt{a^4\Omega_{\rm r0} + a^{-3}\Omega_{\rm m0} + \Omega_{\Lambda 0}}, \tag{14}$$

where Ω_{i0} is the density parameter at present time is defined by:

$$\Omega_{\rm r0} \equiv \frac{8\pi G\rho_{\rm r0}}{3H_0^2}, \quad \Omega_{\rm m0} \equiv \frac{8\pi G\rho_{\rm m0}}{3H_0^2}, \quad \Omega_{\Lambda 0} \equiv \frac{\Lambda}{3H_0^2}. \tag{15}$$

which are respectively the density parameter of radiation, matter and cosmological constant. Note that the subscript 0 means the quantity at present time, and density parameter without the subscript 0 in general depends on time.

The time dependance of the energy density is determined from the conservation law and equation of state parameter w:

$$\rho_{\rm r} \propto a^{-4} \tag{16}$$

$$\rho_{\rm m} \propto a^{-3} \tag{17}$$

$$\rho_{\Lambda} \propto \text{constant} \tag{18}$$

Therefore, the dominant energy component of the universe changes in time. In standard cosmological model, the radiation component was dominant in the early time, but the radiation component decreases faster than other components. After the radiation-matter equality time, the matter component becomes dominant. At sufficiently late time, cosmological constant becomes dominant, and the universe eventually undergoes accelerated expansion. More generally, accelerated expansion is realized if the universe is filled with the energy component whose energy density and pressure satisfy $\rho + 3p < 0$. This energy component is called dark energy, and the cosmological constant is one of the dark energy. Currently, the origin and nature of dark energy are not yet clarified, and we just parametrize its energy density and equation-of-state similarly to a perfect fluid as follows:

$$\Omega_{\rm DE}(t) \equiv \frac{\rho_{\rm DE}(t)}{\rho_{\rm c}(t)}, \tag{19}$$

$$w_{\rm DE}(t) \equiv \frac{p_{\rm DE}(t)}{\rho_{\rm DE}(t)}. \tag{20}$$

From the Friedmann equation, the time dependance of scale factor is determined, and we obtain:

$$\text{Radiation dominant}: \quad a(t) \propto t^{1/2}, \tag{21}$$

$$\text{Matter dominant}: \quad a(t) \propto t^{2/3}, \tag{22}$$

$$\text{Dark energy dominant}: \quad a(t) \propto \exp(Ht). \tag{23}$$

2.1.2 ΛCDM model

The precision measurements of temperature anisotropies of cosmic microwave background (CMB), as well as large-scale structure, strongly support the ΛCDM model as the concordant cosmological model which consistently describe both the cosmic expansion and structure formation.

In the ΛCDM model, late-time cosmic acceleration is explained by the cosmological constant, and the baryon and cold dark matter (CDM) are the main constitution of the matter components:

$$\rho_{\rm m} = \rho_{\rm b} + \rho_{\rm c} \tag{24}$$

$$\Omega_{\rm b0} \equiv \frac{8\pi G\rho_{\rm b0}}{3H_0^2}, \quad \Omega_{\rm c0} \equiv \frac{8\pi G\rho_{\rm c0}}{3H_0^2}, \tag{25}$$

parameters	
$\Omega_{\rm b}h^2$	0.02230 ± 0.00014
$\Omega_{\rm c}h^2$	0.1188 ± 0.0010
H_0	67.74 ± 0.46
Ω_Λ	0.6911 ± 0.0062
$\Omega_{\rm m}$	0.3089 ± 0.0062
$n_{\rm s}$	0.9667 ± 0.0040

Table 1: Best fit values of the ΛCDM model obtained from Planck CMB power spectra, in combination with lensing reconstruction and external data (Type Ia supernovae and BAO) [32]. The error indicates the statistical uncertainty at 68% confidence limits.

where, we define Ω_{b0} and Ω_{c0} by the energy density of baryon $\rho_{\rm b}$ and CDM $\rho_{\rm c}$ in the flat universe. We consider the neutrino is massless and not included in matter component, because the neutrino mass is small enough and still undetected.

We summarize the current constraint on the cosmological parameters. Here, $n_{\rm s}$ is the spectrum index of initial power spectrum, which will be later introduced in Chap.2.2.

Fig. 1 shows the current constraint on the parameters of dark energy obtained from Planck, in combination with observation of type Ia supernovae and BAO [32]. The result of this figure assumes the time-dependent equation of state parameter for dark energy, given by

$$w_{\rm DE} = w_0 + (1 - a)w_a. \tag{26}$$

Current constraints on dark energy are consistent with cosmological constant (i.e., $w_{\rm DE} = -1$), as we already mentioned. The cosmological constant gives a simple solution to explain the late-time cosmic acceleration, however, we do not clearly know the reason why the cosmological constant is ridiculously so small, compared to the Planck energy. Rather, we may have to consider the possibility that the cosmic acceleration is not driven by the dark energy like cosmological constant, and the general relativity as underlying gravity theory does not hold on cosmological scales.

2.2 Linear theory for large scale structure formation

In this section, we discuss the basic properties of large-scale structure based on the linear theory of structure formation.

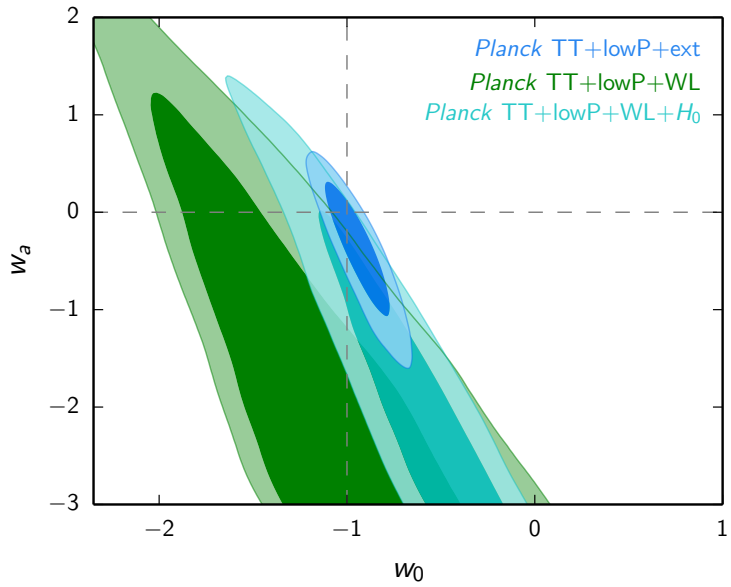

Figure 1: Current constraint on the dark energy equation of state parameters. This figure is taken from Ref. [32].

2.2.1 Generation and evolution of perturbations

The observation of CMB by Planck strongly supports that the universe had experienced accelerated expansion driven by the scalar field in the very early universe. This accelerated expansion is called inflation. The important point of the cosmic inflation is that during the accelerated expansion, a tiny density fluctuation as the seed of LSS is thought to be generated quantum mechanically.

Mechanism of Inflation and generation of perturbation

The scalar field which drives inflation is especially called inflaton. The simplest model of inflaton is given by the single-component real scaler field, $\phi(\boldsymbol{x})$. In this case, Lagrangian is given by [33]:

$$L = \int \sqrt{-g} d^4x \left[-\frac{1}{2} g^{\mu\nu} \partial_\mu \phi \partial_\nu \phi - V(\phi) \right], \tag{27}$$

where $V(\phi)$ is the potential. If we consider the homogeneous-isotropic universe as background space-time, Euler-Lagrange equation for scalar field becomes

$$\frac{\partial^2\phi}{\partial t^2} + 3H\frac{\partial\phi}{\partial t} + V'(\phi) = 0. \tag{28}$$

Here, ($'$) is the derivative with respect to ϕ. The energy-momentum tensor of inflaton is derived from Lagrangian Eq.(27) [33]:

$$T^{\mu}_{\ \nu} = g^{\mu\alpha}\frac{\partial\phi}{\partial x^{\alpha}}\frac{\partial\phi}{\partial x^{\nu}} - g^{\mu}_{\nu}\left[\frac{1}{2}g^{\alpha\beta}\frac{\partial\phi}{\partial x^{\alpha}}\frac{\partial\phi}{\partial x^{\beta}} + V(\phi)\right]. \tag{29}$$

The form of this energy-momentum tensor is identified with that of perfect fluid, $T^{\mu}_{\ \nu} = (\rho + p)u^{\mu}u_{\nu} + p\delta^{\mu}_{\ \nu}$, where the energy density and pressure correspond to

$$\rho_{\phi} = \frac{1}{2}\left(\frac{\partial\phi}{\partial t}\right)^2 + V(\phi), \tag{30}$$

$$p_{\phi} = \frac{1}{2}\left(\frac{\partial\phi}{\partial t}\right)^2 - V(\phi). \tag{31}$$

When the kinetic term is neglected, we obtain $\rho_{\phi} \simeq -p_{\phi}$. In this case, the potential energy of scalar field acts as cosmological constant, and Hubble parameter becomes constant from Eqs.(8) and (9):

$$\frac{d}{dt}H = \left(\frac{1}{a}\frac{da}{dt}\right)^2 - \frac{1}{a}\frac{d^2a}{dt^2} = 0, \tag{32}$$

then accelerated expansion is realized.

During the inflation, the quantum fluctuations of scalar field, coupled with the metric perturbation, were continuously generated at small scales. Because the comoving Hubble, $1/(aH)$, exponentially decreases, the microscopic fluctuation with wavenumber k eventually becomes super-horizon scale, i.e., $k/(aH) \ll 1$, and it can be regarded as a macroscopic classical fluctuation.

Perturbations after Inflation

After the inflation, the dominant energy component of the universe becomes radiation component, and the expansion rate of the universe is slowdown as shown in Eq.(21). On the other hand, the horizon becomes increased, $1/H(t) \propto t$, and thus the metric perturbation of mode-k generated during inflation re-enters into the horizon at late time, i.e., $k \gtrsim aH$. After the horizon re-entry, the density perturbation coupled with metric perturbation can grow in

the presence of CDM. However, at the radiation-dominant era, the growth of perturbations at sub-horizon scales is suppressed due to the strong radiation pressure. Therefore, growth of perturbations starts at the matter-dominant era, when the suppression by pressure is no longer effective.

Baryon acoustic oscillation

In ΛCDM model, the major part of matter component is CDM, but baryon is still important to understand the structure formation followed galaxy formation, and baryon fluctuation imprinted on LSS plays a crucial role in probing late-time cosmic expansion history. Compared to the CDM, the evolution of baryon density perturbation is complicated due to the coupling with radiation part. Before recombination, the universe is filled with the free electrons and protons. The free electrons are tightly coupled with photons by Thomson and Coulomb scatterings. Therefore, baryon and photon act as the single fluid, and baryon density perturbation can not grow in the presence of strong pressure by photon. This suppression continues until the decoupling of baryon and photon. The baryon-photon fluid exhibits acoustic modes, and the waves propagate inside the gravitational potential made by CDM. The time of the decoupling ($z \simeq 1100$) then comes after the radiation-matter equality ($z \simeq 2.4 \times 10^4 \Omega_{\mathrm{m}0} h^2$). After the decoupling, baryon density perturbation starts to grow in the presence of the CDM density perturbation, and subsequent evolution of baryon and CDM fluctuations finally results in observed LSS. One important consequence of the early-stage evolution is that the acoustic signature of the baryon-photon fluctuations remains imprinted on LSS even after the decoupling, and its characteristic scales determined by the sound horizon at decoupling time typically gives $\sim 100 h^{-1}$ Mpc, which can be used as a robust standard ruler. The so-called baryon acoustic oscillations can be a powerful tool to pin down the late-time cosmic expansion history, and thus the measurement of BAOs is now one of the important target in galaxy redshift surveys.

2.2.2 Gravitational evolution of the perturbations

As we already mentioned in previous section, the density perturbations basically start to grow at matter domination era. In this section, we will introduce the basic equation describing the dynamical evolution of density perturbations in matter or dark energy dominant era, and then show the analytic solution of the equations in linear regime.

Basic equations

First, we define matter density perturbation by the sum of density perturbation of CDM and baryon:

$$\delta_{\rm m}(\boldsymbol{x}, t) \equiv \frac{\rho_{\rm m}(\boldsymbol{x}, t) - \bar{\rho}_{\rm m}(t)}{\bar{\rho}_{\rm m}(t)}, \tag{33}$$

where, $\bar{\rho}_{\rm m}$ is the mean energy density of matter component. We also define the peculiar velocity field $\boldsymbol{v}$ as the derivative of comoving coordinate $\boldsymbol{x}$ with respect to the conformal time τ ($ad\tau \equiv dt$):

$$\boldsymbol{v} \equiv \dot{\boldsymbol{x}}, \tag{34}$$

where, $(\dot{})$ stands for the derivative with respect to the conformal time. Note that with this peculiar velocity, momentum is defined as $\boldsymbol{p} \equiv am\boldsymbol{v}$.

For our interest of the observed large-scale structure, the Newtonian treatment is sufficient to describe the late-time (nonlinear) evolution. This is basically true as long as we consider the subhorizon evolution. On cosmological scales, where hydrodynamic and radiative processes are irrelevant, the CDM and baryon are simply described as a collisionless self-gravitating system, whose governing equation is given by the Vlasov (or collisionless Boltzmann) equation coupled with Poisson equation. The one-particle distribution function by $f(\boldsymbol{x}, \boldsymbol{p}, \tau)$, the Vlasov equation is written as:

$$\frac{df}{d\tau} = \frac{\partial f}{\partial \tau} + \frac{\boldsymbol{p}}{am} \cdot \nabla f - am\nabla\Phi \cdot \nabla_{\boldsymbol{p}} f = 0. \tag{35}$$

The zeroth and first order moment of the function $f(\boldsymbol{x}, \boldsymbol{p}, \tau)$, are related to the spatial density and peculiar velocity fields:

$$\int d^3\boldsymbol{p} f(\boldsymbol{x}, \boldsymbol{p}, \tau) = \rho_{\rm m}(\boldsymbol{x}, \tau), \tag{36}$$

$$\int d^3\boldsymbol{p} \frac{\boldsymbol{p}}{am} f(\boldsymbol{x}, \boldsymbol{p}, \tau) = \rho_{\rm m}(\boldsymbol{x}, \tau)\boldsymbol{v}(\boldsymbol{x}, \tau). \tag{37}$$

The solution of the Vlasov equation generally yields a non-vanishing second- order moment of the distribution function, which is divided into two pieces:

$$\int d^3\boldsymbol{p} \frac{p_i p_j}{a^2 m^2} f(\boldsymbol{x}, \boldsymbol{p}, \tau) = \rho_{\rm m}(\boldsymbol{x}, \tau) v_i(\boldsymbol{x}, \tau) v_j(\boldsymbol{x}, \tau) + \sigma_{ij}(\boldsymbol{x}, \tau). \tag{38}$$

where σ_{ij} includes the anisotropic components of velocity dispersions. The CDM as well as baryon after the decoupling were initially cold with a virtually null local velocity dispersion, and follow the single-stream flow. Assuming this property also hold at late- time

evolution, we may set $\sigma_{ij} = 0$. Then, the zeroth and first order-moment equations gives a closed set of evolution eqs:

$$\dot{\delta}_{\rm m}(\boldsymbol{x},\tau) + \nabla\cdot[(1+\delta_{\rm m}(\boldsymbol{x},\tau))\boldsymbol{v}(\boldsymbol{x},\tau)] = 0, \tag{39}$$

$$\dot{\boldsymbol{v}} + \frac{\dot{a}}{a}\boldsymbol{v} + (\boldsymbol{v}\cdot\nabla)\boldsymbol{v} = -\nabla\Phi, \tag{40}$$

supplemented with Poisson equation:

$$\nabla^2\Phi = 4\pi G a^2\bar{\rho}_{\rm m}\delta_{\rm m}. \tag{41}$$

Eqs.(39) and (40) are respectively referred to as the equation of continuity and Euler equation. In the above, density field $\delta_{\rm m}$ and velocity field $\boldsymbol{v}$ are the quantities to be solved, but in the absence of vector metric perturbations, vorticity is irrelevant and we can impose irrotational velocity flow:

$$\nabla\times\boldsymbol{v} = 0. \tag{42}$$

This assumption is valid in the linear regime, because rotation mode of velocity field only has decaying mode. Therefore, velocity field is characterized only with its divergence: $\Theta \equiv \nabla\cdot\boldsymbol{v}$.

LINEAR-ORDER SOLUTION

Linearizing the Eqs.(39) and (40) in Fourier space, we obtain:

$$\dot{\delta}_{\rm L}(\boldsymbol{k},t) + \Theta_{\rm L}(\boldsymbol{k},t) = 0, \tag{43}$$

$$\dot{\Theta}_{\rm L}(\boldsymbol{k},t) + \frac{\dot{a}}{a}\Theta_{\rm L}(\boldsymbol{k},t) + \frac{6}{\tau^2}\delta_{\rm L}(\boldsymbol{k},t) = 0. \tag{44}$$

In the flat universe filled with matter and dark energy satisfying the equation of state, $p = w\rho$, the exact solution for linear perturbations is known. In this case, these equations are rewritten with [34]:

$$9(w+1)^2(1+y)y^2\delta_{\rm L}'' + 3\left[\frac{7}{2} + y\left(5 - \frac{3m}{2}\right)\right]y\delta_{\rm L}' - \frac{3}{2}\delta_{\rm L} = 0, \tag{45}$$

$$y \equiv \left(\frac{a}{a_d}\right)^{-3w}, \quad a_d \equiv a_0\left(\frac{\Omega_{m0}}{\Omega_{\Lambda 0}}\right)^{-1/3w}. \tag{46}$$

Here, $(')$ denotes the derivative with respect to the parameter y. The solution of this equation can be expressed by hypergeometric function, $F(a,b,c,d)$, and its growing mode is written

by [34]:

$$D \propto y^{1/3} F\left(-\frac{1}{3w}, -\frac{3(1-y)}{6w}, -\frac{5-6w}{6w}, -y\right). \tag{47}$$

On the other hand, the linear velocity perturbation is also obtained from Eq.(43):

$$\Theta_{\rm L}(\boldsymbol{k}) = -aHf\delta_{\rm L}(\boldsymbol{k}). \tag{48}$$

Here, we define linear growth rate $f(a)$ as:

$$f(a) \equiv \frac{d\ln D(a)}{d\ln a}. \tag{49}$$

2.2.3 Transfer function

In linear theory, density perturbation can evolve independently for individual mode k. In this respect, the shape of power spectrum remains unchanged in linear stage. However, this is true only after the mode re-enters the horizon. Indeed, the amplitude of density perturbation can be different depending on the time when the mode re-enters the Hubble horizon. This is because the fluctuations cannot grow inside the horizon during the radiation dominant epoch. As a result, the power spectrum deep inside the Hubble horizon at matter dominant epoch has a characteristic scale-dependence. To describe the scale-dependent nature of density fluctuations, it is convenient to introduce the transfer function, defined by:

$$T(k,t) \equiv \frac{D(t_{\rm f})}{D(t)}\frac{\delta_{\rm L}(\boldsymbol{k},t)}{\delta_{\rm ini}(\boldsymbol{k})}, \tag{50}$$

where $\delta_{\rm ini}(\boldsymbol{k})$ is the primordial density perturbations and $\delta_{\rm L}(\boldsymbol{k},t)$ is the density perturbations calculated by linear theory. The linear growth factor D represent the time dependence of density perturbations at matter/dark energy dominant epoch in linear regime. As shown in Fig. 2 the transfer function asymptotically scales as k^{-2} below $k_{\rm eq} \simeq 0.01(\Omega_{\rm m0}h^2/0.13)[h{\rm Mpc}^{-1}]$, which is determined by the horizon of radiation-matter equality.

Using transfer function, we can express the amplitude of late-time density perturbation linear density perturbation $\delta_{\rm L}$:

$$\delta_{\rm L}(k) = -M(k)\,\Phi_{\rm init}(k), \tag{51}$$

$$M(k) = \frac{2}{3}D(z)\frac{k^2T(k)}{H_0^2\Omega_{m0}}, \tag{52}$$

where, $\Phi_{\rm init}$ is the primordial curvature perturbation. Here, we consider the adiabatic initial condition, consistent with simple inflationary scenario. Here and in what follows, $D(t)$ is normalized to unity at current time.

Given the linear density field, we can compute the matter power spectrum defined by

$$(2\pi)^3\delta_{\rm D}(\boldsymbol{k}+\boldsymbol{k}')P(\boldsymbol{k}) \equiv \langle\delta_{\rm m}(\boldsymbol{k})\delta_{\rm m}(\boldsymbol{k}')\rangle, \tag{53}$$

From Eq.(51), linear matter power spectrum is expressed as follows:

$$P_{\rm L}(k) = M^2(k)P_\Phi(k). \tag{54}$$

Here, $P_\Phi(k)$ is the primordial power spectrum, defined by:

$$\langle\Phi_{\rm init}(k)\Phi_{\rm init}(k')\rangle = (2\pi)^3\delta_{\rm D}^{(3)}(\boldsymbol{k}+\boldsymbol{k}')P_\Phi(k). \tag{55}$$

The shape of primordial power spectrum is depend on the model of the perturbation generation. In usual, $P_\Phi(k)$ is assumed to be single power law,

$$P_\Phi(k) \propto k^{n_{\rm s}-4}. \tag{56}$$

Here, $n_{\rm s} \equiv \frac{d\ln P_\Phi(k)}{d\ln k} + 4$ is called the spectral index, and current constraint is summarized in Table 2.1.2. Note that, in the case of the simplest model of inflation, i.e. slow roll inflation, the predicted spectrum index is close to $n_{\rm s} \simeq 1$.

2.3 Redshift-space distortions

The redshift-space distortions are apparent anisotropies of large scale structure observed via spectroscopic measurement of galaxies. The effect is originated from the redshift measurement of each galaxy, and due to the Doppler effect induced by the peculiar velocity of galaxies, the galaxy clustering observed in redshift space appears distorted along the line-of-sight. Although RSD complicates the interpretation of LSS data, this effect is essential to test gravity on cosmological scales. In this section, we will describe the redshift-space distortions at cosmological scales, and derive the formula for power spectrum in linear regime.

2.3.1 Redshift-space and real space

In the spectroscopic measurement of galaxies, the distance along the line-of-sight is measured by the redshift z:

$$1 + z \equiv \frac{1}{a(t)}. \tag{57}$$

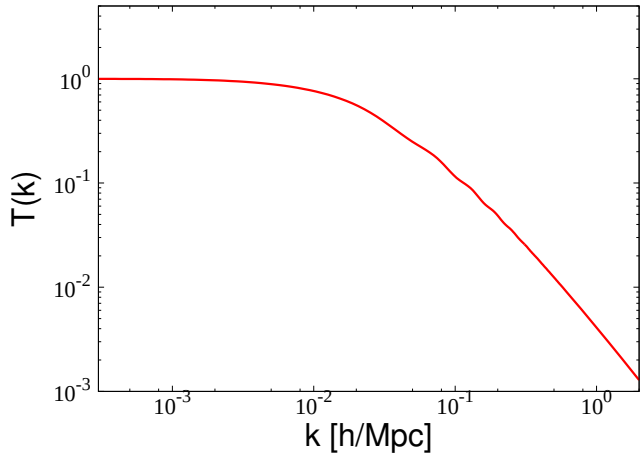

Figure 2: The scale dependence of transfer function based on ΛCDM model with $\Omega_{\rm m0} = 0.279$, $\Omega_{\rm b0} = 0.0462$, $\Omega_{\rm r0} = 8.48 \times 10^{-5}$ and $h = 0.7$. The matter radiation equality correspond to $k \sim 10^{-2} h\mathrm{Mpc}^{-1}$.

When we observe the light emitted at t from the emitter at rest in the comoving coordinate system, the wavelength of the light is redshifted by a factor of $1 + z$ due to the cosmic expansion. In the absence of gravitational lensing, the light trajectory is straight, and we have $d\Omega = 0$. Thus, the comoving distance between the observer and the object at redshift z is written by:

$$\chi = \int_t^{t_0} \frac{dt}{a(t)} = \int_a^1 \frac{da}{a^2 H} = \int_0^z \frac{dz}{H}. \tag{58}$$

Galaxy redshift surveys provides a three-dimensional view of galaxy distribution by measuring the angular position of each galaxy over the sky and redshift along the observer's line-of-sight direction. While the spectroscopic measurement determines the redshift, $z_{\rm obs}$, for each galaxy, the actual value does not properly reflects the cosmological redshift. Through the Doppler effect, the measured redshift is distorted by the peculiar velocity of galaxies:

$$1 + z_{\rm obs} \simeq (1 + z)\left(1 - v_{\parallel}(\boldsymbol{r})\right)^{-1}, \tag{59}$$

where $z_{\rm obs}$ is the observed redshift of the galaxies, $v_{\parallel}$ is the line-of-site component of the peculiar velocity, and we assume $v_{\parallel} \ll c$. With this relation, the observed space called redshift space generally differs from the actual space (real space). Substituting $z_{\rm obs}$ into

Eq.(58), the relation between (comoving) redshift and real spaces is given by

$$\boldsymbol{s} = \boldsymbol{r} + \frac{(1+z)v_{\parallel}(\boldsymbol{r})}{H(z)}\hat{r}, \tag{60}$$

Eq.(60) implies that even if the real space is isotropic, the observed galaxy clustering in redshift space become anisotropic in the presence of the second term of Eq.(60). Based on linear theory, a typical size of the second term is estimated to be $O(1)h^{-1}$Mpc at $\chi(z = 0.5) \simeq 1.32h^{-1}$Gpc.

Now, let us consider how the density field in redshift is related to that in real space. Denoting respectively the density perturbations in real and redshift spaces by $\delta(\boldsymbol{r})$ and $\delta^{(\mathrm{s})}(\boldsymbol{s})$, the mass conservation implies $\{1 + \delta^{(\mathrm{s})}(\boldsymbol{s})\}d^3\boldsymbol{s} = \{1 + \delta(\boldsymbol{r})\}d^3\boldsymbol{r}$, which leads to

$$\delta^{(\mathrm{s})}(\boldsymbol{s}) = \left|\frac{\partial \boldsymbol{s}}{\partial \boldsymbol{r}}\right|^{-1} \{1 + \delta(\boldsymbol{r})\} - 1. \tag{61}$$

Once we obtain Jacobian ($J \equiv |\partial \boldsymbol{r}/\partial \boldsymbol{s}|$), the density perturbations in redshift space is calculated from that in real space. From Eq.(60), Jacobian is calculated as:

$$J = \frac{r^2 dr}{s^2 ds} = \left\{1 - \frac{(1+z)v_{\parallel}}{H(z)r}\right\}^{-2} \left\{1 - \frac{(1+z)}{H(z)}\frac{\partial v_{\parallel}}{\partial r}\right\}^{-1}. \tag{62}$$

In what follows, we adopt the distant-observer and plane-parallel approximation to simplify the calculation. This approximation is reasonable and makes sense when the typical size of survey L is enough larger than the scale of interest, $\sim 1/k$, and sufficiently high redshift. In that region, the velocity term in the first bracket in Eq.(62) can be ignored by comparing to the velocity term in second bracket:

$$\frac{v_{\parallel}}{L} \ll k v_{\parallel}. \tag{63}$$

In addition, we can neglect the curvature of celestial sphere, and fix the line of sight direction to the specific $\hat{z}$ axis:

$$\hat{\boldsymbol{k}} \cdot \hat{\boldsymbol{x}} \simeq \hat{\boldsymbol{k}} \cdot \hat{\boldsymbol{z}}. \tag{64}$$

As a result, Jacobian is approximated to be:

$$J \simeq \left\{1 - \frac{(1+z)}{H(z)}\frac{\partial v_z}{\partial r}\right\}^{-1}. \tag{65}$$

Using Eq.(65), Fourier transform of the density field is given by

$$\delta^{(\mathrm{s})}(\boldsymbol{k}) = \int d\boldsymbol{r}^3 \left\{\delta(\boldsymbol{r}) - \frac{\nabla_z v_z(\boldsymbol{r})}{aH(z)}\right\} e^{i(k\mu v_z/aH + \boldsymbol{k}\cdot\boldsymbol{r})}, \tag{66}$$

where the variable μ is the directional cosine of the angle between the line-of-sight $\hat{\boldsymbol{z}}$ and wave vector $\boldsymbol{k}$, and v_z is line-of-sight component of the velocity field, $v_{\parallel} \simeq v_z \equiv \boldsymbol{v} \cdot \hat{\boldsymbol{z}}$.

2.3.2 Kaiser effect

In this section, we derive the formula for the redshift-space power spectrum in liner regime. Similarly to the real-space power spectrum, redshift-space power spectrum is defined by:

$$(2\pi)^3\delta_{\rm D}(\boldsymbol{k}+\boldsymbol{k}')P^{(\rm s)}(\boldsymbol{k}) \equiv \langle\delta^{(\rm s)}(\boldsymbol{k})\delta^{(\rm s)}(\boldsymbol{k}')\rangle, \tag{67}$$

On the other hand, linearizing Eq.(66), we use the linear relation Eq.(48) written by:

$$\delta_{\rm L}^{(\rm s)}(\boldsymbol{k}) = (1+f\mu^2)\delta_{\rm L}(\boldsymbol{k}), \tag{68}$$

where f is linear growth rate defined at Eq.(49). Substituting the linear density perturbation into Eq.(67), we obtain:

$$P_{\rm L}^{(\rm s)}(k,\mu) = (1+f\mu^2)^2 P_{\rm L}(k). \tag{69}$$

This is known as the Kaiser formula [4], and it indicates that on large scales, bulk flows falling toward overdense regions enhance the clustering of galaxies along the line-of-sight in redshift space. The strength of the anisotropy of Kaiser effect is proportional to the growth rate f. Its value and time dependence are basically determined by the theory of gravity on cosmological scales. In this respect, estimating observationally the growth rate offers an interesting opportunity to test gravity, and the measurement of RSD is now one of the main science goals in galaxy redshift surveys.

Chapter 3 Non-linear theory of the evolution of large scale structure

In this chapter, we describe the treatment of non-linear gravitational evolution of LSS based on both numerical simulation and analytic calculation. We first introduce the method of N-body simulation, which provides a non-perturbative way to trace the evolution of LSS. Then we describe the standard perturbative calculation of density perturbation in real space and redshift space.

3.1 N-body simulation

While the perturbation theory (PT) describes the non-linearity by perturbative expansion and is valid in weakly non-linear regime, the cosmological N-body simulation is powerful to investigate the cosmological structure formation deep inside fully non-linear regime. In the N-body simulation, we describe the gravitational evolution of LSS with N collisionless particles as the sample of particular realization of the phase-space distribution, $f(\boldsymbol{x}, \boldsymbol{v}, z)$, in a comoving periodic box.

To run the N-body simulation, we should provide the position and velocity data for each particle at a sufficiently early time where perturbation is tiny. Then we calculate the gravitational force of each particle and advance the positions and velocities according to Newton's equation of motion. We here describe the representative public codes, 2LPT and Gadget2, which we will use in Chap.5. Note that there are variety of methods to generate the initial condition from input linear power spectrum and to compute gravitational force. For example, RAMSES code [35] is the representative code for the Particle Mesh scheme on an adaptively refined grid (AMR), and MPGRAFIC [36] is used as the initial condition generator of RAMSES. The output results obtained from these codes will be also used in Chap.4.

3.1.1 Initial conditions

To generate initial condition of N-body simulation, we follow several steps described below. First, we place N-particles onto grids imposing periodic boundary condition. This

particle distribution is mostly uniform at the scales larger than the inter-particle distance. In reality, particle distribution should have characteristic inhomogeneities according to linear theory of structure formation. To create large-scale random inhomogeneities, we use the Lagrangian perturbation theory.

Historically, the Zel'dovich approximation as the first order Lagrangian perturbation has been frequently used as initial condition generator at an early development of N-body simulations, but to increase the prediction as well as to eliminate the initial transients, the second-order Lagrangian perturbation theory gets popular, and is used as the standard initial condition generator [37, 38].

The Lagrangian PT provides a way to describe the motion of mass elements in terms of the Lagrangian coordinate. The Lagrangian coordinate $\boldsymbol{q}$ and the Eulerian coordinate $\boldsymbol{x}$ of a particle at time t is related through:

$$\boldsymbol{x}(\boldsymbol{q}, t) = \boldsymbol{q} + \boldsymbol{\xi}(\boldsymbol{q}, t), \tag{70}$$

where, $\boldsymbol{\xi}(\boldsymbol{q}, t)$ is the displacement vector and we set $\boldsymbol{x}(\boldsymbol{q}, t = 0) = \boldsymbol{q}$. In the Lagrangian coordinate, the mass density is defined to be uniform. Then, the conservation of mass implies

$$\rho_{\rm m}(\boldsymbol{x}) d^3x = \bar{\rho}_{\rm m} d^3q, \tag{71}$$

where, $\bar{\rho}_{\rm m}$ is mean value of matter density. Using this relation, the perturbative displacement field is expressed in terms of the linear density field. To derive the explicit expressions, we rewrite the above equation with

$$1 + \delta_{\rm m}(\boldsymbol{x}) = \left| \frac{d\boldsymbol{x}}{d\boldsymbol{q}} \right|^{-1} = \int d^3q \delta_D^3(\boldsymbol{x} - \boldsymbol{q} - \boldsymbol{\xi}(\boldsymbol{q})). \tag{72}$$

Then, $\delta_{\rm m}$ is expressed as:

$$\begin{aligned} \delta_{\rm m}(\boldsymbol{k}) &= \int d^3x e^{-i\boldsymbol{k}\cdot\boldsymbol{x}} \int d^3q \delta_{\rm D}^{(3)}(\boldsymbol{x} - \boldsymbol{q} - \boldsymbol{\xi}(\boldsymbol{q})) - (2\pi)^3 \delta_{\rm D}^{(3)}(\boldsymbol{k}) \\ &= \int d^3q e^{-i\boldsymbol{k}\cdot(\boldsymbol{q}+\boldsymbol{\xi}(\boldsymbol{q}))} - (2\pi)^3 \delta_{\rm D}^{(3)}(\boldsymbol{k}). \end{aligned} \tag{73}$$

Substituting the expressions:

$$e^{-i\boldsymbol{k}\cdot\boldsymbol{\xi}(\boldsymbol{q})} = \sum_{m=0}^{\infty} \frac{1}{m!} (-i\boldsymbol{k} \cdot \boldsymbol{\xi}(\boldsymbol{q}))^m, \tag{74}$$

$$\boldsymbol{\xi}(\boldsymbol{q}) = \int \frac{d^3k}{(2\pi)^3} e^{i\boldsymbol{k}\cdot\boldsymbol{q}} \tilde{\boldsymbol{\xi}}(\boldsymbol{k}), \tag{75}$$

into Eq.(73), we obtain,

$$\delta_{\rm m}(\boldsymbol{k}) = \sum_{n\geq 1}^{\infty} \frac{(-i)^n}{n!} \int \frac{d^3k_1}{(2\pi)^3} \cdots \frac{d^3k_n}{(2\pi)^3} (2\pi)^3 \delta_{\rm D}^{(3)}(\boldsymbol{k}_{1\cdots n} - \boldsymbol{k}) \left[\boldsymbol{k}\cdot\tilde{\boldsymbol{\xi}}(\boldsymbol{k}_1)\right] \cdots \left[\boldsymbol{k}\cdot\tilde{\boldsymbol{\xi}}(\boldsymbol{k}_n)\right]. \quad (76)$$

In the Lagrangian perturbation theory, $\tilde{\boldsymbol{\xi}}$ is expanded in powers of $\delta_{\rm L}$:

$$\tilde{\boldsymbol{\xi}}(\boldsymbol{k}) = \sum_{n=1}^{\infty} \frac{1}{n!} \int \frac{d^3k_1}{(2\pi)^3} \cdots \frac{d^3k_n}{(2\pi)^3} (2\pi)^3 \delta_{\rm D}^{(3)}(\boldsymbol{k}_{1\cdots n} - \boldsymbol{k}) \boldsymbol{L}_n(\boldsymbol{k}_1, \cdots, \boldsymbol{k}_n) \delta_{\rm L}(\boldsymbol{k}_1) \cdots \delta_{\rm L}(\boldsymbol{k}_n), \quad (77)$$

where $\boldsymbol{k}_{12\cdots n} \equiv \boldsymbol{k}_1 + \boldsymbol{k}_2 + \cdots + \boldsymbol{k}_n$. The explicit expressions for the Lagrangian kernels $\boldsymbol{L}_n(\boldsymbol{k}_1, \cdots, \boldsymbol{k}_n)$ up to the second order are given by

$$\boldsymbol{L}_1(\boldsymbol{k}) = \frac{\boldsymbol{k}}{k^2}, \quad (78)$$

$$\boldsymbol{L}_2(\boldsymbol{k}_1, \boldsymbol{k}_2) = \frac{3}{7} \frac{\boldsymbol{k}_{12}}{k^2} \left[1 - \left(\frac{\boldsymbol{k}_1 \cdot \boldsymbol{k}_2}{k_1 k_2}\right)\right], \quad (79)$$

which can be derived easily using the expressions for standard PT kernels [see Eqs.(96),(97) and (100)]. Provided the expression displacement field, now, we can calculate the velocity field

$$\boldsymbol{v}(\boldsymbol{x}, t) = \frac{d\boldsymbol{\xi}(\boldsymbol{q}, t)}{dt}. \quad (80)$$

Finally, we summarize the prossedure of generating initial condition by second order Lagrangian theory (hereafter 2LPT) [37, 38]. First, we create the random initial density field on the grids, following the cosmological model which we want to simulate. Second, using the Fourier transformed quantity of Eq.(77), we calculate the displacement vector on each grid. With this vector, we displace the particle initially placed on each grid, and assign the velocity given by Eq.(80) to each particle.

In the N-body simulation of Chap.5, we employ 2LPT [37, 38] to generate initial conditions.

3.1.2 Solving the Poisson Equation

To evolve the density field represented by N particles, we employ a Tree-Particle-Mesh (Tree-PM) solver, Gadget2[39, 40]. The Tree-PM is a hybrid method combining two differential algorithms called Particle-Mesh (PM) algorithm and tree algorithm. In this section, we review the basic idea of these algorithms.

The straightforward treatment to evolve N particles is to compute gravitational forces for $N(N-1)/2$ pairs of particles directly. The force exerted on i-th particle is expressed as:

$$\Delta\Phi(\boldsymbol{x}_i) = -\frac{G}{a}\sum_{j\neq i} m_j \frac{\boldsymbol{x}_j - \boldsymbol{x}_i}{|\boldsymbol{x}_i|^3}. \tag{81}$$

The algorithm which solves this equation directly is called Particle-Particle (PP) algorithm. However, this algorithm takes $\sim O(N^2)$ operations at each time step, and in the case of cosmological simulation, huge amount of time is consumed due to the large N (e.g. we simulate $N = 1024^3$ particles in this thesis).

To overcome this problem, PM algorithm which uses fast Fourier transform (FFT) has been developed. In the PM algorithm, we firstly divide the space into grids and calculate density field at every grid point. Then, using FFT, we go to Fourier space to obtain the solution of potential. Because the number of operation of FFT is $O(N_{\rm mesh}\log N_{\rm mesh})$, the total number of operation of PM algorithm is $O(N) + O(N_{\rm mesh}\log N_{\rm mesh})$, which is much smaller than that of PP algorithm. If the distance between two particles becomes comparable to or smaller than mesh size, force calculation with PM algorithm becomes inaccurate, and we need to increase $N_{\rm mesh}$ to guarantee the accuracy.

Another method to reduce the number of operation is called tree algorithm. In this algorithm, we iteratively divide the simulation box into 8 small cells until each cell has one or zero particle. This hierarchy structure of cells is called tree. To reduce the computational cost, in computing the force, we treat particles in a distant cells as a single large particle if the cell satisfies the following condition:

$$d > \frac{s}{\theta} + \delta, \tag{82}$$

where, θ is a control parameter, d is the distance from the particle to the center of mass of the cell, s is the size of the cell and δ is the distance from the center of mass to the geometric center of the cell. We can improve the accuracy by increasing the value of θ. This treatment is reasonable because the contribution to the gravitational force from distant objects is smaller than that from the nearby objects. Approximating the gravitational force from long distance, we can reduce the number of operation to $O(N\log N)$. The disadvantage of this algorithm is requirement of large memory size to store not only the position and velocity of particles but also the structure of tree. In addition, when the density fluctuation is small, the accuracy of the algorithm become worse.

In the Tree-PM solver implemented in Gadget2, the code decomposes the gravitational potential into long-range and short-range parts in Fourier space [39]

$$\Phi(\boldsymbol{k}) = \Phi^{\rm long}(\boldsymbol{k}) + \Phi^{\rm short}(\boldsymbol{k}), \tag{83}$$

and then compute long-range part by PM and short-range part by tree algorithm. The long-range part is described by

$$\Phi^{\rm long}(\boldsymbol{k}) = \Phi(\boldsymbol{k}) \exp(-\boldsymbol{k}^2 x_{\rm s}^2), \tag{84}$$

with the spacial scale of force split $x_{\rm s}$, which is sufficiently smaller than the box size $x_{\rm s} \ll L$. On the other hand, short-range part is given by

$$\Phi^{\rm short}(\boldsymbol{k}) = -G\Phi(\boldsymbol{k}) \sum_i \frac{m_i}{x_i'} {\rm erfc}(-\boldsymbol{k}^2 x_{\rm s}^2), \tag{85}$$

where x_i' is the smallest distance of projection of particle i to the point $\boldsymbol{x}$, i.e. $x_i' = \min(|\boldsymbol{x} - \boldsymbol{x}_i - nL|)$.

3.2 Standard perturbation theory

At large scales ($\sim$ 100Mpc) non-linearity of gravitational evolution is rather mild, and the perturbation theory technique is quite powerful to understand the density and velocity perturbations. In this section, we describing the standard method to perturbatively solve the basic equations Eqs.(39)-(41) in real space. This perturbative treatment is referred to as the standard perturbation theory (SPT). Then we extend this SPT calculation to describe the density fields in redshift space.

3.2.1 SPT in real space

Let us first recall that the rotation mode of velocity fields can be neglected at an early phase of the structure formation. The velocity follows the potential flow, and the dynamics of perturbations is described by the density field and velocity-divergence field defined by:

$$\boldsymbol{u}(\boldsymbol{r}) = -\boldsymbol{v}(\boldsymbol{r})/\{faH(z)\}, \tag{86}$$

$$\theta \equiv \nabla \cdot \boldsymbol{u}. \tag{87}$$

Using θ, Fourier transform of Eqs.(39)-(41) leads to

$$\dot{\delta}_{\rm m}(\boldsymbol{k},\tau) - \theta(\boldsymbol{k},\tau) = \int \frac{d^3k_1}{(2\pi)^3} \int \frac{d^3k_2}{(2\pi)^3} (2\pi)^3 \delta_D^{(3)}(\boldsymbol{k}_1 + \boldsymbol{k}_2 - \boldsymbol{k}) \frac{\boldsymbol{k}\cdot\boldsymbol{k}_1}{k_1^2} \theta(\boldsymbol{k}_1,\tau)\delta_{\rm m}(\boldsymbol{k}_2,\tau), \quad (88)$$

$$\dot{\theta}(\boldsymbol{k},\tau) + \left(\frac{3}{2}\frac{\Omega_m}{f^2} - 1\right)\theta(\boldsymbol{k},\tau) - \frac{3}{2}\frac{\Omega_m}{f^2}\delta_{\rm m}(\boldsymbol{k},\tau)$$
$$= \int \frac{d^3k_1}{(2\pi)^3} \int \frac{d^3k_2}{(2\pi)^3} \delta_D^{(3)}(\boldsymbol{k}_1 + \boldsymbol{k}_2 - \boldsymbol{k}) \frac{k^2(\boldsymbol{k}_1\cdot\boldsymbol{k}_2)}{2k_1^2k_2^2} \theta(\boldsymbol{k}_1,\tau)\theta(\boldsymbol{k}_2,\tau). \quad (89)$$

The right-hand side of these equations represent non-linear coupling originated from advection terms of the fluid equations, which are neglected in previous section 2.2.2. These equations can be solved order by order, and the solutions are formally expressed as:

$$\delta_{\rm m} = \sum_{n=1} \delta_n(\boldsymbol{k},\tau), \quad \theta = \sum_{n=1} \theta_n(\boldsymbol{k},\tau); \quad (90)$$

$$\delta_n(\boldsymbol{k},\tau) = \int \frac{d^3p_1}{(2\pi)^3} \cdots \frac{d^3p_n}{(2\pi)^3} (2\pi)^3 \delta_{\rm D}^{(3)}(\boldsymbol{p}_{1\cdots n} - \boldsymbol{k}) F_n(\boldsymbol{p}_1,\cdots,\boldsymbol{p}_n,\tau)\delta_{\rm L}(\boldsymbol{p}_1,\tau)\cdots\delta_{\rm L}(\boldsymbol{p}_n,\tau), \quad (91)$$

$$\theta_n(\boldsymbol{k},\tau) = \int \frac{d^3p_1}{(2\pi)^3} \cdots \frac{d^3p_n}{(2\pi)^3} (2\pi)^3 \delta_{\rm D}^{(3)}(\boldsymbol{p}_{1\cdots n} - \boldsymbol{k}) G_n(\boldsymbol{p}_1,\cdots,\boldsymbol{p}_n,\tau)\delta_{\rm L}(\boldsymbol{p}_1,\tau)\cdots\delta_{\rm L}(\boldsymbol{p}_n,\tau). \quad (92)$$

Here, F_n and G_n are called standard PT kernels, δ_n and θ_n are the quantities at n-th order, and $\delta_1 = \theta_1 = \delta_{\rm L}$ from Eq.(48). To derive the explicit expression for F_n and G_n, we substitute Eqs.(91) and (92) into Eqs.(88) and (89), and solve iteratively from lower order.

It is known that the time dependance of the term $\Omega_{\rm m}/f^2$ in Eqs.(88) and (89) is quite weak in realistic cosmological models. Here, we assume the Einstein-de Sitter universe ($\Omega_{\rm m} = f = 1$), and focus on the fastest growing mode. In this case, we obtain F_n and G_n analytically with time independent form (see for example [41]):

$$F_n(\boldsymbol{k}_1,\cdots,\boldsymbol{k}_n) = \sum_{m=1}^{n-1} \frac{G_{\rm m}(\boldsymbol{k}_1,\cdots,\boldsymbol{k}_{\rm m})}{(2n+3)(n-1)}$$
$$\times \left[(1+2n)\frac{\boldsymbol{q}\cdot\boldsymbol{q}_1}{q_1^2} F_{n-m}(\boldsymbol{k}_{m+1},\cdots,\boldsymbol{k}_n) + \frac{q^2(\boldsymbol{q}_1\cdot\boldsymbol{q}_2)}{q_1^2q_2^2} G_{n-m}(\boldsymbol{k}_{m+1},\cdots,\boldsymbol{k}_n)\right], \quad (93)$$

$$G_n(\boldsymbol{k}_1,\cdots,\boldsymbol{k}_n) = \sum_{m=1}^{n-1} \frac{G_{\rm m}(\boldsymbol{k}_1,\cdots,\boldsymbol{k}_{\rm m})}{(2n+3)(n-1)}$$
$$\times \left[3\frac{\boldsymbol{q}\cdot\boldsymbol{q}_1}{q_1^2} F_{n-m}(\boldsymbol{k}_{m+1},\cdots,\boldsymbol{k}_n) + n\frac{q^2(\boldsymbol{q}_1\cdot\boldsymbol{q}_2)}{q_1^2q_2^2} G_{n-m}(\boldsymbol{k}_{m+1},\cdots,\boldsymbol{k}_n)\right], \quad (94)$$

$$\boldsymbol{q}_1 \equiv \boldsymbol{k}_1 + \cdots + \boldsymbol{k}_{\rm m} \quad , \quad \boldsymbol{q}_2 \equiv \boldsymbol{k}_{m+1} + \cdots + \boldsymbol{k}_n \quad , \quad \boldsymbol{q} \equiv \boldsymbol{q}_1 + \boldsymbol{q}_2. \tag{95}$$

The expressions of the Kernels are not symmetrized about arguments, but below, we use symmetrized Kernels about their arguments for convenience. At $n < 3$, F_n and G_n are obtained by:

$$F_1(\boldsymbol{k}_1) = 1, \quad G_1(\boldsymbol{k}_1) = 1, \tag{96}$$

$$F_2(\boldsymbol{k}_1, \boldsymbol{k}_2) = \frac{10}{7} + \left(\frac{k_1}{k_2} + \frac{k_2}{k_1}\right)\frac{\boldsymbol{k}_1 \cdot \boldsymbol{k}_2}{k_1 k_2} + \frac{4}{7}\left(\frac{\boldsymbol{k}_1 \cdot \boldsymbol{k}_2}{k_1 k_2}\right)^2, \tag{97}$$

$$G_2(\boldsymbol{k}_1, \boldsymbol{k}_2) = \frac{6}{7} + \left(\frac{k_1}{k_2} + \frac{k_2}{k_1}\right)\frac{\boldsymbol{k}_1 \cdot \boldsymbol{k}_2}{k_1 k_2} + \frac{8}{7}\left(\frac{\boldsymbol{k}_1 \cdot \boldsymbol{k}_2}{k_1 k_2}\right)^2. \tag{98}$$

In general, the $\Omega_{\rm m}/f^2$ term is time dependent. For example, it is known from numerical calculation that in GR case [42],

$$f \simeq \Omega_m^{0.55}. \tag{99}$$

Therefore, the Kernels must have time dependance. However, the time dependance of the Kernels is very weak in usual case, and we can generally approximate the PT solutions even in the non-Einstein-de Sitter universe as follows [43, 44, 45]:

$$\delta_{\rm m}(\boldsymbol{k}, \tau) = \sum_{n=1} \int \frac{d^3\boldsymbol{p}_1 \cdots d^3\boldsymbol{p}_n}{(2\pi)^{3n}} \delta_{\rm D}(\boldsymbol{k} - \boldsymbol{p}_{1\cdots n})\, F_n(\boldsymbol{p}_1, \cdots, \boldsymbol{p}_n)\delta_{\rm L}(\boldsymbol{p}_1, \tau) \cdots \delta_{\rm L}(\boldsymbol{p}_n, \tau), \tag{100}$$

$$\theta(\boldsymbol{k}, \tau) = \sum_{n=1} \int \frac{d^3\boldsymbol{p}_1 \cdots d^3\boldsymbol{p}_n}{(2\pi)^{3n}} \delta_{\rm D}(\boldsymbol{k} - \boldsymbol{p}_{1\cdots n})\, G_n(\boldsymbol{p}_1, \cdots, \boldsymbol{p}_n)\delta_{\rm L}(\boldsymbol{p}_1, \tau) \cdots \delta_{\rm L}(\boldsymbol{p}_n, \tau). \tag{101}$$

3.2.2 SPT in redshift space

The SPT treatment discussed above can be also applied to the nonlinear density field in redshift space, let us first expand the redshift-space density field in Fourier space. The Taylor expansion of Eq. (66) leads to:

$$\begin{aligned}\delta_{\rm i}^{(\rm s)}(\boldsymbol{k}) = \sum_{n=0} \int \frac{d^3\boldsymbol{q}_1}{(2\pi)^3} \cdots \int \frac{d^3\boldsymbol{q}_n}{(2\pi)^3} \delta_{\rm D}(\boldsymbol{k} - \boldsymbol{q}_{1\cdots n}) \\ \times \{\delta_{\rm i}(\boldsymbol{k}) + f\mu^2\theta(\boldsymbol{k})\}\, \frac{(f\mu k)^n}{n!} \frac{\mu_1}{q_1}\theta(\boldsymbol{q}_1) \cdots \frac{\mu_n}{q_n}\theta(\boldsymbol{q}_n),\end{aligned} \tag{102}$$

where $\boldsymbol{q}_{1\cdots n}$ being $\boldsymbol{q}_1 + \cdots + \boldsymbol{q}_n$, and i means m or h. Then, the real-space quantities δ_i and θ are further expanded in terms of the standard PT kernels by substituting Eqs.(100)

and (101). Plugging the above expressions into Eq. (102), reorganizing the perturbative expansion in powers of $\delta_{\rm L}$ leads to

$$\delta_{\rm i}^{(\rm s)}(\boldsymbol{k}) = \sum_{n=1} \int \frac{d^3\boldsymbol{q}_1}{(2\pi)^3} \cdots \int \frac{d^3\boldsymbol{q}_n}{(2\pi)^3} \delta_D(\boldsymbol{k} - \boldsymbol{q}_{1\cdots n}) Z_n(\boldsymbol{q}_1, \cdots, \boldsymbol{q}_n) \delta_{\rm L}(\boldsymbol{q}_1) \cdots \delta_{\rm L}(\boldsymbol{q}_n). \tag{103}$$

Here, the Z_n is called redshift-space PT kernel, and these are expressed in terms of the real-space PT kernels in a rather intricate way. We present the explicit expression for Z_n up to fourth order (e.g., [46]) bellow.

$$Z_1(\boldsymbol{k}) = b(k) + f\mu^2, \tag{104}$$

$$Z_2(\boldsymbol{k}_1, \boldsymbol{k}_2) = b(k) F_2(\boldsymbol{k}_1, \boldsymbol{k}_2) + f\mu^2 G_2(\boldsymbol{k}_1, \boldsymbol{k}_2) + \frac{f\mu k}{2} \left[\frac{\mu_1}{k_1} (b(k) + f\mu_2^2) + \frac{\mu_2}{k_2} (b(k) + f\mu_1^2) \right]. \tag{105}$$

$$\begin{aligned} Z_3(\boldsymbol{k}_1, \boldsymbol{k}_2, \boldsymbol{k}_3) = {} & b(k) F_3(\boldsymbol{k}_1, \boldsymbol{k}_2, \boldsymbol{k}_3) + f\mu^2 G_3(\boldsymbol{k}_1, \boldsymbol{k}_2, \boldsymbol{k}_3) + f\mu k \left[b(k) F_2(\boldsymbol{k}_2, \boldsymbol{k}_3) + f\mu_{23}^2 G_2(\boldsymbol{k}_2, \boldsymbol{k}_3) \right] \frac{\mu_1}{k_1} \\ & + f\mu k (b(k) + f\mu_1^2) \frac{\mu_{23}}{k_{23}} G_2(\boldsymbol{k}_2, \boldsymbol{k}_3) + \frac{(f\mu k)^2}{2} (b(k) + f\mu_1^2) \frac{\mu_2}{k_2} \frac{\mu_3}{k_3}, \end{aligned} \tag{106}$$

$$Z_4(\boldsymbol{k}_1, \boldsymbol{k}_2, \boldsymbol{k}_3, \boldsymbol{k}_4) = Z_{4\rm a}(\boldsymbol{k}_1, \boldsymbol{k}_2, \boldsymbol{k}_3, \boldsymbol{k}_4) + Z_{4\rm b}(\boldsymbol{k}_1, \boldsymbol{k}_2, \boldsymbol{k}_3, \boldsymbol{k}_4). \tag{107}$$

Here, the fourth-order kernels $Z_{4\rm a}$ and $Z_{4\rm b}$ are respectively given by

$$\begin{aligned} Z_{4\rm a}(\boldsymbol{k}_1, \boldsymbol{k}_2, \boldsymbol{k}_3, \boldsymbol{k}_4) = {} & b(k) F_4(\boldsymbol{k}_1, \boldsymbol{k}_2, \boldsymbol{k}_3, \boldsymbol{k}_4) + f\mu^2 G_4(\boldsymbol{k}_1, \boldsymbol{k}_2, \boldsymbol{k}_3, \boldsymbol{k}_4) \\ & + f\mu k \left[b(k) F_3(\boldsymbol{k}_2, \boldsymbol{k}_3, \boldsymbol{k}_4) + f\mu_{234}^2 G_3(\boldsymbol{k}_2, \boldsymbol{k}_3, \boldsymbol{k}_4) \right] \frac{\mu_1}{k_1} \\ & + f\mu k (b(k) + f\mu_1^2) \frac{\mu_{234}}{k_{234}} G_3(\boldsymbol{k}_2, \boldsymbol{k}_3, \boldsymbol{k}_4) + \frac{(f\mu k)^3}{6} (b(k) + f\mu_1^2) \frac{\mu_2}{k_2} \frac{\mu_3}{k_3} \frac{\mu_4}{k_4}, \end{aligned} \tag{108}$$

$$\begin{aligned} Z_{4\rm b}(\boldsymbol{k}_1, \boldsymbol{k}_2, \boldsymbol{k}_3, \boldsymbol{k}_4) = {} & f\mu k \left[b(k) F_2(\boldsymbol{k}_1, \boldsymbol{k}_2) + f\mu_{12}^2 G_2(\boldsymbol{k}_1, \boldsymbol{k}_2) \right] \frac{\mu_{34}}{k_{34}} G_2(\boldsymbol{k}_3, \boldsymbol{k}_4) \\ & + \frac{(f\mu k)^2}{2} \left[b(k) F_2(\boldsymbol{k}_1, \boldsymbol{k}_2) + f\mu_{12}^2 G_2(\boldsymbol{k}_1, \boldsymbol{k}_2) \right] \frac{\mu_3}{k_3} \frac{\mu_4}{k_4} \\ & + \frac{(f\mu k)^2}{2} \frac{\mu_{12}}{k_{12}} G_2(\boldsymbol{k}_1, \boldsymbol{k}_2) \left[(b(k) + f\mu_3^2) \frac{\mu_4}{k_4} + (b(k) + f\mu_4^2) \frac{\mu_3}{k_3} \right]. \end{aligned} \tag{109}$$

In the above, the vector $\boldsymbol{k}$ in the n-th order kernel implies $\boldsymbol{k} = \boldsymbol{k}_1 + \cdots + \boldsymbol{k}_n$, and $b(k)$ is the bias function which parametrize the relation between the matter density field and galaxy/halo number density field, described the retail at Chap. 5.6.1. The quantities μ, μ_i, μ_{ij}, and μ_{ijk} are defined by:

$$\mu \equiv \frac{\boldsymbol{k} \cdot \hat{\boldsymbol{z}}}{k}, \quad \mu_i \equiv \frac{\boldsymbol{k}_i \cdot \hat{\boldsymbol{z}}}{k_i}, \quad \mu_{ij} \equiv \frac{(\boldsymbol{k}_i + \boldsymbol{k}_j) \cdot \hat{\boldsymbol{z}}}{|\boldsymbol{k}_i + \boldsymbol{k}_j|}, \quad \mu_{ijk} \equiv \frac{(\boldsymbol{k}_i + \boldsymbol{k}_j + \boldsymbol{k}_k) \cdot \hat{\boldsymbol{z}}}{|\boldsymbol{k}_i + \boldsymbol{k}_j + \boldsymbol{k}_k|}. \tag{110}$$

In applying these results to the statistical calculations described in Chap. 3.3 and 4.3, the kernels Z_n have to be symmetrized under the exchange of each argument. One important remark is that even with fully symmetrized kernels F_n and G_n, the resultant redshift-space kernels Z_n at $n \geq 3$ only preserve partial symmetry. For instance, while the kernel Z_3 given at Eq. (106) is symmetric under $\boldsymbol{k}_1 \leftrightarrow \boldsymbol{k}_3$, the expression for Z_{4a} preserve the symmetry of $\boldsymbol{k}_2 \leftrightarrow \boldsymbol{k}_3 \leftrightarrow \boldsymbol{k}_4$. These kernels become fully symmetrized if we take the cyclic permutations.

3.3 The perturbative calculation of power spectrum and bispectrum up to 1-loop level

With the PT expression of the density field in Eq. (103), the redshift-space power spectrum and bispectrum are expanded as

$$P^{(\mathrm{s})}(\boldsymbol{k}) = P^{\mathrm{lin}} + P^{1\text{-loop}} + \cdots, \tag{111}$$

$$B^{(\mathrm{s})}(\boldsymbol{k}_1, \boldsymbol{k}_2, \boldsymbol{k}_3) = B^{\mathrm{tree}} + B^{1\text{-loop}}_{222} + B^{1\text{-loop}}_{321\text{-I}} + B^{1\text{-loop}}_{321\text{-II}} + B^{1\text{-loop}}_{411} + \cdots. \tag{112}$$

The power spectrum and bispectrum in real space are also expanded by same expression. As we will mention below, one can easily obtain expressions of real space from that of redshift space, so we focus on the expressions if redshift space in this section. Each term at the right-hand-side of Eqs.(111) and (112) are given by

$$P^{\mathrm{lin}}(\boldsymbol{k}) = \{Z_1(\boldsymbol{k})\}^2 P_{\mathrm{L}}(k), \tag{113}$$

$$P^{1\text{-loop}}(\boldsymbol{k}) = \int \frac{d^3p}{(2\pi)^3} \{Z_2(\boldsymbol{p}, \boldsymbol{k}-\boldsymbol{p})\}^2 P_{\mathrm{L}}(p) P_{\mathrm{L}}(|\boldsymbol{k}-\boldsymbol{p}|) + 2Z_1(\boldsymbol{k}) P_{\mathrm{L}}(k) \int \frac{d^3p}{(2\pi)^3} \{Z_3(\boldsymbol{p}, -\boldsymbol{p}, \boldsymbol{k})\} P_{\mathrm{L}}(p). \tag{114}$$

for the power spectrum, and

$$B^{\mathrm{tree}}(\boldsymbol{k}_1, \boldsymbol{k}_2, \boldsymbol{k}_3) = 2Z_2(\boldsymbol{k}_1, \boldsymbol{k}_2) Z_1(\boldsymbol{k}_1) Z_1(\boldsymbol{k}_2) P_{\mathrm{L}}(k_1) P_{\mathrm{L}}(k_2) + 2 \text{ perms } (\boldsymbol{k}_1 \leftrightarrow \boldsymbol{k}_2 \leftrightarrow \boldsymbol{k}_3), \tag{115}$$

$$B^{1\text{-loop}}_{222}(\boldsymbol{k}_1, \boldsymbol{k}_2, \boldsymbol{k}_3) = \int \frac{d^3p}{(2\pi)^3} Z_2(\boldsymbol{p}, \boldsymbol{k}_1 - \boldsymbol{p}) Z_2(-\boldsymbol{p}, \boldsymbol{k}_2 + \boldsymbol{p}) Z_2(-\boldsymbol{k}_1 + \boldsymbol{p}, -\boldsymbol{k}_2 - \boldsymbol{p}) \times P_{\mathrm{L}}(p) P_{\mathrm{L}}(|\boldsymbol{k}_1 - \boldsymbol{p}|) P_{\mathrm{L}}(|\boldsymbol{k}_2 + \boldsymbol{p}|) + 2 \text{ perms } (\boldsymbol{k}_1 \leftrightarrow \boldsymbol{k}_2 \leftrightarrow \boldsymbol{k}_3), \tag{116}$$

$$B^{\text{1-loop}}_{\text{321-I}}(\boldsymbol{k}_1,\boldsymbol{k}_2,\boldsymbol{k}_3) = Z_1(\boldsymbol{k}_1)P_{\text{L}}(k_1)\int\frac{d^3p}{(2\pi)^3}Z_2(\boldsymbol{p},\boldsymbol{k}_2-\boldsymbol{p})Z_3(-\boldsymbol{k}_1,-\boldsymbol{p},-\boldsymbol{k}_2+\boldsymbol{p})P_{\text{L}}(p)P_{\text{L}}(|\boldsymbol{k}_2-\boldsymbol{p}|) + 5\text{ perms }(\boldsymbol{k}_1\leftrightarrow\boldsymbol{k}_2\leftrightarrow\boldsymbol{k}_3), \tag{117}$$

$$B^{\text{1-loop}}_{\text{321-II}}(\boldsymbol{k}_1,\boldsymbol{k}_2,\boldsymbol{k}_3) = Z_1(\boldsymbol{k}_1)Z_2(\boldsymbol{k}_1,\boldsymbol{k}_2)P_{\text{L}}(k_1)P_{\text{L}}(k_2)\int\frac{d^3p}{(2\pi)^3}Z_3(\boldsymbol{k}_2,\boldsymbol{p},-\boldsymbol{p})P_{\text{L}}(p) + 5\text{ perms }(\boldsymbol{k}_1\leftrightarrow\boldsymbol{k}_2\leftrightarrow\boldsymbol{k}_3), \tag{118}$$

$$B^{\text{1-loop}}_{411}(\boldsymbol{k}_1,\boldsymbol{k}_2,\boldsymbol{k}_3) = Z_1(\boldsymbol{k}_1)Z_1(\boldsymbol{k}_2)P_{\text{L}}(k_1)P_{\text{L}}(k_2)\int\frac{d^3p}{(2\pi)^3}Z_4(-\boldsymbol{k}_1,-\boldsymbol{k}_2,\boldsymbol{p},-\boldsymbol{p})P_{\text{L}}(p) + 2\text{ perms }(\boldsymbol{k}_1\leftrightarrow\boldsymbol{k}_2\leftrightarrow\boldsymbol{k}_3). \tag{119}$$

for the bispectrum. In deriving the expressions above, we assume the Gaussianity of linear density field δ_{L}. One can easily obtain the expressions for the real-space power spectrum and bispectrum of density field if we replace the kernels Z_n with F_n. A notable point in redshift space is that the redshift-space kernel depends on the line-of-sight direction. As a result, the statistical isotropy of power spectrum and bispectrum is broken in each term, and we need one and two more additional variables to characterize the redshift-space power spectrum and bispectrum, respectively.

Another important point is that the kernels Z_n at $n \geq 2$ include the mode-coupling contributions from the velocity fields, which basically come from the perturbative expansion of the exponential factor in Eq. (66). This implies that the Finger-of-God damping effect cannot be simply described in a naive standard PT treatment, and we need to resum the infinite series of PT expansions. As it has been shown in Ref. [11], the standard PT prediction in redshift space largely overestimates the power spectrum amplitude at one-loop order, and cannot accurately describe the BAO in redshift space. The applicable range of one-loop prediction thus becomes narrower than that of the real-space prediction. Since the expression of bispectrum also uses the redshift PT kernels and it even includes the higher-order, the situation must be similar or rather worse than that in the power spectrum case. We will see in Chap. 4.4 that without accounting the Finger-of-God damping, standard PT prediction of bispectrum starts to deviate from simulation even at large scales. A proper account of the damping effect is essential, and we will consider how to incorporates the damping effect into the PT calculation in Chap. 4.3.

3.4 Comparison between N-body simulation and SPT

Here, we compare the N-body simulation results using 2LPT and Gadget2 with SPT one-loop results in real space to make sure the consistency of both method. The setting of N-body simulation is described as Chap. 5.3. The results are shown at Figs. 3 and 4.

In the case of power spectrum, SPT one-loop model is correspond with the result of N-body simulation by few % accuracy at large scale, while the linear power spectrum soon deviate from the simulation more than 5%.

Although the consistency is worse than the case of power spectrum, bispectrum from SPT one-loop calculation still agree with N-body result almost 5% at high redshift $z = 1$.

As we will see at Chap. 4.4.3, the SPT bispectrum in redshift space are soon deviate from N-body simulation. Therefore, we need to consider improved method to include non-linearity of RSD.

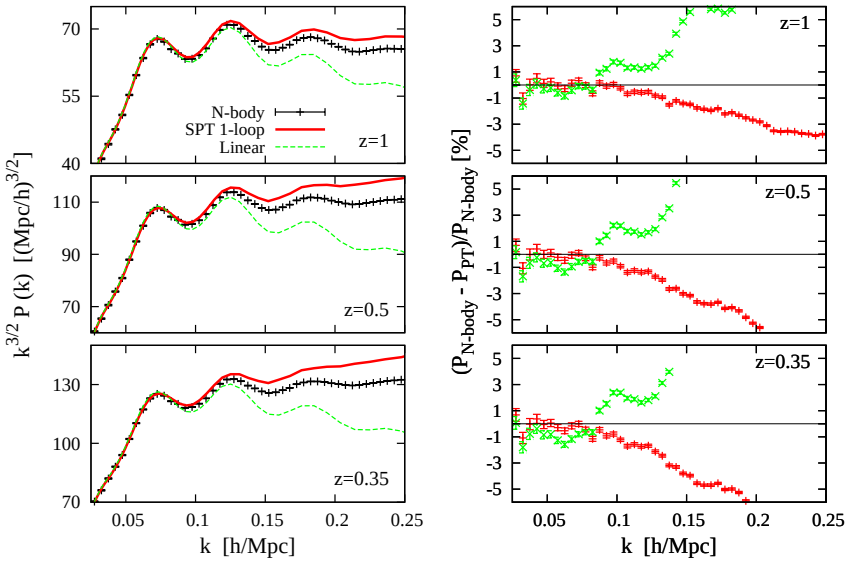

Figure 3: Real-space power spectrum as function of wave number k at $z = 3$ (top), 1 (middle) and 0.35 (bottom). The left panels plot the power spectrum multiplied by $k^{3/2}$, while the right panels show the fractional difference between the N-body simulation by Gadget-2 [40, 39] and PT predictions, $(P_{N-\mathrm{body}} - P_{\mathrm{PT}})/P_{N-\mathrm{body}}$. In each panel, black points with error bars indicate the results of N-body simulations. The green dashed and red solid lines are the linear theory and the standard PT one-loop predictions.

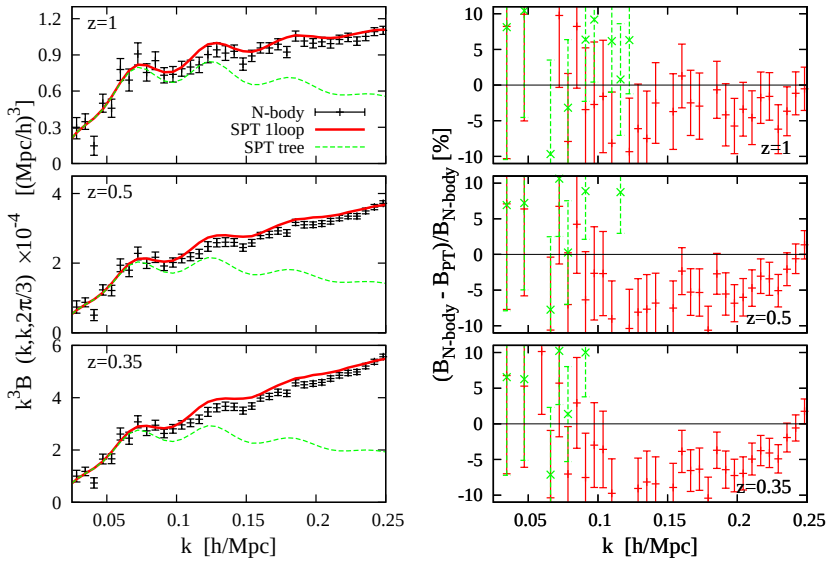

Figure 4: Real-space bispectrum as function of wave number k at $z = 3$ (top), 1 (middle) and 0.35 (bottom). The left panels plot the bispectrum multiplied by k^3, while the right panels show the fractional difference between the N-body simulation by Gadget-2 [40, 39] and PT predictions, $(B_{N-\mathrm{body}} - B_{\mathrm{PT}})/B_{N-\mathrm{body}}$. The expressions of the points and lines are similar to Fig. 3.

Chapter 4 Precision modeling of redshift-space bispectrum

In this chapter, we begin by reviewing the current cosmological constraints through power spectrum and bispectrum of LSS, focusing on the test of gravity with redshift-space distortions. We discuss the prospect for testing gravity through future galaxy redshift surveys, and address a crucial aspect toward a precision test of gravity. Then, we present an improved theoretical model for redshift-space bispectrum, which we aim at applying to a precision test of gravity. Comparing with N-body simulation, the validity of the improved model is also discussed. This chapter is based on Ref. [47].

4.1 Motivation

The measurements of RSD taken from various observations now cover a wide range of redshifts out to $z \sim 1.4$ (e.g., Refs. [48, 49, 50, 51, 52], see also Chap. 5.5 of Ref. [53]), and the results are broadly consistent with general relativity as shown in Fig. 5. But a closer look at the constrained values of $f\sigma_8$ suggests a mild tension with the Planck ΛCDM model [54], indicating some systematics or potentially new physics. Here, σ_8 is the normalization amplitude of the linear power spectrum smoothed over $8\,h^{-1}$ Mpc. A further improvement on the RSD measurement is thus important, mitigating both the statistical errors and systematics. This is one of the main reasons why there are various projects aiming at precisely measuring RSD which will uncover a large cosmic volume.

With a gigantic survey volume, the next-generation galaxy redshift surveys (e.g. Euclid, LSST) will therefore offer an opportunity to precisely measure the power spectrum or correlation function at an unprecedented precision, and provided a high-precision template, a robust and tight constraint on $f\sigma_8$ will be expected. Furthermore, one promising point is that taking advantage of a large-volume data, a high-statistical measurement of the higher-order statistics such as bispectrum or three-point correlation function is made available, and combining it with power spectrum measurement further helps to tighten the constraint on $f\sigma_8$.

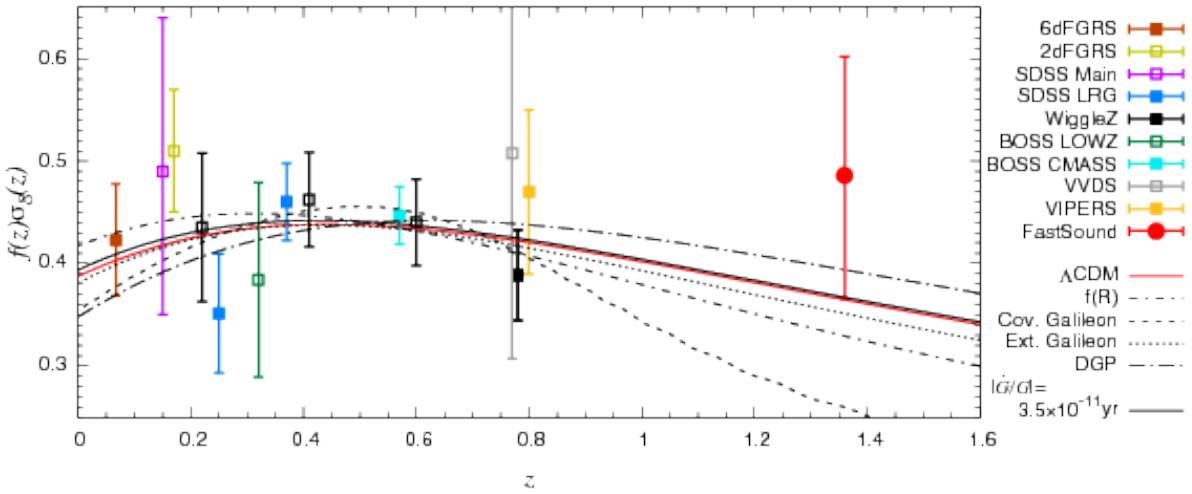

Figure 5: Current status of constraint on $f\sigma_8$ as a function of redshift through power spectrum and two point correlation function of LSS with various galaxy surveys. The each line shows the amplitude of $f\sigma_8$ from different theories of gravity obtained by minimizing χ^2. The data points used for the χ^2 minimization are denoted as the filled-symbol points while those which are not used are denoted as the open-symbol points. This figure is taken from Ref. [49].

There have been various studies based on the Fisher matrix analysis to quantify the statistical impact of the bispectrum on the cosmological parameter estimation, showing that adding the bispectrum indeed plays an important role to break parameter degeneracy (e.g., Refs. [55, 56, 57, 58, 59]). In particular, the impact of combining bispectrum measurement is demonstrated for the RSD measurement by Refs. [60, 61], showing that even if we restrict the data to the large-scale modes, the constraint on $f\sigma_8$ will be improved by a factor of two as shown in Fig. 6 [60].

However, most of these analysis has been demonstrated in a very simplified setup, assuming that the observed bispectrum is described by the perturbation theory (PT) at leading order [46], on top of a simple prescription for galaxy bias. While such a simplified forecast study helps to understand the ability and/or potential of the planned galaxy surveys, there are a number of remarks and cautions in a practical data analysis. One important point to be noted is the theoretical template of redshift-space bispectrum. While the perturbative description is supposed to be adequate in real space at the weakly nonlinear stage of gravitational clustering, the situation becomes more subtle in redshift space, because the redshift space is related to the real space through nonlinear mapping. As a

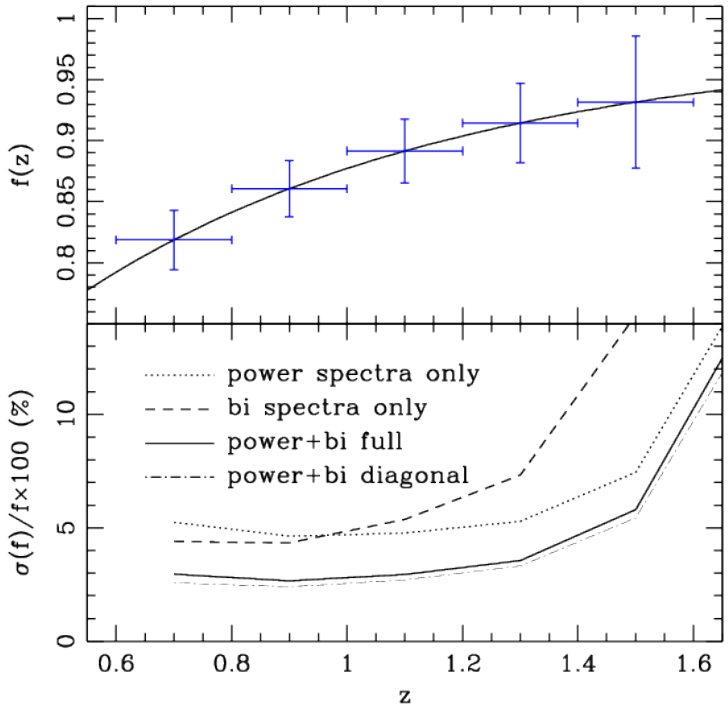

Figure 6: Upper: Expected 1σ (68% C.L.) constraint on the linear growth rate $f(z)$, assuming the future spectroscopy survey DESI (Dark Energy Spectroscopy Instrument). The results are estimated using both the power spectrum and bispectrum. Lower: The fractional errors of f from power spectrum (dotted), bispectrum (dashed) and the combined result of the power spectrum and bispectrum. In the combined case, taking account of the cross covariance, is plotted as solid curve, and taking account of the diagonals only, is plotted as dot-dashed curve. This figure is taken from Ref. [60].

result, in terms of the real-space quantities, even the redshift-space power spectrum cannot be simply expressed as the large-scale two-point statistics of the underlying fields, and is significantly affected by the small-scale physics (e.g., Ref. [6]). Hence, a sophisticated treatment is needed for a reliable theoretical template even in the weakly nonlinear regime [11, 20, 21, 22, 23, 24, 25, 26].

On the other hand, the analysis using the redshift-space bispectrum has been already examined in the existing galaxy surveys [62, 63], and the constraints on $f\sigma_8$ is shown to be improved by combining the power spectrum with bispectrum, as shown in Fig. 7 [62]. The improvement of the constraint is, however, rather milder than expected. One possible reason is that they only use the monopole moment of bispectrum, ignoring the quadrupole and higher-multipole bispectra. Since the higher-multipole bispectra naturally appear due to the RSD, a measurement of higher-multipoles would be essential to get a tighter constraint [61, 64], and modeling the anisotropic components of redshift-space bispectrum is thus rather critical.

The aim of this chapter is to address this issue, and based on the next-to-leading order calculations, we present a perturbation-theory model of redshift-space bispectrum, which consistently incorporates the effect coming from the small-scale virial motion. While modeling the redshift-space bispectrum has been already investigated based on fitting formula [27, 28] and halo model (e.g., Refs. [29, 30]), analytical treatment would be certainly powerful in characterizing the anisotropies of the redshift-space bispectrum (see e.g., [31] for discussion on resummed PT treatment). In particular, with perturbation theory, one can give an accurate description for the large scales of our interest. Albeit its limitation, the PT-based modeling therefore deserves further consideration, and we present, for the first time, monopole and quadrupole moments of the redshift-space bispectrum at one-loop order, which agree well with N-body simulations at BAO scales.

4.2 Exact formula of power spectrum and bispectrum in redshift space

In this section, prior to presenting our improved model of bispectrum, we discuss several remarks on modeling the redshift-space power spectrum and bispectrum based on the exact formulas. Using Eq. (66), the exact formulas for the power spectrum and bispectrum in redshift space, expressed in terms of the real-space quantities, are derived. Recalling that

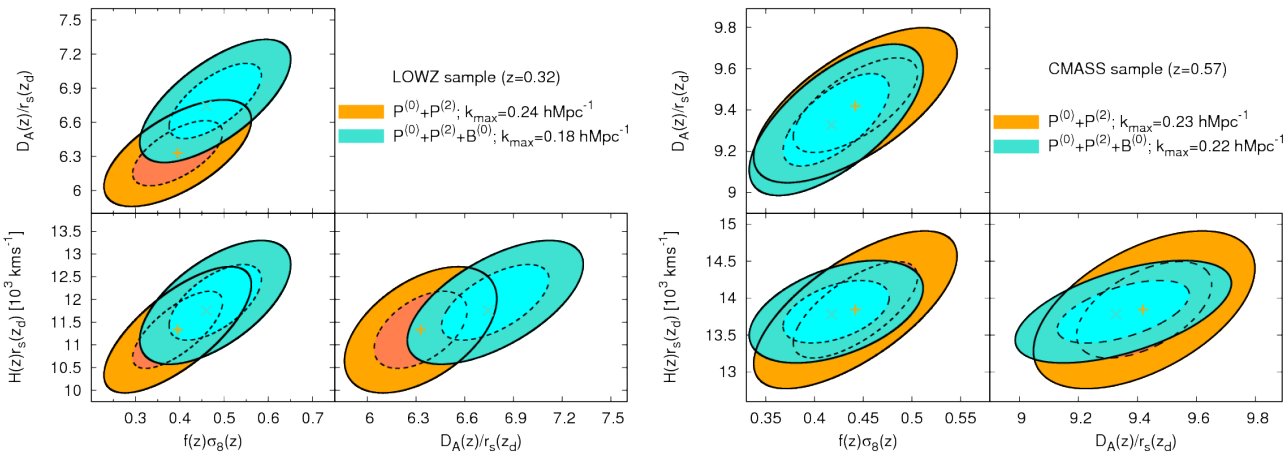

Figure 7: Comparison of the 1 σ (solid lines) and 2 σ (dashed lines) confident regions of $f\sigma_8$, $D_\mathrm{A}/r_\mathrm{s}$ and Hr_s, corresponding to the LOWZ and CMASS samples of BOSS. Here, D_A and r_s are the angular diameter distance and the sound horizon. The orange contours correspond to the constrains obtained by analyzing the power spectrum monopole and quadrupole up to $k_\mathrm{max} = 0.24h\mathrm{Mpc}^{-1}$ for LOWZ and $k_\mathrm{max} = 0.23h\mathrm{Mpc}^{-1}$ for CMASS, using the covariance matrix obtained from the MD-Patchy mocks [65]. The turquoise contours are the 1σ and 2σ confident levels obtained from the analysis of combining the power spectrum multipoles and the bispectrum up to $k_\mathrm{max} = 0.18h\mathrm{Mpc}^{-1}$ for the LOWZ sample and $k_\mathrm{max} = 0.22h\mathrm{Mpc}^{-1}$ for the CMASS sample. This figure is taken from Ref. [62].

the power spectrum and bispectrum are respectively defined as

$$(2\pi)^3\delta_{\rm D}(\boldsymbol{k}+\boldsymbol{k}')P^{(\rm s)}(\boldsymbol{k}) \equiv \langle\delta^{(\rm s)}(\boldsymbol{k})\delta^{(\rm s)}(\boldsymbol{k}')\rangle, \tag{120}$$

$$(2\pi)^3\delta_{\rm D}(\boldsymbol{k}_1+\boldsymbol{k}_2+\boldsymbol{k}_3)B^{(\rm s)}(\boldsymbol{k}_1,\boldsymbol{k}_2,\boldsymbol{k}_3) \equiv \langle\delta^{(\rm s)}(\boldsymbol{k}_1)\delta^{(\rm s)}(\boldsymbol{k}_2)\delta^{(\rm s)}(\boldsymbol{k}_3)\rangle, \tag{121}$$

substituting Eq. (66) into the above leads to

$$P^{(\rm s)}(\boldsymbol{k}) = \int d\boldsymbol{r}e^{i\boldsymbol{k}\cdot\boldsymbol{r}_{12}}\Big\langle e^{-ifk_zu_{12z}}\left\{\delta(\boldsymbol{r}_1)+f\nabla_z u_z(\boldsymbol{r}_1)\right\}\left\{\delta(\boldsymbol{r}_2)+f\nabla_z u_z(\boldsymbol{r}_2)\right\}\Big\rangle, \tag{122}$$

for the redshift-space power spectrum, and

$$B^{(\rm s)}(\boldsymbol{k}_1,\boldsymbol{k}_2,\boldsymbol{k}_3) = \int d\boldsymbol{r}_{13}\boldsymbol{r}_{23}e^{i(\boldsymbol{k}_1\cdot\boldsymbol{r}_{13}+\boldsymbol{k}_2\cdot\boldsymbol{r}_{23})}$$
$$\times\Big\langle e^{-if(k_{1z}u_{13z}+k_{2z}u_{23z})}\left\{\delta(\boldsymbol{r}_1)+f\nabla_z u_z(\boldsymbol{r}_1)\right\}\left\{\delta(\boldsymbol{r}_2)+f\nabla_z u_z(\boldsymbol{r}_2)\right\}\left\{\delta(\boldsymbol{r}_3)+f\nabla_z u_z(\boldsymbol{r}_3)\right\}\Big\rangle, \tag{123}$$

for the redshift-space bispectrum. Here, we used the normalized peculiar velocity defined at Eq.(87), and denote the pairwise normalized velocity of the separation $\boldsymbol{r}_{ij} = \boldsymbol{r}_i - \boldsymbol{r}_j$ by $\boldsymbol{u}_{ij} \equiv \boldsymbol{u}_i - \boldsymbol{u}_j$.

From the above expressions, we see that albeit the simple relation (60), the power spectrum and bispectrum in redshift space are rather intricate statistical relation. Qualitatively, the amplitude of the power spectrum is enhanced by the additional term of the velocity field at large scales (Kaiser effect [4]), while at small scales, it is also known that an exponential damping factor suppress the amplitude (Finger-of-God effect). We expect that the redshift-space bispectrum possesses similar qualitative features, because the structure of the expressions is of the same form in both the power spectrum and bispectrum. However, redshift-space bispectrum has additional complexity, that no longer characterized simply by the shape of the triangle, i.e., length of three wave vectors k_1, k_2 and k_3, or length of vectors k_1 and k_2 and their angle $\theta_{12} \equiv \cos^{-1}(\hat{\boldsymbol{k}}_1\cdot\hat{\boldsymbol{k}}_2)$. In addition to these three variables, we need two more variables to describe the orientation of the triangular shape with respect to the line-of-sight direction. In this respect, the identification and separation of the Kaiser and Finger-of-God effects are rather non-trivial, and we need more careful treatment for an accurate modeling of redshift-space bispectrum.

4.3 An improved modeling of redshift-space bispectrum

In this section, we present the PT model of redshift-space bispectrum which keeps the non-perturbative damping effect. Our strategy is to decompose the contributions into non-perturbative part and the terms which can be evaluated with PT calculation, starting with

the exact expression, Eq. (123). For this purpose, we follow the treatment by Ref. [11], and rewrite the exact expression in terms of cumulants. We then identify the non-perturbative part responsible for the FoG damping. Based on the simple proposition similarly made by Ref. [11], the non-perturbative damping term is separated out from the rest of the contributions, for which we apply the PT calculation. We derive the expression valid at one-loop order.

Let us begin by rewriting Eq. (123) in the form

$$B^{(\mathrm{s})}(\boldsymbol{k}_1, \boldsymbol{k}_2, \boldsymbol{k}_3) = \int d\boldsymbol{r}_{13} d\boldsymbol{r}_{23} e^{i(\boldsymbol{k}_1 \boldsymbol{r}_{13} + \boldsymbol{k}_2 \boldsymbol{r}_{23})} \langle A_1 A_2 A_3 e^{j_4 A_4 + j_5 A_5} \rangle, \tag{124}$$

where the quantities A_i, j_i are respectively defined by

$$A_1 = \delta(\boldsymbol{r}_1) + f \nabla_z u_z(\boldsymbol{r}_1), \tag{125}$$

$$A_2 = \delta(\boldsymbol{r}_2) + f \nabla_z u_z(\boldsymbol{r}_2), \tag{126}$$

$$A_3 = \delta(\boldsymbol{r}_3) + f \nabla_z u_z(\boldsymbol{r}_3), \tag{127}$$

$$A_4 = u_z(\boldsymbol{r}_1) - u_z(\boldsymbol{r}_3), \tag{128}$$

$$A_5 = u_z(\boldsymbol{r}_2) - u_z(\boldsymbol{r}_3), \tag{129}$$

$$j_4 = -ik_1 \mu_1 f, \tag{130}$$

$$j_5 = -ik_2 \mu_2 f, \tag{131}$$

with $\mu_i = \boldsymbol{k}_i \cdot \hat{\boldsymbol{z}}/k_i$. To express the moment given above in terms of the cumulants, we use the relation between moment and cumulant generating functions (e.g., [11, 6, 22]). For the stochastic vector field $\boldsymbol{A}$, we have

$$\langle e^{\boldsymbol{j} \cdot \boldsymbol{A}} \rangle = \exp\left\{ \langle e^{\boldsymbol{j} \cdot \boldsymbol{A}} \rangle_{\mathrm{c}} \right\}, \tag{132}$$

with j being an arbitrary constant vector, $\boldsymbol{j}$. To be specific, we assume that the vector fields given above are five components, i.e., $\boldsymbol{A} = \{A_1, A_2, A_3, A_4, A_5\}$ and $\boldsymbol{j} = \{j_1, j_2, j_3, j_4, j_5\}$. Then, taking the derivative three times with respect to j_1, j_2 and j_3, we set $j_1 = j_2 = j_3 = 0$. We obtain

$$\begin{aligned}
\langle A_1 A_2 A_3 e^{j_4 A_4 + j_5 A_5} \rangle = \exp\left\{ \langle e^{j_4 A_4 + j_5 A_5} \rangle_{\mathrm{c}} \right\} \Big[& \langle A_1 A_2 A_3 e^{j_4 A_4 + j_5 A_5} \rangle_{\mathrm{c}} + \langle A_1 A_2 e^{j_4 A_4 + j_5 A_5} \rangle_{\mathrm{c}} \langle A_3 e^{j_4 A_4 + j_5 A_5} \rangle_{\mathrm{c}} \\
& + \langle A_2 e^{j_4 A_4 + j_5 A_5} \rangle_{\mathrm{c}} \langle A_1 A_3 e^{j_4 A_4 + j_5 A_5} \rangle_{\mathrm{c}} + \langle A_1 e^{j_4 A_4 + j_5 A_5} \rangle_{\mathrm{c}} \langle A_2 A_3 e^{j_4 A_4 + j_5 A_5} \rangle_{\mathrm{c}} \\
& + \langle A_1 e^{j_4 A_4 + j_5 A_5} \rangle_{\mathrm{c}} \langle A_2 e^{j_4 A_4 + j_5 A_5} \rangle_{\mathrm{c}} \langle A_3 e^{j_4 A_4 + j_5 A_5} \rangle_{\mathrm{c}} \Big].
\end{aligned} \tag{133}$$

This equation is indeed what we want to derive, and the left hand side is exactly the same one as in the integrand of Eq. (124).

The above expression shows that the pairwise velocity fields A_4 and A_5 in the exponent produce non-trivial correlations with density and velocity gradient fields. Further, these fields appear in the overall prefactor. This is indeed the same structure as seen in the expression of power spectrum [11]. In power spectrum, the exponential prefactor is known to give a suppression of the amplitude due to the large-scale coherent and small-scale virialized motions, and at the large-scale of our interest, it mainly affects the broadband shape of the power spectrum. We expect that the overall prefactor in Eq. (133) similarly behaves like the one in the power spectrum, and it can alter the broadband shape of the bispectrum. Because of its functional form, the prefactor is likely to be affected by the small-scale nonlinearity even at large scales, and we may thus take it as non-perturbative part. On the other hand, the terms in the square bracket of Eq. (133) include the density fields and are responsible for reproducing the real-space bispectrum in the absence of redshift-space distortions [this is simply obtained by setting all the velocity fields in Eq. (133) to zero]. Thus, these terms basically carry the cosmological information, and imprints the acoustic feature of BAO. Although each term in the square bracket contains the exponential factor $e^{j_4A_4+j_5A_5}$, the contribution can be small as long as we consider the BAO scales, and the perturbative expansion may work well.

Based on these considerations, Ref. [11] presented a PT-based model for redshift-space power spectrum which we call TNS model. The TNS model reproduces the measured results of N-body simulations quite well, and incorporating the effect of galaxy bias into the model, it has been also applied to the galaxy survey data [13]. We describe the formulation of TNS model in Appendix C. Below, adopting the proposition by Ref. [11], we derive the PT model of redshift-space bispectrum valid at weakly nonlinear scales. That is,

(i) The overall prefactor, $\exp\left\{\langle e^{j_4A_4+j_5A_5}\rangle_{\rm c}\right\}$, is kept as a non-perturbative contribution, and is replaced with general functional form $D_{\rm FoG}$, which is assumed to be given as a function of $k_1\mu_1$, $k_2\mu_2$ and $k_3\mu_3$, ignoring the spatial correlation of A_4 and A_5. This means that the zero-lag correlation is the only dominant contribution. The relevant functional form of $D_{\rm FoG}$ will be discussed in Chap. 4.4.

(ii) The terms in the square bracket are treated perturbatively, and regarding the variables j_4 and j_5 as expansion parameters, we collect the contributions valid at one-loop

order in standard PT.

From the proposition (i), the overall exponential factor is factorized outside the integral over $\boldsymbol{r}_{13}$ and $\boldsymbol{r}_{23}$. We have

$$\begin{aligned} B^{(\mathrm{s})}(\boldsymbol{k}_1,\boldsymbol{k}_2,\boldsymbol{k}_3) \longrightarrow D_{\mathrm{FoG}}(k_1\mu_1,k_2\mu_2,k_3\mu_3) \int d\boldsymbol{r}_{13}d\boldsymbol{r}_{23} \\ \times e^{i(\boldsymbol{k}_1\boldsymbol{r}_{13}+\boldsymbol{k}_2\boldsymbol{r}_{23})}\Big[\langle A_1A_2A_3e^{j_4A_4+j_5A_5}\rangle_{\mathrm{c}} + \langle A_1A_2e^{j_4A_4+j_5A_5}\rangle_{\mathrm{c}}\langle A_3e^{j_4A_4+j_5A_5}\rangle_{\mathrm{c}} \\ + \langle A_2e^{j_4A_4+j_5A_5}\rangle_{\mathrm{c}}\langle A_1A_3e^{j_4A_4+j_5A_5}\rangle_{\mathrm{c}} + \langle A_1e^{j_4A_4+j_5A_5}\rangle_{\mathrm{c}}\langle A_2A_3e^{j_4A_4+j_5A_5}\rangle_{\mathrm{c}} \\ + \langle A_1e^{j_4A_4+j_5A_5}\rangle_{\mathrm{c}}\langle A_2e^{j_4A_4+j_5A_5}\rangle_{\mathrm{c}}\langle A_3e^{j_4A_4+j_5A_5}\rangle_{\mathrm{c}}\Big], \end{aligned} \tag{134}$$

We then expand the terms in the square bracket. Up to the third order in j_n, we obtain

$$B^{(\mathrm{s})}(\boldsymbol{k}_1,\boldsymbol{k}_2,\boldsymbol{k}_3) \longrightarrow D_{\mathrm{FoG}}(k_1\mu_1,k_2\mu_2,k_3\mu_3) \sum_{n=1}^{11} C_n(\boldsymbol{k}_1,\boldsymbol{k}_2,\boldsymbol{k}_3), \tag{135}$$

where the functions C_n are defined by

$$C_n(\boldsymbol{k}_1,\boldsymbol{k}_2,\boldsymbol{k}_3) \equiv \int d\boldsymbol{r}_{13}d\boldsymbol{r}_{23}\, e^{i(\boldsymbol{k}_1\boldsymbol{r}_{13}+\boldsymbol{k}_2\boldsymbol{r}_{23})}\, S_n \tag{136}$$

with the integrands S_n given below:

$$S_1 = \langle A_1A_2A_3\rangle_{\mathrm{c}}, \tag{137}$$

$$S_2 = \langle A_1A_2\rangle_{\mathrm{c}}\langle (j_4A_4+j_5A_5)A_3\rangle_{\mathrm{c}} + \mathrm{cyc}, \tag{138}$$

$$S_3 = \langle (j_4A_4+j_5A_5)A_1A_2A_3\rangle_{\mathrm{c}}, \tag{139}$$

$$S_4 = \langle (j_4A_4+j_5A_5)A_1A_2\rangle_{\mathrm{c}}\langle (j_4A_4+j_5A_5)A_3\rangle_{\mathrm{c}} + \mathrm{cyc}, \tag{140}$$

$$S_5 = \langle A_1A_2\rangle_{\mathrm{c}}\langle (j_4A_4+j_5A_5)^2A_3\rangle_{\mathrm{c}} + \mathrm{cyc}, \tag{141}$$

$$S_6 = \langle (j_4A_4+j_5A_5)A_1\rangle\langle (j_4A_4+j_5A_5)A_2\rangle\langle (j_4A_4+j_5A_5)A_3\rangle, \tag{142}$$

$$S_7 = \langle (j_4A_4+j_5A_5)^2A_1A_2A_3\rangle_{\mathrm{c}}, \tag{143}$$

$$S_8 = \langle (j_4A_4+j_5A_5)^3A_1A_2A_3\rangle_{\mathrm{c}}, \tag{144}$$

$$S_9 = \langle (j_4A_4+j_5A_5)^2A_1A_2\rangle_{\mathrm{c}}\langle (j_4A_4+j_5A_5)A_3\rangle_{\mathrm{c}} + \mathrm{cyc}, \tag{145}$$

$$S_{10} = \langle (j_4A_4+j_5A_5)A_1A_2\rangle_{\mathrm{c}}\langle (j_4A_4+j_5A_5)^2A_3\rangle_{\mathrm{c}} + \mathrm{cyc}, \tag{146}$$

$$S_{11} = \langle A_1A_2\rangle_{\mathrm{c}}\langle (j_4A_4+j_5A_5)^3A_3\rangle_{\mathrm{c}} + \mathrm{cyc}. \tag{147}$$

In the above, the relevant terms for one-loop PT calculations, which are of the order of $O(P_{\mathrm{L}}^3)$, appear at $n \leq 6$, and the rest of the terms turns out to be higher-order. Hence,

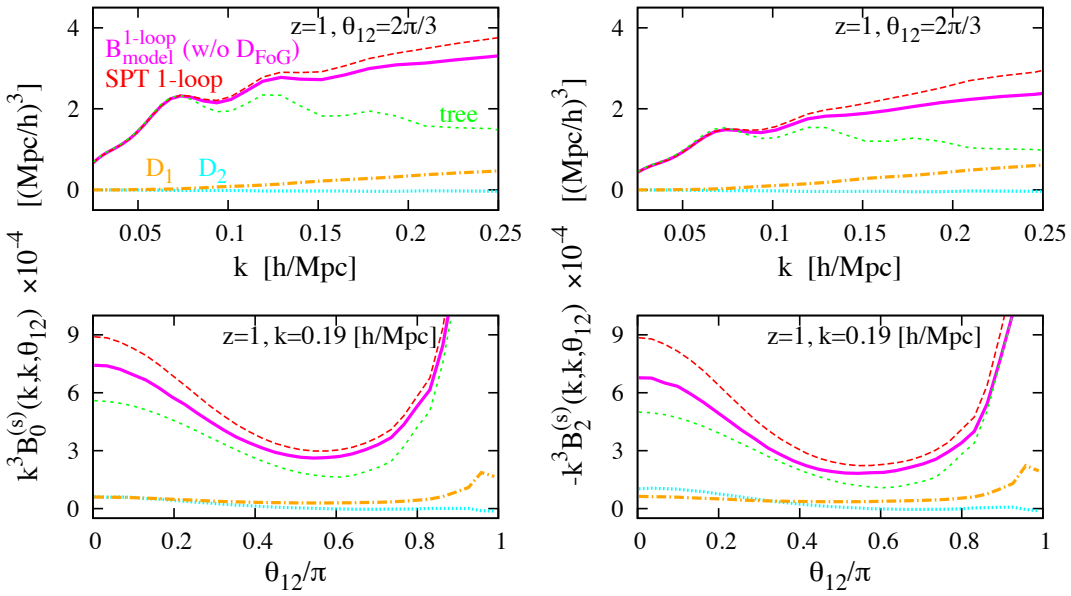

Figure 8: Monopole (left) and quadrupole (right) moments of redshift-space bispectrum from PT. The results at $z = 1$ are shown. While top panels show the scale-dependence of the equilateral configuration (i.e., plotted as function of $k \equiv k_1 = k_2 = k_3$ fixing θ_{12} to $2\pi/3$), bottom panels plot the shape dependence for isosceles configuration fixing the wave numbers to $k1 = k2 = k = 0.19h\,\mathrm{Mpc}^{-1}$. In each panel, green dotted and red dashed lines are respectively the standard PT predictions at tree-level ($B^{(\mathrm{s})}_{\mathrm{SPT,tree}}$) and one-loop order ($B^{(\mathrm{s})}_{\mathrm{SPT,1\text{-}loop}}$). Magenta solid lines are the prediction based on Eq. (151), $B^{(\mathrm{s})}_{\mathrm{model}}$, for which the term D_{FoG} is set to 1. This is essentially $B^{(\mathrm{s})}_{\mathrm{SPT,1\text{-}loop}}$, but the terms, D_1 (orange) and D_2 (cyan), are subtracted. This figure is taken from Ref. [47].

keeping the terms valid at the one-loop level, we model the redshift-space bispectrum as

$$B^{(\mathrm{s})}_{\mathrm{model}}(\boldsymbol{k}_1, \boldsymbol{k}_2, \boldsymbol{k}_3) = D_{\mathrm{FoG}}(k_1\mu_1, k_2\mu_2, k_3\mu_3) \sum_{n=1}^{6} C_n(\boldsymbol{k}_1, \boldsymbol{k}_2, \boldsymbol{k}_3). \tag{148}$$

The above model is compared with the standard PT results in Chap. 3.3, which can be also derived from Eqs. (124) and (133) by a naive expansion of all the exponential factors, $e^{i(j_4A_4+j_5A_5)}$. Collecting the relevant contributions at one-loop order, we have

$$B^{(\mathrm{s})}_{\mathrm{SPT,1\text{-}loop}}(\boldsymbol{k}_1, \boldsymbol{k}_2, \boldsymbol{k}_3) = \sum_{n=1}^{6} C_n(\boldsymbol{k}_1, \boldsymbol{k}_2, \boldsymbol{k}_3) + \sum_{n=1}^{2} D_n(\boldsymbol{k}_1, \boldsymbol{k}_2, \boldsymbol{k}_3). \tag{149}$$

with the functions D_n given by

$$D_n(\boldsymbol{k}_1, \boldsymbol{k}_2, \boldsymbol{k}_3) = \frac{1}{2} \int d\boldsymbol{r}_{13} d\boldsymbol{r}_{23}\, e^{i(\boldsymbol{k}_1\boldsymbol{r}_{13}+\boldsymbol{k}_2\boldsymbol{r}_{23})} S_n \langle (j_4A_4 + j_5A_5)^2 \rangle_{\mathrm{c}}, \tag{150}$$

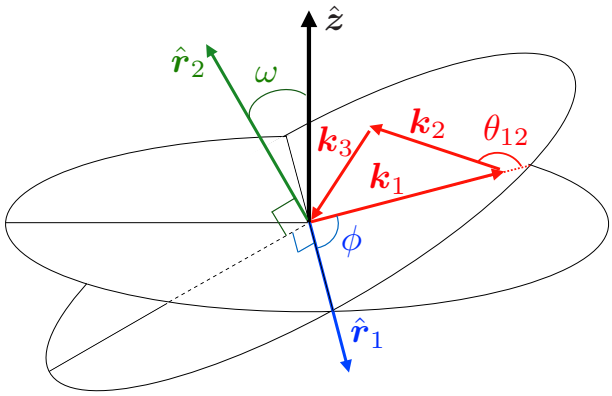

Figure 9: Definition of the angles, ω and ϕ, given in Eqs. (207) and (208), which characterize the orientation of the triangle against the line-of-sight direction, $\hat{\boldsymbol{z}}$. Here, the unit vectors, $\hat{\boldsymbol{r}}_1$ and $\hat{\boldsymbol{r}}_2$, are expressed in terms of the quantities indicated in the figure by $\hat{\boldsymbol{r}}_1 = \hat{\boldsymbol{z}} \times (\boldsymbol{k}_1 \times \boldsymbol{k}_2)/(k_1 k_2 \sin\theta_{12} \sin\omega)$ and $\hat{\boldsymbol{r}}_2 = \boldsymbol{k}_1 \times \boldsymbol{k}_2/(k_1 k_2 \sin\theta_{12})$. This figure is taken from Ref. [47]

where the function S_n $(n = 1, 2)$ is defined by Eqs. (137) and (138). These terms come from the expansion of the overall prefactor $\exp\left\{\langle e^{j_4 A_4 + j_5 A_5}\rangle_{\rm c}\right\}$. Hence, at one-loop order, Eq. (148) is recast as

$$B^{(\rm s)}_{\rm model}(\boldsymbol{k}_1, \boldsymbol{k}_2, \boldsymbol{k}_3) = D_{\rm FoG}(k_1\mu_1, k_2\mu_2, k_3\mu_3)\Big\{B^{(\rm s)}_{\rm SPT,1\text{-}loop}(\boldsymbol{k}_1, \boldsymbol{k}_2, \boldsymbol{k}_3) - \sum_{n=1}^{2} D_n(\boldsymbol{k}_1, \boldsymbol{k}_2, \boldsymbol{k}_3)\Big\}. \tag{151}$$

In what follows, we use Eq. (151) to compute the PT model of redshift-space bispectrum, and compare the predictions with N-body simulations. To be precise, we first compute $B^{(\rm s)}_{\rm SPT,1\text{-}loop}$ based on the standard PT calculations summarized in Chap. 3.3 [Eqs. (112) with (115), (116), (117), (118), and (119)]. Then, we subtract D_1 and D_2 terms from the standard PT bispectrum and, we take into account Fingers-of-God effect. The explicit expressions for D_1 and D_2 relevant for the one-loop calculations are presented in Appendix A.

Before closing this section, we look at the significance of the difference between the standard PT bispectrum and the model given in Eq. (151) or (148). In Fig. 8, ignoring the $D_{\rm FoG}$ contribution, the monopole and quadrupole moments of the bispectrum are computed at $z = 1$ for equilateral (top) and isosceles (bottom) configurations, and the results are plotted as function of k and angle $\theta_{12} \equiv \cos^{-1}(\hat{\boldsymbol{k}}_1 \cdot \hat{\boldsymbol{k}}_2)$, respectively. Here, the multipole

moments of the bispectrum, $B_\ell^{(\mathrm{s})}$, are defined by:

$$B_\ell^{(\mathrm{s})}(k_1, k_2, \theta_{12}) = \int_0^{2\pi} \frac{d\phi}{2\pi} \int_0^1 d\mu B^{(\mathrm{s})}(\boldsymbol{k}_1, \boldsymbol{k}_2, \boldsymbol{k}_3)\mathcal{P}_\ell(\mu), \tag{152}$$

where the function $\mathcal{P}_\ell(\mu)$ is the Legendre polynomials with μ being the directional cosine given by $\mu = \cos\omega$. The angles ω and ϕ characterize the orientation of the triangles (i.e., $\boldsymbol{k}_1$, $\boldsymbol{k}_2$, and $\boldsymbol{k}_3$) with respect to the line-of-sight direction (see Fig. 9). Precise definition of the angles ω and ϕ, together with the properties of multipole expansion, is described in Appendix B. Note that our definition differs from the one frequently used in the literature (e.g., Refs. [46, 66, 30, 61]), but a nice property is that the bispectrum multipoles become fully symmetric under the permutation of the order of k_1, k_2 and k_3.

Fig. 8 shows that both the one-loop bispectra, $B^{(\mathrm{s})}_{\mathrm{SPT,1\text{-}loop}}$ (red) and $B^{(\mathrm{s})}_{\mathrm{model}}$ (magenta), have a larger amplitude than the tree-level prediction. While these predictions lead to similar scale and shape dependencies, differences appear manifest at smaller scales due to the D_1 and D_2 terms. Though these two terms are basically small and weakly depend on scales, we will see below that subtracting these from $B^{(\mathrm{s})}_{\mathrm{SPT,1\text{-}loop}}$ indeed plays an important role to get a consistent damping behavior of D_{FoG} from both power spectrum and bispectrum (see Chap. 4.4.4).

4.4 Comparison with *N*-body simulations

In this section, we present a detailed comparison of the redshift-space bispectrum between PT predictions and *N*-body simulations. After briefly describing the *N*-body data set used in the analysis in Chap. 4.4.1, we first compare the real-space results in Sec 4.4.2 to see the applicable range of PT as well as the quality of *N*-body data. We then move to the redshift space, and compare the monopole and quadrupole bispectra from *N*-body simulations with those obtained by PT calculations in Chap. 4.4.3. Chap. 4.4.4 discusses the validity and consistency of the ansatz for the damping function D_{FoG} in our PT model of bispectrum.

4.4.1 *N*-body simulations and measurement of the bispectrum

We use the simulation ensembles Set B and Set C from Dark Energy Universe Simulation - Parallel Universe Runs (DEUS-PUR) introduced by [67] [1]. Each simulation started from a given realization of the initial matter density field and cosmological parameters shown in

[1] Set C was not directly presented in [67] but it was performed at the same time for the same project.

parameters	
H_0	72
Ω_Λ	$1 - \Omega_\mathrm{m}$
Ω_m	0.2573
σ_8	0.801
n_s	0.963

Table 2: Cosmological parameters used in the simulations with RAMSES code.

	HR	LR
Set	B	C
Number of realizations	96	512
Box size [h^{-1}Mpc]	656.25	1312.5
Number of particles	1024^3	512^3
Particle [$h^{-1}\mathrm{M}_\odot$]	1.88×10^{10}	1.20×10^{12}
Initial redshift (z_ini)	190	106
Output redshifts	$z = 1,\ 0$	$z = 1,\ 0.5,\ 0$

Table 3: Parameters of N-body simulation sets used in the simulations.

Table 4.4.1. The initial conditions were generated with an improved version of MPGRAFIC [36] while the particles evolution were computed with an optimized version of the RAMSES N-body code [35]. The main characteristics of the two ensembles of simulations are summarized in Table 3. Set B consists in 96 simulations with 1024^3 particles in a cosmological volume of $(656.25\ h^{-1}\mathrm{Mpc})^3$. The total effective volume is 27 $(h^{-1}\mathrm{Gpc})^3$ and the mass resolution is $1.88 \times 10^{10}\ h^{-1}\mathrm{M}_\odot$. We call this set HR ("High Resolution"). Set C consists in 512 simulations with 512^3 particles in a cosmological volume of $(1312.5\ h^{-1}\mathrm{Mpc})^3$. The total effective volume of 1158 $(h^{-1}\mathrm{Gpc})^3$ is larger but the mass resolution of $1.20{\times}10^{12}\ h^{-1}\mathrm{M}_\odot$ is more limited. We call this set LR ("Low Resolution"). The two sets are complementary because they are affected at different level by numerical effects such as sample variance, finite volume and mass resolution effects (see Refs [67, 68] for a study of these effects).

The matter bispectrum is estimated using the BISP_MES code [37] kindly provided by S.Colombi. The code has been updated to take into account redshift space distortions (RSD) and projections onto multipoles. We provide here a short summary of the numerical methods, for more details see [37]. Particles position and velocity from a given snapshot are

provided as an input of the code. Particles position are then displaced along the $\hat{z}$-direction of the box using Eq. (60). When a particle falls outside of the simulation box, periodic boundary conditions are assumed to ensure conservation of the total number of particles. The density in Fourier-space is then computed using Cloud-In-Cell (CIC) mass assignment followed by a Fast Fourier Transform (FFT). The density field is further deconvolved with the CIC window function. We call the resulting density field from a given snapshot of the j-th simulation of a set, $\delta_{\mathrm{sim,j}}$. For triangles with sides k_1, k_2 and k_3, the multipole moments of the bispectrum are computed by a projection onto Legendre polynomials followed by an averaging over an homogeneous sample of modes within a bin of size Δk_1, Δk_2 and Δk_3 centered on k_1, k_2 and k_3. The averaging procedure is performed by randomly picking N_{mode} possible orientations and sizes of triangles within this interval (Monte-Carlo method). The estimated multipole projection of the bispectrum for a given snapshot of the j-th simulation is then given by

$$B^{(s)}_{\ell,\mathrm{sim,j}}(k_1,k_2,k_3) = \frac{1}{N_{\mathrm{mode}}}\sum_{i=1}^{N_{\mathrm{mode}}} \delta^{(s)}_{\mathrm{sim,j}}(\boldsymbol{k}_1^i)\delta^{(s)}_{\mathrm{sim,j}}(\boldsymbol{k}_2^i)\delta^{(s)}_{\mathrm{sim,j}}(\boldsymbol{k}_3^i)\mathcal{P}_\ell(\mu^i), \tag{153}$$

where the subscript i indicates the rank of the orientation/size of the triangle.

The number of orientations/sizes N_{mode} used for the averaging procedure is set to 10^7. With such a large value, the results are insensitive to the exact choice of N_{mode}. The size of the bin is chosen to be equal to the fundamental frequency of the box. We also use an FFT grid with 512^3 elements. The corresponding Nyquist frequency is 2.45 h Mpc^{-1} (1.23 h Mpc^{-1}) for the HR (LR) simulation. As a consequence, we do not apply any shot noise corrections nor any aliasing corrections since such effects are negligible at the scale of interest in this thesis ($k < 0.3$ h Mpc^{-1}). However, at the very large scales of interest for comparison to perturbation theory ($k = 0.01 - 0.1$ h Mpc^{-1}), HR simulations might suffer from non-negligible finite-mode sampling [69]. In the linear regime, the bispectrum of the density field should be zero for perfect ensemble average. Because the total number of independent modes in the simulation is finite, the resulting bispectrum is non-zero. To mitigate this effect at large scales, we compute the initial bispectrum of each snapshot $B^{(s)}_{\ell,\mathrm{ini,j}}$. The linearly evolved bispectrum is then subtracted from the snapshot bispectrum to obtain a corrected bispectrum $B^{(s)}_{\ell,\mathrm{corr,j}}$. The linearly evolved bispectrum is computed using Eq. (153) but instead of using the snapshot density $\delta^{(s)}_{\mathrm{sim,j}}(\boldsymbol{k}^i)$, we use the linearly evolved

density field

$$\delta^{(s)}_{\mathrm{linevol,j}}(\boldsymbol{k}^i, z) = \frac{1 + f(z)\mu^2}{1 + f(z_{\mathrm{ini}})\mu^2} \frac{D(z)}{D(z_{\mathrm{ini}})} \times \delta^{(s)}_{\mathrm{sim,j}}(\boldsymbol{k}^i, z_{\mathrm{ini}}), \tag{154}$$

where $f(z)$ is the linear growth rate and $D(z)$ is the linear growth factor. This correction plays a role at the percent level at small k ($k < 0.1\ h\ \mathrm{Mpc}^{-1}$) for the HR run.

For each snapshot we consider isosceles triangles ($k_1 = k_2$) and scalene triangles ($k_1 = 2k_2$). For each type of triangle, we explore the scale dependence by fixing θ_{12} and varying k_1 and the shape dependence by fixing k_1 and varying θ_{12}. Once the bispectrum is computed for all simulations of a given set, we perform an ensemble average of $B^{(s)}_{\ell,\mathrm{corr,j}}(k_1, k_2, k_3)$ to get the mean bispectrum of the set

$$B^{(s)}_{\ell,\mathrm{sim}}(k_1, k_2, k_3) = \frac{1}{N_{\mathrm{sim}}} \sum_{j=1}^{N_{\mathrm{sim}}} B^{(s)}_{\ell,\mathrm{corr,j}}(k_1, k_2, k_3), \tag{155}$$

where N_{sim} is the number of simulations of the set. This bispectrum estimate is the one used in the rest of the thesis. We also compute the standard error of the bispectrum and we estimate statistical error bars assuming[2]

$$\Delta B^{(s)}_{\ell,\mathrm{stat}} = \frac{\sqrt{\frac{1}{N_{\mathrm{sim}}} \sum_{j=1}^{N_{\mathrm{sim}}} B^{(s)}_{\ell,\mathrm{corr,j}}(k_1, k_2, k_3)^2 - B^{(s)}_{\ell,\mathrm{sim}}(k_1, k_2, k_3)^2}}{\sqrt{N_{\mathrm{sim}}}}. \tag{156}$$

The same analysis is repeated in comoving space (i.e. no redshift space distortions) by setting the velocity field and linear growth rate to zero.

4.4.2 Results in real space

Let us first look at the results in real space and check the applicable range of PT as well as the quality of N-body data.

Fig. 10 shows the power spectra at $z = 1$ (top), 0.5 (middle) and 0 (bottom). Left panel plots the power spectra multiplied by $k^{3/2}$, while the right panel summarizes their fractional difference, for which we take the predictions by the Emulator code [70, 71, 72, 73] as the base value, and evaluate $[P(k) - P_{\mathrm{Emu}}(k)]/P_{\mathrm{Emu}}(k)$ with P_{Emu} being the Emulator power spectrum. Note here that the error bars in the N-body results indicate the standard error of

[2]Multiplying the expression of Eq. (156) by $\sqrt{N_{\mathrm{sim}}/(N_{\mathrm{sim}} - 1)}$ decreases the bias in the estimate of the standard error. However, we think that our realizations are enough to neglect -1.

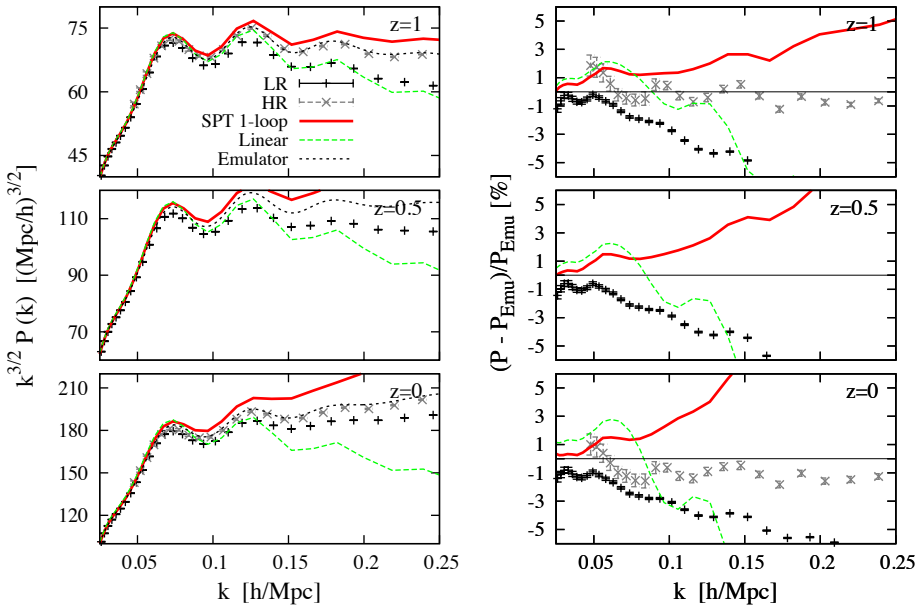

Figure 10: Real-space power spectrum as function of wave number k at $z = 1$ (top), 0.5 (middle) and 1 (bottom). The left panel plots the power spectrum multiplied by $k^{3/2}$, while the right panel shows the fractional difference between the emulator and other predictions, $(P - P_{\rm Emu})/P_{\rm Emu}$. In each panel, black and gray points with errorbars indicate the results of LR and HR simulations, respectively. The green dashed and red solid lines are the linear theory and the standard PT one-loop predictions. The black dashed lines in the left panels are the prediction based on the cosmic emulator [70, 71, 72, 73]. This figure is taken from Ref. [47].

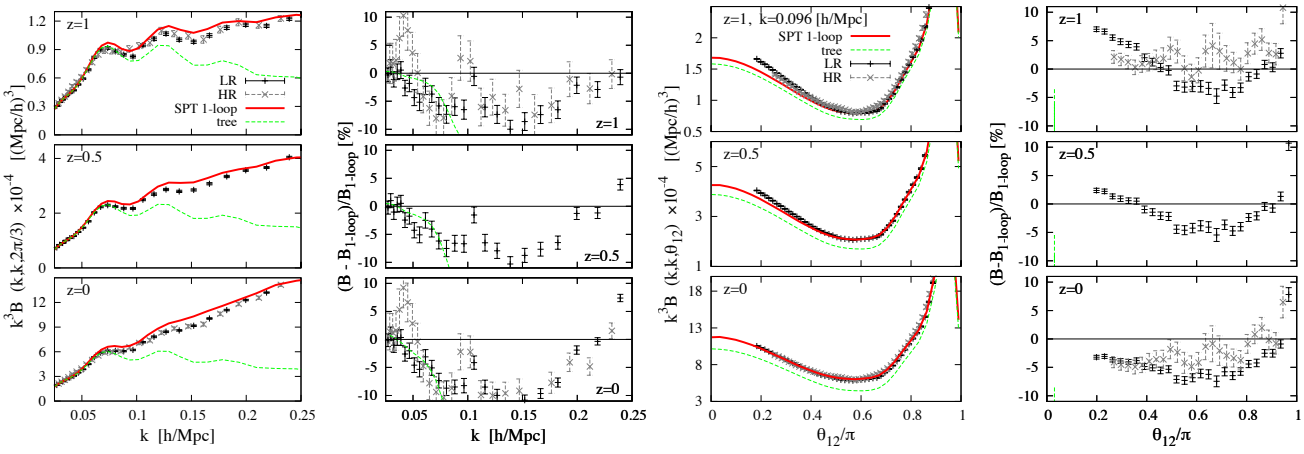

Figure 11: Real-space bispectrum in real space at $z = 1$ (top), 0.5 (middle), and 0 (bottom). The first two panels from the left show the results for equilateral triangular shape (i.e., $k_1 = k_2 = k_3 = k$), plotted as function of wave number k. The leftmost panel is the bispectrum amplitude multiplied by k^3, while the second panel plots the fractional difference between standard PT one-loop predictions and others, i.e., $(B - B_{\rm 1\text{-}loop})/B_{\rm 1\text{-}loop}$. The right two panels also present the results similarly to the left two panels, but the cases with isosceles triangular shape ($k_1 = k_2$) are plotted as function of the angle $\theta_{12} \equiv \cos^{-1}(\hat{\boldsymbol{k}}_1 \cdot \hat{\boldsymbol{k}}_2)$, fixing the scale $k_1 = k_2$ to $0.096\,h\,{\rm Mpc}^{-1}$. In each panel, meanings of the symbols and line types are the same as in Fig. 10, except for the green dashed lines, which indicate the standard PT prediction at tree-level order.This figure is taken from Ref. [47].

the averaged power spectrum over the number of realizations. The claimed error bars of the Emulator are 1%.

The PT predictions at one-loop order (red) reasonably agree with those of the emulator code, and the agreement is at the 3 percent level for the scales of $k \lesssim 0.18$, 0.12 and $0.1\,h\,\mathrm{Mpc}^{-1}$ at $z = 1$, 0.5 and 0, respectively. This is consistent with what has been found in the literature. The high-resolution N-body data (HR) also shows a reasonable agreement with the emulator (1 percent level over all the studied range of wavenumber) and one-loop PT predictions, but the low-resolution data (LR) systematically deviates from others at small scales. The deviation gradually increases from about 0.5 percent near $k = 0.05\,h\,\mathrm{Mpc}^{-1}$) to 5 percent near $k = 0.2\,h\,\mathrm{Mpc}^{-1}$. This is a well known mass-resolution effect which tends to decrease the power at small scale [70, 68, 74]. We refer to Ref. [68] for a dedicated section about statistical and systematics errors on the matter power spectrum with a similar simulation set-up as the one used in this thesis.

On the other hand, turning to look at the real-space bispectrum, we do not clearly see the systematic difference between HR and LR simulations. Fig. 11 shows the results for the equilateral triangular shapes plotted as function of k (left two panels), and those for the isosceles triangles plotted as function of $\theta_{12} \equiv \cos^{-1}(\hat{\boldsymbol{k}}_1 \cdot \hat{\boldsymbol{k}}_2)$ (right two panels). Note that in panels showing the amplitude of bispectrum, the results are all multiplied by k^3. Also, in plotting the fractional difference (second left and rightmost panels), we take the one-loop PT predictions as the base model, and evaluate the ratio, $(B - B_{1\text{-loop}})/B_{1\text{-loop}}$.

Compared to the power spectrum case, the statistical errors in N-body simulations is larger, and the difference between the two data set can be seen only at large scales $k \lesssim 0.05\,h\,\mathrm{Mpc}^{-1}$. Rather, there seems to be a systematic difference between simulations and PT prediction, and because of this, the agreement between simulations and PT prediction look somewhat worse, and is at 5% level even at the scales where the reasonable agreement at a few percent level can be seen in the power spectrum. Perhaps, these results might be partly ascribed to the setup of initial conditions (early starting redshift) or to the overestimate of non-linear effects on the bispectrum by standard PT, but without any reference, it is difficult to further clarify the origin of systematics. We will leave it to future investigation. Nevertheless, one important point is that the one-loop PT predictions can capture the major trend in the N-body simulations at small scales; scale-dependent enhancement of the bispectrum amplitude at $k \gtrsim 0.05\,h\,\mathrm{Mpc}^{-1}$. Because of this, the agreement still remains at the $5 - 10\%$ level even at small scales at all redshifts.

Keeping the systematics and a level of agreement in the real space in mind, we will move to the redshift space, and continue the comparison in next subsection.

4.4.3 Results in redshift space

To see the impact of FoG damping on the bispectrum, we first compare the standard PT predictions with results of N-body simulations.

Figs. 12 and 13 respectively show the scale- and shape-dependencies of the bispectrum for equilateral and isosceles configurations. Based on the definition of multipole expansion in Eq. (152) and Appendix B, we compute and measure the monopole and quadrupole moments of the bispectrum, which are respectively plotted in left and right panels. Overall, the N-body results both from the LR and HR data agree well each other. A closer look at $k \gtrsim 0.1\,h\,\mathrm{Mpc}^{-1}$ reveals that the amplitude of the LR data is systematically larger than that of the HR data, but within the errorbars there is no significant discrepancy in both monopole and quadrupole moments. Rather, a discrepancy between the N-body results and PT predictions is manifest, and compared to the results in real space, the range of agreement is fairly narrower for standard PT one-loop, and is restricted to a low-k region. This is rather manifest at higher redshifts, and the prediction generally overestimates the simulations. On the other hand, shifting the overall amplitude, the shape dependence predicted by standard PT one-loop seems to reasonably match the measured results of N-body simulations (see Fig. 13). The results clearly manifest that a naive standard PT fails to describe the damping behaviors seen in the N-body simulations, and an appropriate prescription for the damping effect is important for prediction even at large scales.

Let us then see how the PT model presented in Chap. 4.3 works well. In doing so, an appropriate functional form of D_{FoG} needs to be first specified. The function D_{FoG} is generally expressed as function of $k_1\mu_1$, $k_2\mu_2$, and $k_3\mu_3$, and it contains the non-perturbative damping behavior arising from the exponential factor, $\exp\{\langle e^{j_4A_4+j_5A_5}\rangle_c\}$ [see Eq. (133) and proposition (i) in Chap. 4.3]. Here, we adopt the following Gaussian form as a simple and relevant ansatz, similar to what has been frequently used in the power spectrum cases [11]:

$$D_{\mathrm{FoG}} = \exp\left[-\frac{1}{2}(f\,\sigma_{\mathrm{v}})^2\left\{(k_1\mu_1)^2 + (k_2\mu_2)^2 + (k_3\mu_3)^2\right\}\right]. \tag{157}$$

The function f is the linear growth rate, and σ_v is the constant parameter corresponding to the one-dimensional velocity dispersion, which controls the strength of the FoG damping. Note that similar functional form is obtained by expanding the exponential pre-factor and

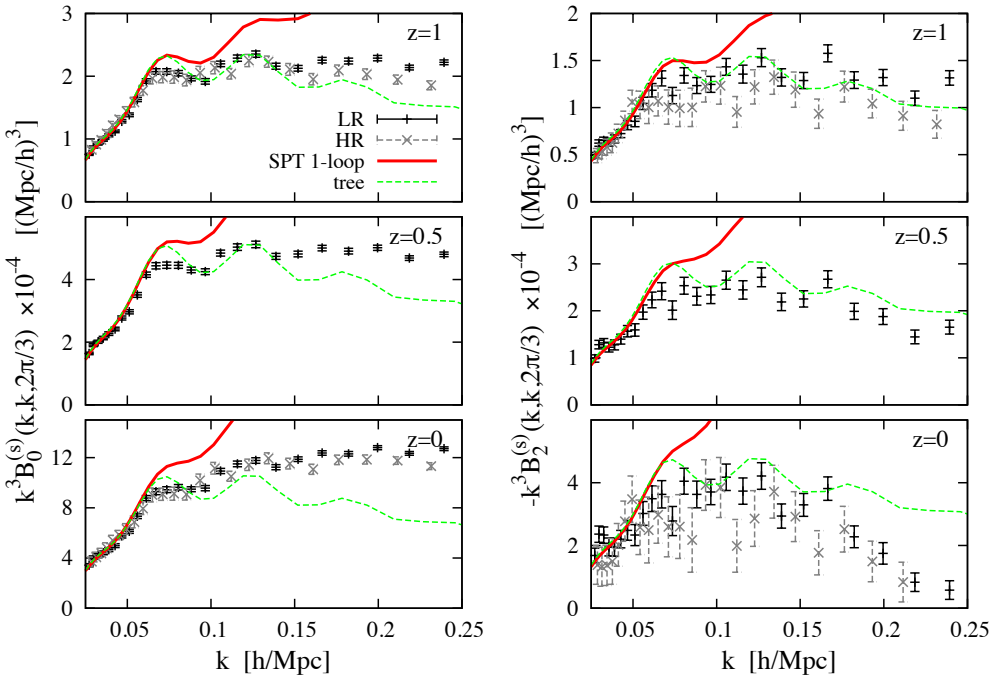

Figure 12: Monopole (left) and quadrupole (right) moments of the redshift-space bispectrum for the equilateral triangles, plotted as function of wave number k at $z = 1$ (top), 0.5 (middle), and 0 (bottom). The standard PT predictions at tree-level (green dashed) and one-loop (red solid) order are compared with the measured bispectrum from LR (black) and HR (gray) data of N-body simulations. The results for equilateral shape triangles are particularly shown. This figure is taken from Ref. [47].

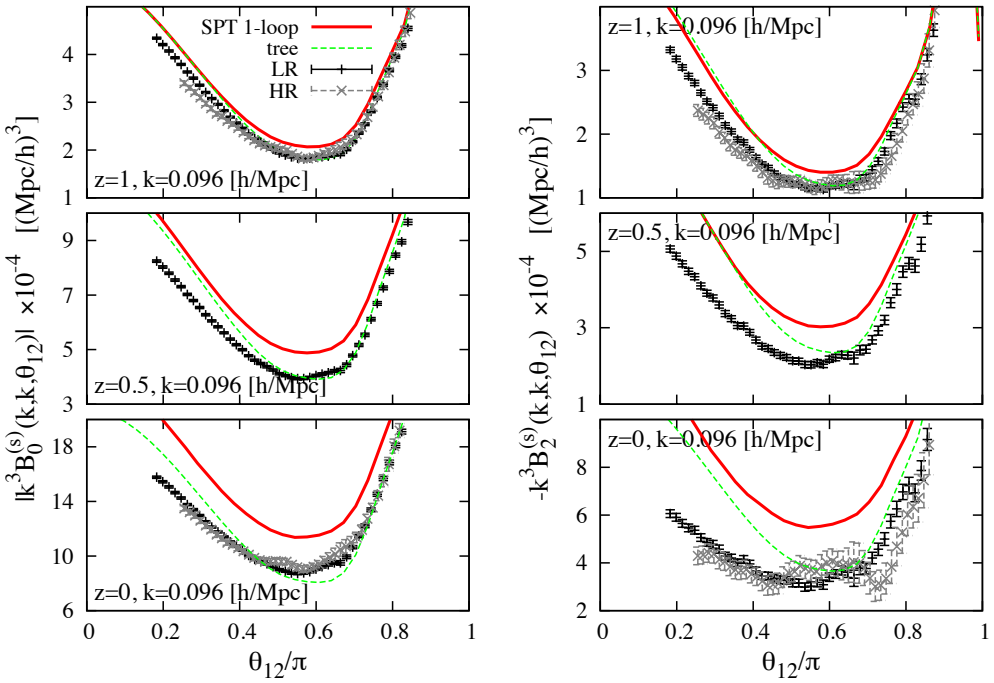

Figure 13: Same as Fig. 12, but the shape-dependence of the bispectrum is plotted as function of $\theta_{12} = \cos^{-1}(\hat{\boldsymbol{k}}_1 \cdot \hat{\boldsymbol{k}}_2)$, fixing both k_1 and k_2 to $0.096\,h\,\mathrm{Mpc}^{-1}$. The meanings of the line types are the same as in Fig. 12. This figure is taken from Ref. [47].

truncating it at the second-order in cumulants, just ignoring the spatial correlation. A non-trivial point may be whether $D_{\rm FoG}$ is still expressed as univariate function of $(k_1\mu_1)^2 + (k_2\mu_2)^2 + (k_3\mu_3)^2$ or not beyond the scales relevant for tree-level predictions. We will discuss and check it in Chap. 4.4.4.

Adopting Eq. (157), Figs. 14-17 compare the prediction of the PT model with N-body simulations. While Figs. 14 and 15 show the scale-dependence of the bispectrum amplitudes for equilateral ($k_1 = k_2 = k_3$) and scalene triangular configuration with $k_1 = 2k_2 = (2/\sqrt{3})k_3$, Figs. 16 and 17 respectively plot the shape-dependence of the bispectrum as function of $\theta_{12} = \cos^{-1}(\hat{\boldsymbol{k}}_1 \cdot \hat{\boldsymbol{k}}_2)$ for the triangles of $k_1 = k_2$ and $k_1 = 2k_2$. In each figure, the monopole and quadrupole moments of the bispectrum are computed/measured according to the definition in Appendix B, and the results are presented in left and right panels, respectively. Here, the measured results of the bispectra are shown only for LR data, since no notable difference has been found in both LR and HR data.

Overall, the one-loop PT model depicted as magenta solid lines better agree with simulations over a wider range of k as well as for a wide range of shapes. Note that the free parameter $\sigma_{\rm v}$ in Eq. (157) is determined at each redshift by fitting the predicted monopole and quadrupole moments with measured results of N-body simulations at the range $[k_{\rm min}, k_{\rm max}]$. While $k_{\rm min}$ is set to $0.05\,h\,{\rm Mpc}^{-1}$, we adopt $k_{1\%}$ defined by Ref. [75] as the maximum wavenumber $k_{\rm max}$, indicated by the vertical arrow in each panel of Figs. 14 and 15 (blue for tree-level PT and red for one-loop PT). The $k_{1\%}$ indicates the maximum wavenumber below which the predicted power spectrum is shown to well reproduce the N-body result within 1% accuracy in the real space, and from Fig. 11, we see that the $k_{1\%}$ also gives a good indicator for the applicable range of one-loop bispectrum in real space. Because the deviations between PT and simulations do not behave as a monotonous function it is however hard to extract an exact scale. This is why we rely on more accurate power spectrum measurements to define $k_{1\%}$. The fitted result of the parameter $\sigma_{\rm v}$ is given in left panel of each figure, which are close to the linear theory prediction of one-dimensional velocity dispersion (see also Tables 4, 5, Figs. 18 and 19).

A notable point may be that the one-loop PT model reproduces the N-body results even beyond the fitting range of $\sigma_{\rm v}$. For comparison, in Figs. 14-17, we have also plotted the

		$P^{(s)}_{\rm model}$: 1-loop	$B^{(s)}_{\rm model}$: 1-loop		
z	$k_{\rm max}$		$k_1 = k_2 = k_3$	$k_1 = 2k_2 = (2/\sqrt{3})k_3$	$\sigma_{\rm v,lin}$
1	0.13	4.3 ± 0.1 (4.2 ± 0.04)	4.9 ± 0.3 (5.9 ± 0.3)	4.0 ± 0.2 (4.3 ± 0.3)	3.8
0.5	0.1	5.9 ± 0.1	7.8 ± 0.4	6.3 ± 0.3	4.8
0	0.08	8.8 ± 0.3 (9.8 ± 0.3)	13 ± 0.8 (15 ± 1.0)	10 ± 0.6 (9.1 ± 1.1)	6.1

Table 4: Fitted values of $\sigma_{\rm v}$ given in Eq. (157) from 1-loop models of power spectrum and bispectrum. The results are obtained by fitting the monopole and quadrupole predictions of PT models to the measured results from the LR (HR) data of N-body simulations, and are listed in units of h Mpc^{-1}. For reference, the rightmost column shows the linear theory predictions.

		$B^{(s)}_{\rm model}$: tree		
z	$k_{\rm max}$	$k_1 = k_2 = k_3$	$k_1 = 2k_2 = (2/\sqrt{3})k_3$	$\sigma_{\rm v,lin}$
1	0.09	6.1 ± 0.2	6.5 ± 0.1	3.8
0.5	0.07	9.0 ± 0.3	9.5 ± 0.2	4.8
0	0.06	13 ± 0.6	15 ± 0.4	6.1

Table 5: Same as Fig. 5, but the results for tree bispectrum model

tree-level standard PT predictions multiplied by the damping function of Eq. (157)[3], depicted as blue short-dashed lines, but the agreement with N-body simulations is restricted to the fitting range indicated by the blue vertical arrow. In this respect, the one-loop corrections play an important role, together with damping function, to better describe the redshift-space bispectrum at weakly non-linear regime. A closer look at the equilateral case in Fig. 14 reveals that the agreement of the one-loop model is bit degraded compared to the scalene case (Fig. 15), especially for the quadrupole moment. Similar trend is also found for the shape dependence in Figs. 16 and 17. This is partly because for a fixed wavenumber k, one of the side length for the triangle becomes smaller or larger than k, and the results can be less or more sensitive to the nonlinearity of the gravitational clustering and RSD. Indeed, for the cases shown in Figs. 15 and 17, the tree-level PT predictions get closer to the one-loop PT results at large scales.

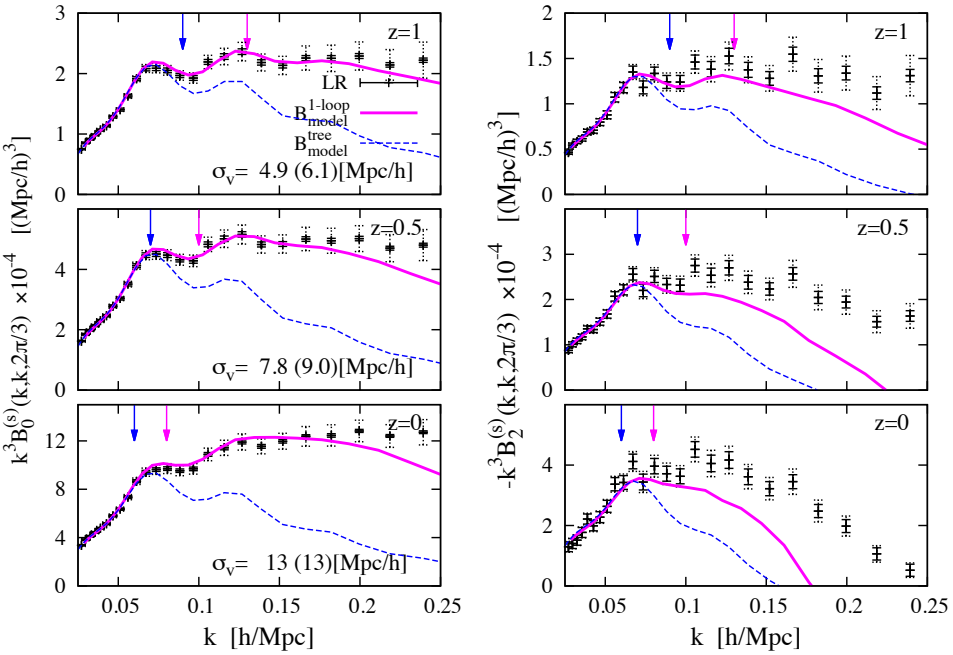

Figure 14: Monopole (left) and quadrupole (right) moments of the redshift-space bispectrum for the equilateral triangles, plotted as function of wave number k at $z = 1$ (top), 0.5 (middle), and 0 (bottom). Here, the PT models involving the damping function $D_{\rm FoG}$ are compared with the measured results obtained from the LR data of N-body simulations. The predictions of tree- and one-loop PT model are depicted as blue dashed and magenta solid lines, respectively. In plotting the predictions, the free parameter $\sigma_{\rm v}$ in the damping function is determined by fitting the monopole and quadrupole moments to the N-body data at $0.05\,h\,{\rm Mpc}^{-1} \leq k \leq k_{\rm max}$, with $k_{\rm max}$ indicated by the vertical arrows in each panel. Note that the error bars depicted as solid and dotted lines respectively represent the statistical error averaged over the number of realizations, and the one including both the statistical and systematic errors (see Chap. 4.4.4). This figure is taken from Ref. [47].

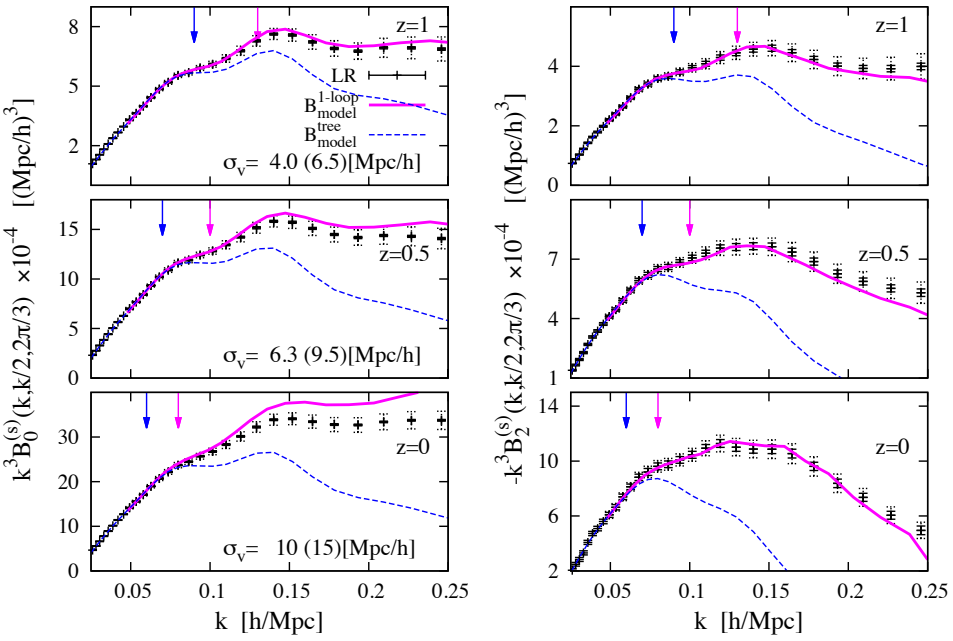

Figure 15: Same as Fig. 14, but the results for scalene triangle of $k_1 = 2k_2 = (2/\sqrt{3})k_3 = k$ are shown. This figure is taken from Ref. [47].

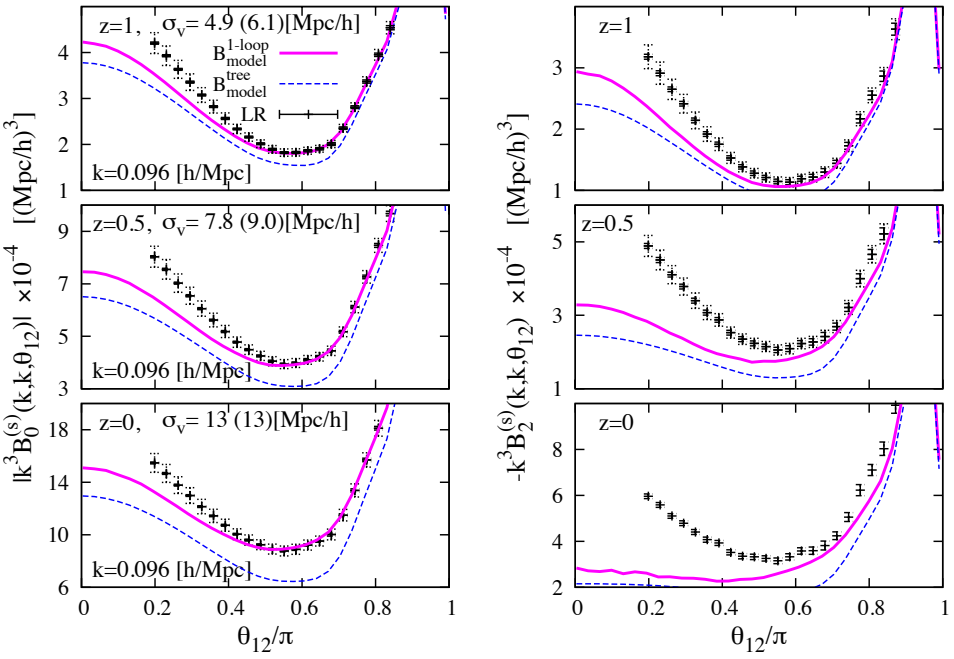

Figure 16: Same as Fig. 14, but here the shape dependence of the bispectrum for isosceles triangle ($k_1 = k_2$) is plotted as function of $\theta_{12} = \cos^{-1}(\hat{\boldsymbol{k}}_1 \cdot \hat{\boldsymbol{k}}_2)$, fixing the scale of k_1 and k_2 to $0.096\,h\,\mathrm{Mpc}^{-1}$. Here, in plotting the predictions of PT models, we adopt the fitted results of σ_v obtained from Fig. 14. This figure is taken from Ref. [47].

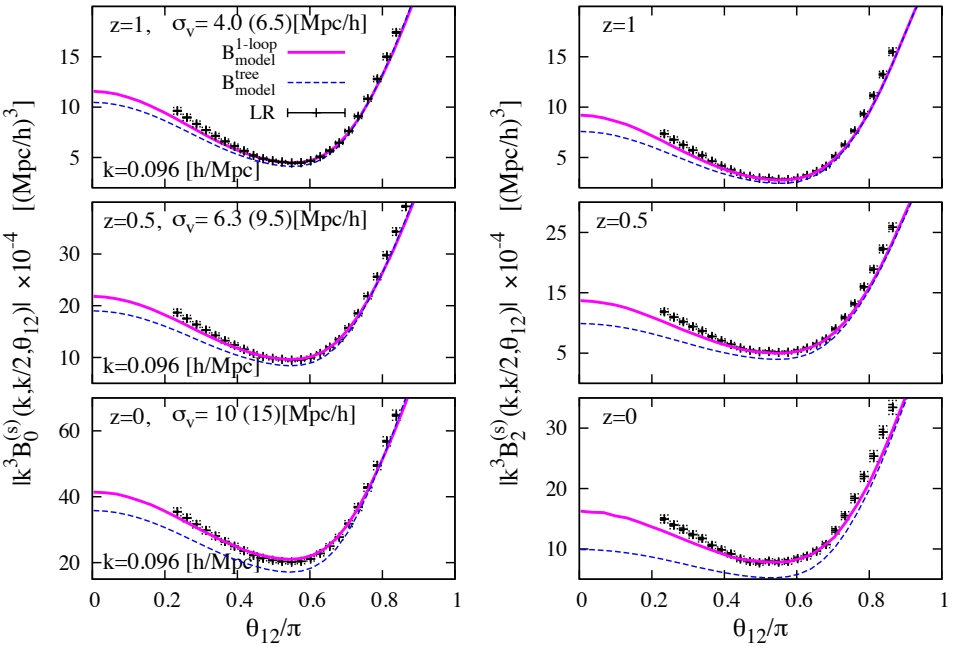

Figure 17: Same as Fig. 16, but the results for another triangular shape with $k_1 = 2k_2$ are shown, again fixing k_1 and $2k_2$ to $0.096\,h\,\mathrm{Mpc}^{-1}$. Here, in plotting the predictions of PT models, we adopt the fitted results of σ_v obtained from Fig. 15. This figure is taken from Ref. [47].

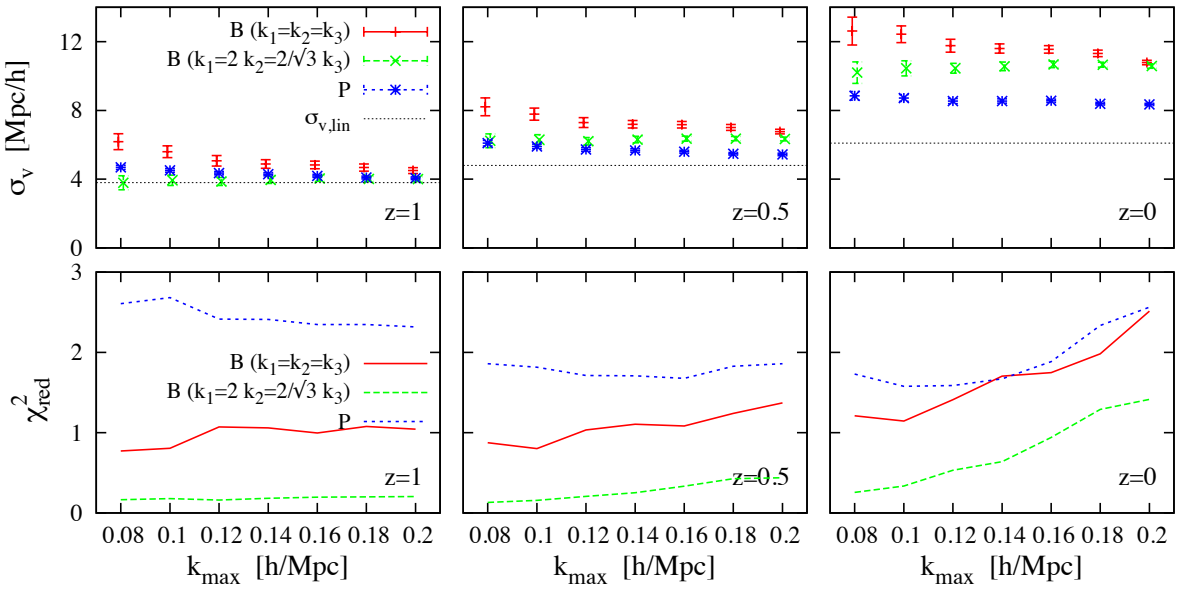

Figure 18: Dependence of the fitted results of parameter σ_v (top), and the reduced chi-square (bottom) on the maximum wavenumber $k_{\rm max}$ at $z = 1$ (left), 0.5 (middle), and 0 (right). Red and green symbols respectively represent the results from the bispectrum for equilateral and scalene shape with $k_1 = 2k_2 = (2/\sqrt{3})k_3$. On the other hand, blue symbols are obtained from TNS model by Ref. [11]. Note that all the results are obtained by fitting the one-loop PT model predictions to the measured results from LR data of N-body simulations. This figure is taken from Ref. [47].

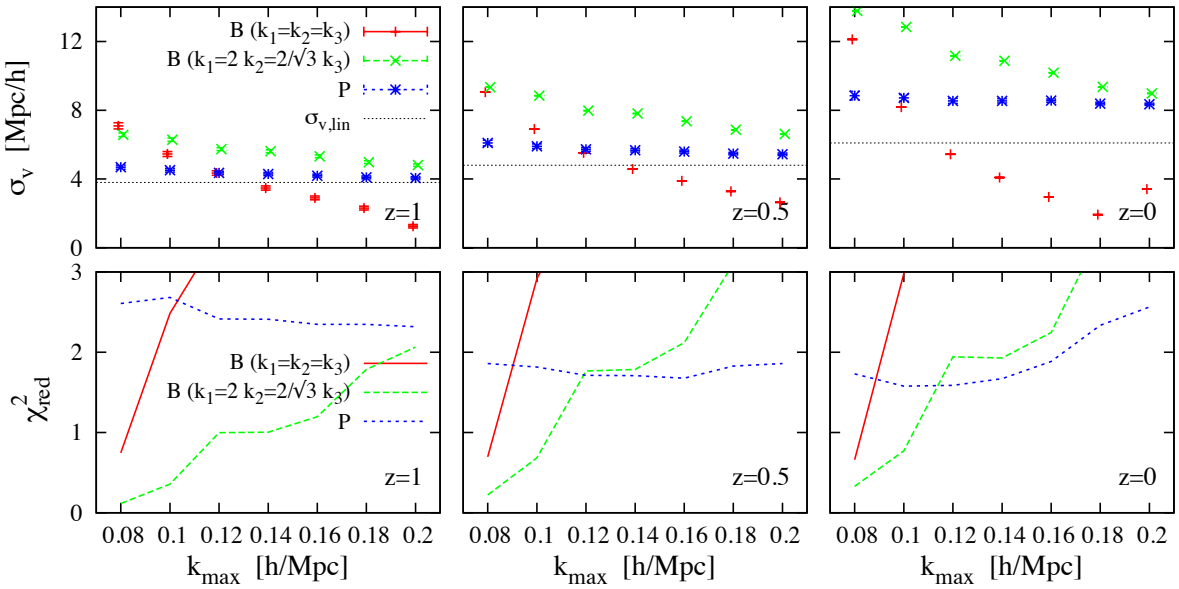

Figure 19: Same as in Fig. 18, but the results obtained by fitting the tree-level PT model predictions to the N-body data are shown. Meanings of the lines and symbols are the same as in Fig. 18. This figure is taken from Ref. [47].

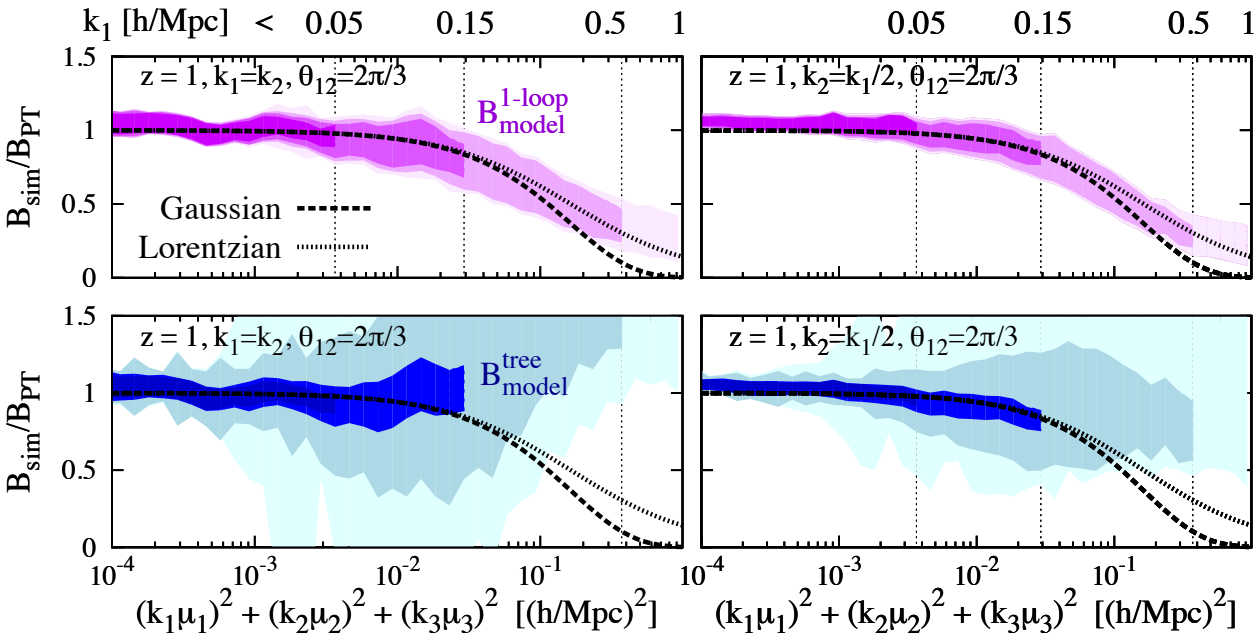

Figure 20: Ratio of the redshift-space bispectrum measured from the LR data and to the one-loop (top) and tree-level (bottom) PT models, setting $D_{\rm FoG}$ to unity (or equivalently, taking the limit $\sigma_{\rm v} \to 0$). Here, without applying multipole expansion, the ratio is evaluated for various orientation of the triangle, and the scatters of the estimated results are shown as color shaded regions, fixing the equilateral shape (left) and scalene shape with $k_1 = 2k_2 = (2/\sqrt{3})k_3$ (right). The resultant ratio is then plotted against $(k_1\mu_1)^2 + (k_2\mu_2)^2 + (k_3\mu_3)^2$. Note that the four different color strengths imply the length of k_1 used to estimate the ratio, indicated at the upper horizontal axis. For reference, Gaussian (dashed) and Lorentzian (dotted) forms of the damping function are also plotted. This figure is taken from Ref. [47].

4.4.4 Testing the ansatz of damping function

Adopting the Gaussian form of the non-perturbative damping function, we have seen that the PT model successfully describes the measured results of the bispectrum. However, the validity and consistency of the treatment have to be checked and/or verified, at least in the following two aspects. One is the consistency of the fitted values of $\sigma_{\rm v}$. Since the present PT model is constructed in similar manner to the TNS model in Ref. [11], the fitted values of the parameter $\sigma_{\rm v}$ derived from bispectrum have to be consistent with those from the power spectrum. The other aspect is the functional form of the damping function. We have assumed in Eq. (157) that the damping function is expressed as the univariate function of $(k_1\mu_1)^2 + (k_2\mu_2)^2 + (k_3\mu_3)^2$, but this can be verified only at the leading-order, and have to be checked at the scales relevant for the one-loop PT.

Let us first discuss the consistency of the fitted value, $\sigma_{\rm v}$. Tables 4 and 5 summarize the results derived both from the bispectrum and power spectrum. The estimated results are based on the N-body simulations of the LR (HR) data, and we used the one-loop model for power spectrum, while for the bispectrum, the fitted results from two different configurations are presented in both tree-level and one-loop PT cases. The best-fitted values both from the power spectrum and bispectrum one-loop models reasonably agree with each other at $z = 1$. Although a deviation is manifest at lower redshifts, this is small compared to the cases with tree-level predictions of bispectrum.

To see the robustness of the fitted values, we extend the analysis in Tables 4 and 5, and using the LR data, we examine the fitting in various range of k. The results are shown in Figs. 18 and 19. In each figure, top and bottom panels respectively plot the fitted values $\sigma_{\rm v}$ and the reduced χ^2 as function of $k_{\rm max}$. Note that in estimating $\chi^2_{\rm red}$ and the errors of the fitted $\sigma_{\rm v}$, we took account of the systematics in the N-body simulations. That is, at each data point, we added the systematic errors $\Delta P^{(\rm s)}_{\ell,\rm sys}$ and $\Delta B^{(\rm s)}_{\ell,\rm sys}$ to the statistical errors of the power spectrum and bispectrum multipoles, $\Delta P^{(\rm s)}_{\ell,\rm stat}$ and $\Delta B^{(\rm s)}_{\ell,\rm stat}$, as shown in Figs. 14-17 for the bispectrum case (solid error bars: $\Delta B^{(\rm s)}_{\ell,\rm stat}$, dotted error bars: $\Delta B^{(\rm s)}_{\ell,\rm stat} + \Delta B^{(\rm s)}_{\ell,\rm sys}$). The size of the systematics is estimated from the real-space results in Figs. 10 and 11. We assume that the relative systematics in redshift space for the power spectrum and bispectrum are proportional to the relative systematics in real space for the matter power spectrum,

[3] In terms of the descriptions given in Chap. 4.3, the tree-level standard PT multiplied by $D_{\rm FoG}$ corresponds to the leading-order PT calculations of Eq. (148) with the functions C_n summing up to $n = 2$.

$\Delta P_{\rm sys}/P_{\rm sim} = |P_{\rm sim} - P_{\rm ref}|/P_{\rm sim}$, where $P_{\rm sim}$ represents the measured real-space power spectrum in N-body simulations, and $P_{\rm ref}$ is our reference for the real-space power spectrum. For the reference, we choose the emulator power spectrum (although the estimated systematics is of order 1 percent, we neglect this contribution). The systematics for the power spectrum and bispectrum in redshift space are estimated as,

$$\frac{\Delta P^{(\rm s)}_{\ell,\rm sys}(k_a)}{P^{(\rm s)}_{\ell,\rm sim}(k_a)} = \alpha \frac{\Delta P_{\rm sys}(k_a)}{P_{\rm sim}(k_a)}, \tag{158}$$

$$\frac{\Delta B^{(\rm s)}_{\ell,\rm sys}(k_1,k_2,k_3)}{B^{(\rm s)}_{\ell,\rm sim}(k_1,k_2,k_3)} = \beta \sqrt{\frac{1}{3}\sum_{a=1}^{3}\left(\frac{\Delta P_{\rm sys}(k_a)}{P_{\rm sim}(k_a)}\right)^2}, \tag{159}$$

where α and β are two fudge factors that we have fixed to $\alpha \sim 1$ and $\beta \sim 1$. We have checked that at large-k (where statistical error bars are small compared to systematics), Eq. (159) reproduces the order of magnitude of the relative difference between the bispectrum of the HR set and the LR set (which is affected by mass resolution effect).

The rough systematic errors adopted here may result in a rather crude estimate of the goodness of fit, and thus the derived $\chi^2_{\rm red}$ can only be used for a comparison between tree-level and one-loop results in Fig. 18 and 19. Nevertheless, we see that the fitting results in one-loop PT cases are basically stable against the variation of $k_{\rm max}$, and the estimated values of $\chi^2_{\rm red}$ are smaller than those in the tree-level cases. Further, we checked that the (best-)fitted values of $\sigma_{\rm v}$ are robust against the systematic errors, and the resultant values in one-loop PT reasonably agree well with each other, especially at $z = 1$. Although the deviation becomes manifest at lower redshift, this would be probably due to the break down of the one-loop predictions. In fact, the $\chi^2_{\rm red}$ systematically increases with $k_{\rm max}$, indicating that the fitting starts to fail. Thus, at least at the redshift $z = 1$, the one-loop PT models work fine, and the FoG damping is described with a single parameter.

Next consider the validity of the ansatz for $D_{\rm FoG}$ at Eq. (157). To clarify whether the non-perturbative part is described by the univariate function or not, we directly measure the bispectrum, not applying the multipole expansion. In this case, the bispectrum in redshift space is described by the five variables. For each shape and orientation of the bispectrum, we compute the corresponding PT prediction based on Eq. (148) or (151), but setting $D_{\rm FoG}$ to 1. Taking the ratio gives

$$\frac{B^{(\rm s)}_{\rm sim}(k_1,k_2,\theta_{12},\omega,\phi)}{B^{(\rm s)}_{\rm model}(k_1,k_2,\theta_{12},\omega,\phi)\Big|_{D_{\rm FoG}=1}}. \tag{160}$$

At the scales where the one-loop PT is applicable, this ratio directly quantifies the functional form of $D_{\rm FoG}$, and thus we can check whether it is expressed as univariate function of $(k_1\mu_1)^2 + (k_2\mu_2)^2 + (k_3\mu_3)^2$ or not.

Fig. 20 shows the measured results of the ratio, Eq. (160), for various orientations at $z = 1$, plotted against $(k_1\mu_1)^2 + (k_2\mu_2)^2 + (k_3\mu_3)^2$. To be precise, what is shown here is the dispersion of the measured ratio depicted as shaded color region, and the four different color strengths imply the length of k_1 used to estimate the ratio: $k_1 \leq 0.05$, 0.15, 0.5, and $1\,h\,\mathrm{Mpc}^{-1}$ from dark to light. The results are compared with the univariate damping function of the Gaussian (dashed) and Lorentzian (dotted) form. Clearly, the scatter of the ratio for the one-loop PT model, given in top panel, is small, and its mean values fairly trace the univariate damping function. This is in marked contrast to the results for tree-level PT shown in bottom panel, where we see a large scatter. Further, the results seem robust irrespective of the shape of the bispectrum triangle, as seen in both left and right panels, where we respectively show the results for the equilateral case ($k_1 = k_2 = k_3$) and the scalene triangle with $k_1 = 2k_2 = (2/\sqrt{3})k_3$. A closer look at results suggests that Lorentzian form describes the measured ratio reasonably well at the high-k tail, although it is mostly the boundary where we can apply one-loop PT prediction. Hence, we conclude that the univariate ansatz for $D_{\rm FoG}$ is validated at least in the applicable range of one-loop predictions.

Chapter 5 Testing improved bispectrum template against simulation catalogs

In this chapter, toward future practical application of the improved model of redshift-space bispectrum developed in previous chapter, we here study how well we can get a robust and tight constraint on the gravity both from the power spectrum and bispectrum. For this purpose, we run a large number of N-body simulations and create mock matter/halo catalogs, with which we perform cosmological data analysis. Using the improved models of power spectrum and bispectrum, we carefully investigate how well these models reproduce the fiducial model parameters in the N-body simulations, especially focusing on the growth rate parameter. In doing this, one practical issue is the measurement of bispectrum from N-body simulation, which requires a time-consuming calculation based on the standard method. Hence, we first develop a fast estimation method for bispectrum, together with accelerated calculation method for theoretical template. Applying these methods, we analyze mock data from N-body simulation, and check if our model can properly reproduce the fiducial cosmological parameters. We also demonstrate the impact of combining power spectrum and bispectrum compared to the case using power spectrum alone.

5.1 Fast measurement of the bispectrum

Because the observable range of the universe is finite, available number of Fourier modes is limited, and we can not perform a rigorous statistical average with galaxy survey data. Nevertheless, we can estimate power spectrum and bispectrum from observation or simulation by taking average over finite number of Fourier modes. For a robust measurement of statistical quantity, we need to choose the estimator of statistical quantity in such a way that, for an infinite number of Fourier modes, the estimator is exactly reduced to what we want to measure, and the statistical fluctuation (i.e., variance) of it is minimized. Further, the estimator should be evaluated faster as much as possible in measuring the bispectrum from the data. Below, employing the bispectrum estimator developed by [76, 77], which

enable us to calculate quite faster than usual one by adapting FFT, we extend it to the measurement of bispectrum multipole shown in Fig. 9.

Following [77], we define the bispectrum estimator as:

$$\hat{B}_\ell(k_1, k_2, \theta_{12}) \equiv \frac{(2\ell+1)}{N^{\rm T}_{123}} \prod_{i=1}^{3} \int_{S_i} d^3\boldsymbol{p}_i \delta_{\rm D}(\boldsymbol{p}_1 + \boldsymbol{p}_2 + \boldsymbol{p}_3) \int \frac{d^3\boldsymbol{x}_i}{(2\pi)^3} \delta(\boldsymbol{x}_i) e^{-i\boldsymbol{p}_i\cdot\boldsymbol{x}_i} \mathcal{P}_\ell(\hat{q}\cdot\hat{x}), \quad (161)$$

where, S_i represents a linear bin around k_i with the width given by Δk, i.e., $k_i - \Delta k/2 \le p_i \le k_i + \Delta k/2$. The δ is the redshift-space density field measured from the data, $\hat{x}$ is the unit vector which points to the line-of-site direction, because we adapted the distant observer and plane-parallel approximation, we can take $\hat{x}$ as fixed direction $\hat{z}$ (see Eq.(64)). $\hat{q}$ is the unit vector which is used to define the multipole moment of bispectrum. The $N^{\rm T}_{123}$ is the number of triangles inside the shells S_1, S_2 and S_3, given by

$$N^{\rm T}_{123} = \int_{S_1} d^3\boldsymbol{p}_1 \int_{S_2} d^3\boldsymbol{p}_2 \int_{S_3} d^3\boldsymbol{p}_3 \delta_{\rm D}(\boldsymbol{p}_1 + \boldsymbol{p}_2 + \boldsymbol{p}_3). \quad (162)$$

Note here that the N_{123} depends on the wave numbers, k_1, k_2, and k_3.

In the N-body simulation and galaxy surveys, density fields are computed with particle distributions, and discreteness of the particles produces additional systematics in measuring statistical quantities, called shot noise. In the case of matter field, we can neglect the shot noise if we have a sufficient number of particles. However, in the case of halos, or galaxies, the shot noise becomes significant, and needs to be subtracted. To see the impact of the shot noise, we consider to discrete Fourier transform of the density perturbation:

$$\tilde{\delta}(k) \equiv \sum_{i=1}^{N} w_i e^{i\boldsymbol{k}\cdot\boldsymbol{x}_i}, \quad (163)$$

where, w_i is the weight for each object, and we choose $w_i = 1/N$ which gives the same weight for each object. The shot noise comes from the self pairs that appear in the summation over the product of the density perturbation.

In the case of monopole ($\ell = 0$), the above estimator is rewritten with:

$$\begin{aligned}\hat{B}_0(k_1, k_2, \theta_{12}) &= \frac{1}{N^{\rm T}_{123}} \prod_{i=1}^{3} \int_{S_i} d^3\boldsymbol{p}_i \int d^3\boldsymbol{r} e^{i(\boldsymbol{p}_1+\boldsymbol{p}_2+\boldsymbol{p}_3)\boldsymbol{r}} \tilde{\delta}(\boldsymbol{p}_i) - N^{\rm s}_0 \\ &= \frac{1}{N^{\rm T}_{123}} \prod_{i=1}^{3} \int d^3\boldsymbol{r} \mathcal{D}_{0,S_i}(\boldsymbol{r}) - N^{\rm s}_0, \end{aligned} \quad (164)$$

with the shot noise contribution $N_0^{\rm s}$ given by

$$N_0^{\rm s} = \frac{1}{N_{123}^{\rm T} N}\prod_{i=1}^{3}\int_{S_i} d^3\boldsymbol{p}_i \delta_{\rm D}(\boldsymbol{p}_1+\boldsymbol{p}_2+\boldsymbol{p}_3)[\tilde{\delta}(\boldsymbol{p}_1)\tilde{\delta}(-\boldsymbol{p}_1)+{\rm cyc}] - \frac{2}{N^2}$$
$$= \frac{1}{N_{123}^{\rm T} N}\int d^3\boldsymbol{r}[\mathcal{D}'_{0,S_1}(\boldsymbol{r})\mathcal{E}_{0,S_2}(\boldsymbol{r})\mathcal{E}_{0,S_3}(\boldsymbol{r})+{\rm cyc}] - \frac{2}{N^2}, \tag{165}$$

$$N_{123}^{\rm T} = \prod_{i=1}^{3}\int_{S_i} d^3\boldsymbol{p}_i \int d^3\boldsymbol{r} e^{i(\boldsymbol{p}_1+\boldsymbol{p}_2+\boldsymbol{p}_3)\boldsymbol{r}} = \prod_{i=1}^{3}\int d^3\boldsymbol{r}\mathcal{E}_{0,S_i}(\boldsymbol{r}) \tag{166}$$

$$\mathcal{D}_{0,S_i}(\boldsymbol{r}) \equiv \int_{S_i} d^3\boldsymbol{p}\tilde{\delta}(\boldsymbol{p})e^{i\boldsymbol{p}\cdot\boldsymbol{r}}, \tag{167}$$

$$\mathcal{D}'_{0,S_i}(\boldsymbol{r}) \equiv \int_{S_i} d^3\boldsymbol{p}|\tilde{\delta}(\boldsymbol{p})|^2 e^{i\boldsymbol{p}\cdot\boldsymbol{r}}, \qquad \mathcal{E}_{0,S_i}(\boldsymbol{r}) \equiv \int_{S_i} d^3\boldsymbol{p}e^{i\boldsymbol{p}\cdot\boldsymbol{r}}, \tag{168}$$

In the second line of Eq.(164) and (165), the Dirac delta function is rewritten with Fourier integral form, and decompose it into several pieces. Thanks to this decomposition, we can avoid a time-consuming operation for finding three-wave vectors satisfying triangular condition, and only require the three-times FFT to evaluate the estimator.

In the case of quadrupole moment ($\ell = 2$), there appears the differences arising from the definition of multipole expansion. In the paper by [77], he took $\hat{q}$ as $\hat{k}_1$, but in this thesis, we choose $\hat{q}$ as $\hat{r}_2$, as defined in Fig. 9. In this case, the Legendre polynomial becomes

$$\mathcal{P}_2(\hat{r}_2\cdot\hat{z}) = \frac{3}{2}\left\{\frac{k_{1x}k_{2y}-k_{1y}k_{2x}}{k_1k_2\sin\theta_{12}}\right\}^2 - \frac{1}{2}$$
$$= \frac{3}{2(k_1k_2\sin\theta_{12})^2}\left(k_{1x}^2k_{2y}^2 - 2k_{1x}k_{2y}k_{1y}k_{2x} + k_{1y}^2k_{2x}^2\right) - \frac{1}{2}. \tag{169}$$

Substituting Eq.(169) into Eq.(161) and subtructing the shot noise, we obtain the estimator of bispectrum quadrupole:

$$\hat{B}_2(k_1,k_2,\theta_{12}) = \frac{5}{N_{123}^{\rm T}}\int d^3\boldsymbol{r}\mathcal{D}_{0,S_3}(\boldsymbol{r})$$
$$\times\left[\frac{3}{2}\left\{\mathcal{D}_{xx,S_1}(\boldsymbol{r})\mathcal{D}_{yy,S_2}(\boldsymbol{r})+\mathcal{D}_{yy,S_1}(\boldsymbol{r})\mathcal{D}_{xx,S_2}(\boldsymbol{r})-2\mathcal{D}_{xy,S_1}(\boldsymbol{r})\mathcal{D}_{xy,S_2}(\boldsymbol{r})\right\} - \frac{1}{2}\mathcal{D}_{0,S_1}(\boldsymbol{r})\mathcal{D}_{0,S_2}(\boldsymbol{r})\right] - N_2^{\rm s}, \tag{170}$$

$$N_2^{\rm s} = \frac{5}{N_{123}^{\rm T}N}\int d^3\boldsymbol{r}$$
$$\times\left\{\mathcal{E}_{0,S_3}(\boldsymbol{r})\left[\frac{3}{2}\left\{\mathcal{D}'_{xx,S_1}(\boldsymbol{r})\mathcal{E}_{yy,S_2}(\boldsymbol{r})+\mathcal{D}'_{yy,S_1}(\boldsymbol{r})\mathcal{E}_{xx,S_2}(\boldsymbol{r})-2\mathcal{D}'_{xy,S_1}(\boldsymbol{r})\mathcal{E}_{xy,S_2}(\boldsymbol{r})\right\} - \frac{1}{2}\mathcal{D}'_{0,S_1}(\boldsymbol{r})\mathcal{E}_{0,S_2}(\boldsymbol{r})\right]\right.$$
$$\left.+\mathcal{E}_{0,S_3}(\boldsymbol{r})\left[\frac{3}{2}\left\{\mathcal{E}_{xx,S_1}(\boldsymbol{r})\mathcal{D}'_{yy,S_2}(\boldsymbol{r})+\mathcal{E}_{yy,S_1}(\boldsymbol{r})\mathcal{D}'_{xx,S_2}(\boldsymbol{r})-2\mathcal{E}_{xy,S_1}(\boldsymbol{r})\mathcal{D}'_{xy,S_2}(\boldsymbol{r})\right\} - \frac{1}{2}\mathcal{E}_{0,S_1}(\boldsymbol{r})\mathcal{D}'_{0,S_2}(\boldsymbol{r})\right]\right.$$

$$+\mathcal{D}'_{0,S_3}(\boldsymbol{r})\left[\frac{3}{2}\left\{\mathcal{E}_{xx,S_1}(\boldsymbol{r})\mathcal{E}_{yy,S_2}(\boldsymbol{r})+\mathcal{E}_{yy,S_1}(\boldsymbol{r})\mathcal{E}_{xx,S_2}(\boldsymbol{r})-2\mathcal{E}_{xy,S_1}(\boldsymbol{r})\mathcal{E}_{xy,S_2}(\boldsymbol{r})\right\}-\frac{1}{2}\mathcal{E}_{0,S_1}(\boldsymbol{r})\mathcal{E}_{0,S_2}(\boldsymbol{r})\right]\Bigg\}, \tag{171}$$

$$\mathcal{D}_{ab,S_i}(\boldsymbol{r}) \equiv \frac{1}{\sin\theta_{12}}\int_{S_i} d^3\boldsymbol{p}\frac{p_a p_b}{p^2}\tilde{\delta}(\boldsymbol{p})e^{i\boldsymbol{p}\cdot\boldsymbol{r}}, \tag{172}$$

$$\mathcal{D}'_{ab,S_i}(\boldsymbol{r}) \equiv \frac{1}{\sin\theta_{12}}\int_{S_i} d^3\boldsymbol{p}\frac{p_a p_b}{p^2}|\tilde{\delta}(\boldsymbol{p})|^2 e^{i\boldsymbol{p}\cdot\boldsymbol{r}}, \qquad \mathcal{E}_{ab,S_i}(\boldsymbol{r}) \equiv \frac{1}{\sin\theta_{12}}\int_{S_i} d^3\boldsymbol{p}\frac{p_a p_b}{p^2}e^{i\boldsymbol{p}\cdot\boldsymbol{r}}, \tag{173}$$

where p_x and p_y are the x and y components of wave vector $\boldsymbol{p}$, and $N_2^{\rm s}$ is the shot noise of bispectrum quadrupole. In deriving Eq.(170), we have fixed the angle θ_{12} inside the bin. This is an approximation, but is valid as long as the size of the Fourier shell, S_i, is small enough. Thanks to this approximation, we can still apply FFT to $\mathcal{D}_{ab,S_i}(\boldsymbol{r})$, $\mathcal{D}'_{ab,S_i}(\boldsymbol{r})$ and $\mathcal{E}_{ab,S_i}(\boldsymbol{r})$.

We calculate monopole and quadrupole of bispectrum using these estimators as follows. 1) We assign the particles or halos to a cartesian grid of dimension $N_{\rm grid} = 512^3$ using Cloud in Cell (CIC) interpolation. 2) Applying FFT for the density field on grids, we obtain the density field in Fourier space. 3) Applying inverse FFT, we calculate $\mathcal{D}$ and $\mathcal{E}$ in Eqs.(167),(168),(172) and (173) (we omit the subscripts in $\mathcal{D}$ and $\mathcal{E}$) on grids from the density field in Fourier space. 4) Taking summation over the product of $\mathcal{D}$ and $\mathcal{E}$, we obtain Eqs.(164)-(166),(170) and (171). The difference between the fast measurement method and he naive estimator in Eq.(161) appears from process 3). To calculate the bispectrum from the density field in Fourier space, naive estimator have to check $N_{\rm grid}^2$ cells for the triangle condition, $\delta_{\rm D}(\boldsymbol{p}_1+\boldsymbol{p}_2+\boldsymbol{p}_3)$, while the fast measurement method only needs $N_{\rm grid}\log N_{\rm grid}$ operations for FFT. Therefore, the fast measurement method is quite powerful compare to the naive estimator [76]. This fast measurement method takes less than two hour to calculate monopole and quadrupole of bispectrum in the case of data set 3 for halo catalog which we will describe below (see Table 8). Here, we used the 64 nodes for parallel computation with OpenMP to perform FFT.

5.2 Fast calculation for improved bispectrum template

Toward a practical data analysis using bispectrum, fast computational method is demanding not only for the measurement of bispectrum but also for the calculation of bispectrum template. The improved model of bispectrum developed in Chap.4 needs five-dimensional integration and computational cost becomes high if we proceed to the parameter estimation analysis using all configurations of bispectrum, which we will later demonstrate. A

straightforward way to accelerate the calculation is to store the numerical data of the template for various configurations over the parameter space, and interpolate these results to obtain the template to be fitted to the measured bispectrum. In this section, we summarize the method to quickly construct the template of our improved bispectrum model.

In this thesis, we are particularly interested in constraining the growth rate, f, from bispectrum, marginalizing over other nuisance parameters which keep the systematics under control. The systematics we need to take care are the Finger-or-God effect and galaxy/halo bias for which we will assume linear bias (but we allow it to be scale dependent, see Chap.5.6.1). Then, the number of free parameters for each configuration of bispectrum is three, i.e., f, $\sigma_{\rm v}$, and b. In this case, our improved model Eq.(151) can be expanded in polynomial form of f and b except FoG damping term:

$$B^{(\rm s)}_{\rm model}(\boldsymbol{k}_1,\boldsymbol{k}_2,\boldsymbol{k}_3) = D_{\rm FoG}(k_1\mu_1,k_2\mu_2,k_3\mu_3,f\sigma_v) \times\Big\{\sum_{i_1=0}^{1}\sum_{i_2=0}^{1}\sum_{i_3=0}^{1}\sum_{j=0}^{6} b^{i_1}(k_1)b^{i_2}(k_2)b^{i_3}(k_3)f^j B_{i_1i_2i_3j}(\boldsymbol{k}_1,\boldsymbol{k}_2,\boldsymbol{k}_3)\Big\}, \tag{174}$$

with, $i_1+i_2+i_3+j\le 6$. The expression given above is valid at one-loop order, and number of possible non-vanishing components in $B_{i_1i_2i_3j}$ becomes 32. This expression can be also applied to the tree bispectrum model, and in this case, $i_1+i_2+i_3+j\le 4$ and $B_{i_1i_2i_3j}$ has 16 components. Hence, once we obtain $B_{i_1i_2i_3j}(\boldsymbol{k}_1,\boldsymbol{k}_2,\boldsymbol{k}_3)$, we can quickly construct the template the perturbative part for any values of f and b. To construct the template for bispectrum multipoles, we need to further perform the angular integral for $B_{i_1i_2i_3j}$ multiplied by the FoG factor:

$$B_{i_1i_2i_3j,\ell}(k_1,k_2,\theta_{12}) = \int_0^{2\pi}\frac{d\phi}{2\pi}\int_0^1 d\mu D_{\rm FoG}(k_1\mu_1,k_2\mu_2,k_3\mu_3,f\sigma_v)B_{i_1i_2i_3j}(\boldsymbol{k}_1,\boldsymbol{k}_2,\boldsymbol{k}_3)\mathcal{P}_\ell(\mu). \tag{175}$$

In the analysis below, we first store the numerical data of Eq.(175) for various configurations and values of σ_v. Interpolating these data set, the bispectrum template is then constructed according to Eq.(174).

5.3 Constructing mock catalogs from N-body simulations

To test our bispectrum template, we create matter and halo catalog from N-body simulation with cosmological parameters shown in Table 5.3. We use publicly available code, Gadget2, and the initial conditions were generated with 2LPT. The main characteristics of the

simulation are summarized in Table 7. We first created the 380 realizations of matter fields with 1024^3 particles in a cosmological volume of $(1.0\ h^{-1}\mathrm{Gpc})^3$. The total effective volume is 380 $(h^{-1}\mathrm{Gpc})^3$ and the mass resolution is $2.58 \times 10^{11}\ h^{-1}\mathrm{M}_\odot$.

Then, we construct the halo fields from 350 simulations with the Friends-of-frends (FoF) group finder [78] and the Rockstar code [79]. In the FoF algorithm, the particles are linked together when their distance is shorter than linking length. In this thesis, we set the linking length to 0.2 times of mean separation of particles, and consider the groups linked more than 20 particles as candidates of halo. These candidates of halo still have particles which is not bounded for the gravity of halo, and some of neighbor halos are recognized as one halo, because FoF algorithm only cares the positions of particles. The Rockstar code analyzes each candidate of halo in phase space, then removes the unbounded particles and classifies the neighbor halos [79].

The FFT grid used for statistical calculation is 512^3 elements. The corresponding Nyquist frequency is 1.61 h Mpc^{-1}. While we neglect shot noise corrections in matter fields, we take into account the shot noise corrections for halo power spectrum and bispectrum. Since we are interested in the scales much larger than Nyquist frequency, we do not consider the aliasing corrections in both cases. In the simulations presented below, we did not apply the method to reduce the fluctuation of the initial density fields, described in Eq.(154).

Setting the size of the Fourier bin to the fundamental Fourier mode, i.e., $\Delta k = 2\pi/L$, we measure the bispectra using the fast estimator described in Chap. 5.1. Because of finite size of bins, various wave vectors $\vec{k}_i$ fall into the same bin. Due to the finite numbers of discrete Fourier modes, the averaged wavenumber over each bin is not always equal to the central value of the bin. To take account of this, we estimate the actual mean value of wavenumber in each Fourier bin, which is used to compute theoretical template of power spectrum and bispectrum. For the power spectrum, we also consider the effect of inhomogeneous sampling arising from discrete Fourier modes, and take the average over the discrete Fourier-modes (see Appendix B of Ref. [26] in detail).

5.4 Likelihood Analysis

To get the best-fit values and statistical errors of the free parameters, we perform maximum likelihood analysis based on the Markov-chain Monte Carlo technique (MCMC) using publicly available python code, emcee [80, 81]. We assume Gaussian likelihood function for

parameters	
H_0	72
Ω_Λ	$1 - \Omega_\mathrm{m}$
Ω_m	0.301
σ_8	0.801
n_s	0.963

Table 6: Cosmological parameters using for Gadget-2 simulation.

	Matter fields	Halo fields
Number of realizations	380	350
Box size [h^{-1}Mpc]	1000.	1000.
Number of particles	1024^3	1024^3
Particle/Halo mass [$h^{-1}\mathrm{M}_\odot$]	2.58×10^{11}	$> 5.16 \times 10^{12}$
Initial redshift (z_ini)	15	15
Output redshifts	$z = 1,\ 0.5$	$z = 1,\ 0.5$

Table 7: Parameters of N-body simulation data sets used in the Gadget-2 code.

power spectrum and bispectrum:

$$\mathcal{L}_P \propto \exp\left\{-\frac{1}{2}\chi_P^2\right\}; \quad \chi_P^2 \equiv \sum_{\ell,\ell'=1,2}\sum_{ij}\left(P^{(s)}_{i,\ell,\mathrm{model}} - P^{(s)}_{i,\ell,\mathrm{sim}}\right)\left(C^P_{\ell\ell'}\right)^{-1}_{ij}\left(P^{(s)}_{j,\ell,\mathrm{model}} - P^{(s)}_{j,\ell,\mathrm{sim}}\right), \tag{176}$$

$$\mathcal{L}_B \propto \exp\left\{-\frac{1}{2}\chi_B^2\right\}; \quad \chi_B^2 \equiv \sum_{\ell,\ell'=1,2}\sum_{ij}\left(B^{(s)}_{i,\ell,\mathrm{model}} - B^{(s)}_{i,\ell,\mathrm{sim}}\right)\left(C^B_{\ell\ell'}\right)^{-1}_{ij}\left(B^{(s)}_{j,\ell,\mathrm{model}} - B^{(s)}_{j,\ell,\mathrm{sim}}\right). \tag{177}$$

Here, i and j represent the Fourier bin. The functions $P^{(s)}_{i,\ell,\mathrm{model}}$ and $B^{(s)}_{i,\ell,\mathrm{model}}$ are respectively the theoretical templates of multipole power spectrum and bispectrum given at the wavenumber of i-th Fourier bin or the i-th triangular configuration (actual meaning of the index i for the bispectrum will be later described in Chap. 5.5). For $P^{(s)}_{i,\ell,\mathrm{model}}$, we use the TNS model in Ref. [11]. The derivation of the TNS model and its analytical expressions are summarized in Appendix C. For $B^{(s)}_{i,\ell,\mathrm{sim}}$, we adapt our improved model in Eq.(148) with Gaussian damping function (Eq.(157)), but for references, the models ignoring the one-loop corrections (tree PT model), and including the D_1 and D_2 terms (SPT one-loop model, see

	0	1	2	3
Statistical quantity	Power spectrum	Bispectrum		
$k_{\rm min}$	k_f	k_f		0.05
$k_{\rm max}$	0.15	$k_3 < 0.05$, k_1 and $k_2 < 0.15$		0.15
Configurations		$\cos\theta_{23} < 0.0$	$0.0 \leq \cos\theta_{23}$	
Number of bins	29	204	384	766

Table 8: Summary of data sets for power spectrum and bispectrum used in likelihood analysis. Here, $\cos\theta_{23} \equiv \hat{\boldsymbol{k}}_2 \cdot \hat{\boldsymbol{k}}_3$.

Eqs.(149), (150) and Appendix A) with Gaussian damping function are also examined to see the impact of correction terms. The $P^{(s)}_{i,\ell,\rm sim}$ and $B^{(s)}_{i,\ell,\rm sim}$ are the averaged power spectrum and bispectrum over 300 realizations of N-body simulations given at i-th Fourier bin or i-th triangular configuration. The $C^P_{\ell\ell',ij}$ and $C^B_{\ell\ell',ij}$ in Eqs.(176) and (177) are the covariance matrices of the ℓ- and ℓ'-th moment of multipole power spectrum and bispectrum between i-th and j-th bins. In this thesis, we consider only the diagonal components, ignoring the non-Gaussian off-diagonal components. Thus, the covariances can be written as

$$C^P_{\ell\ell',ij} \equiv \delta_{\ell\ell'}\delta_{ij}\left(\sigma^P_i\right)^2, \tag{178}$$

$$C^B_{\ell\ell',ij} \equiv \delta_{\ell\ell'}\delta_{ij}\left(\sigma^B_i\right)^2. \tag{179}$$

Here, σ^P_i and σ^B_i is the statistical errors of power spectrum and bispectrum at i-th bin or i-th triangle, which are evaluated from the standard error of simulations according to Eq.(156). Then, the maximum likelihood estimation gives the best fit values of parameters. Also, with the MCMC chain of the samples, one can evaluate the posterior probability distribution for each parameter from which we can estimate the statistical uncertainty of the best-fit values. When combining both power spectrum and bispectrum, we assume that power spectrum and bispectrum are statistically uncorrelated, and use $\mathcal{L}_P \times \mathcal{L}_B$ as the total likelihood function to estimate the best-fit value and statistical uncertainties of the model parameters.

Below, the likelihood analysis is performed with various values of $k_{\rm max}$ up to $0.15\,h$ Mpc^{-1}. In particular, for the bispectrum, robustness of the best-fit results are carefully checked with different combination of data set. Table 8 summarizes the data used for likelihood analysis.

5.5 Results in matter fields

Let us first present the results for matter density fields to check if our improved bispectrum model can consistently reproduce the fiducial model parameters, as well as to see the impact of combining both power spectrum and bispectrum to break the degeneracy of the parameters between f and $\sigma_v' \equiv f\sigma_v$.

To demonstrate this, we assume a hypothetical survey with the volume $1\,h^{-3}\,\mathrm{Gpc}^3$ at $z = 1$. This is comparable to that of a particular redshift slice of Subaru PFS [82]. To estimate the statistical errors, we simply rescale the (diagonal component of) covariance evaluated from 380 simulations by

$$C^P_{\ell\ell',ii} \to \frac{V_{\rm sim}}{V_{\rm surv}} C^P_{\ell\ell',ii}, \tag{180}$$

$$C^B_{\ell\ell',ii} \to \frac{V_{\rm sim}}{V_{\rm surv}} C^B_{\ell\ell',ii}. \tag{181}$$

Here, $V_{\rm sim}$ is the total volume of simulation over 380 realization while $V_{\rm surv}$ is survey volume of hypothetical survey, i.e., $V_{\rm surv} = 1h^{-3}\mathrm{Gpc}^3$. Fig. 21 and Table 9 present the results of the parameter estimation. In Fig. 21, the 68% (and 96%) confidence regions of power spectrum and bispectrum are respectively depicted as darker (lighter) gray and green contours. There is a strong degeneracy between parameters f and σ_v' in each case. However, the degeneracies shown in power spectrum and bispectrum cases are slightly different each other, and combining power spectrum and bispectrum helps to break the degeneracy, reducing the statistical error significantly, as shown by the red contour in Fig. 21. As a result, the marginalized 1 σ error (68% C.L.) on f becomes tighter than 30%, and fiducial value of f is inside the confidence region (Table 8). Increasing $k_{\rm max}$, available number of Fourier modes gets increased, and the statistical error would be further reduced, leading to a much tighter constraint. However, the present theoretical templates are built with one-loop PT calculations, and beyond $k_{\rm max} = 0.15\,h\,\mathrm{Mpc}^{-1}$, nonlinear effect of gravity becomes significant, and the higher-order corrections need to be included.

The resultant constraint shown in Fig. 21 indicates that the PT-based template works very well, but comparing the best-fit results of the PT templates with the measured results from simulations, as shown in Figs. 22-24, we sometimes see a large discrepancy especially for bispectrum in several types of configurations. Here, in Figs. 23 and 24, the results are sorted as triangle configurations indexed with Fourier bins similar to Ref. [62]. The index starts from the smallest triangle among the data set. We then plot the bispectrum for

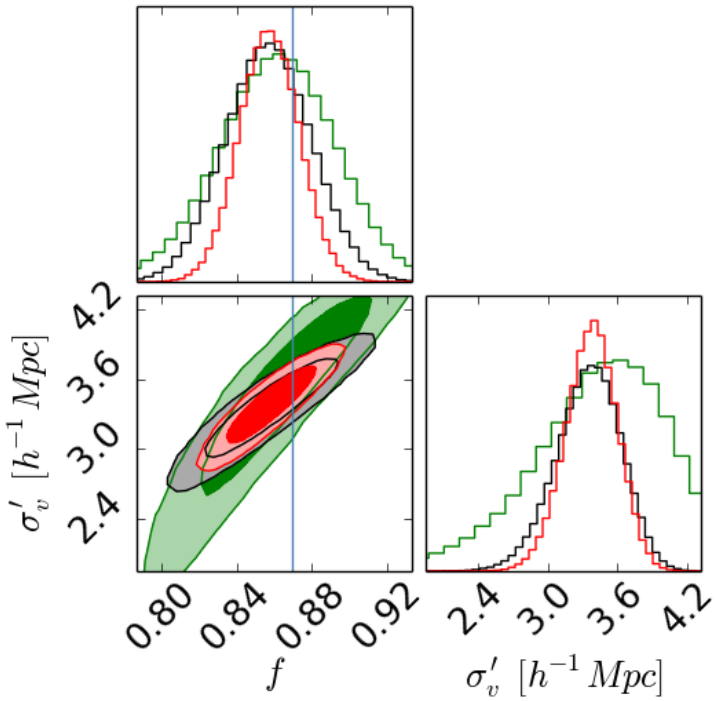

Figure 21: Constraints on the parameters f and σ_v' from the matter field, assuming a hypothetical survey with the volume $1\,h^{-3}\,\mathrm{Gpc}^3$ at $z = 1$. The darker (lighter) green, black and red contours show the statistical uncertainty at 68% (95%) confident limit from the bispectrum, power spectrum, and combination of both power spectrum and bispectrum, respectively. Blue vertical lines indicate the fiducial value of f.

	$P^{(s)}_{\mathrm{model}}$: 1-loop	$B^{(s)}_{\mathrm{model}}$: 1-loop	$P^{(s)}_{\mathrm{model}} + B^{(s)}_{\mathrm{model}}$: 1-loop	fiducial/linear
f	$0.8582^{+0.0097}_{-0.0105}$	$0.8619^{+0.0135}_{-0.0138}$	$0.8582^{+0.0068}_{-0.0073}$	0.8698
σ_v'	$3.380^{+0.114}_{-0.128}$	$3.493^{+0.247}_{-0.266}$	$3.392^{+0.091}_{-0.101}$	3.164

Table 9: The best-fit values and the marginalized 1 σ error of the parameters f and σ_v' from redshift-space power spectrum, bispectrum and combination of power spectrum and bispectrum in matter fields assuming a hypothetical survey with the volume $1\,h^{-3}\,\mathrm{Gpc}^3$ at $z = 1$. The results are obtained from the maximum likelihood analysis with MCMC technique up to $k_{\mathrm{max}} = 0.15\,h\mathrm{Mpc}^{-1}$.

triangular bins where we sequentially loop through all possible sets of values of k_1, k_2 and k_3, with k_3 in the inner most loop, and k_1 in the outer most increasing loop, where the loops go from k_f to the maximum value considered, either $k_{max} = 0.15h\text{Mpc}^{-1}$, a truncation scale set by our constraints $k_3 \leq k_2 \leq k_1$ or $k_1 \leq k_2 + k_3$. In this method, a smaller index tends to represent the bispectrum at larger scale.

In Figs. 23 and 24, while the best-fit power spectrum template perfectly matches the measured power spectrum quite well, a large discrepancy is found for squeezed and flattened-shape triangles in the quadrupole moments of bispectrum, and it is true even at large scales. A possible reason for this may be that due to a finite number of Fourier modes, discreteness of Fourier modes leads to an inhomogeneous sampling over each bin. As a result, the measured bispectrum averaged over each Fourier bin may differ from the PT template computed at the center of Fourier bin. Our bispectrum templates were built accounting for the weighted sampling, and each bispectrum was computed at the weighted Fourier modes, however, the effect of inhomogeneous sampling has not been properly taken into account in this treatment. Note that in computing the power spectrum, we partly include it by averaging over the discrete Fourier modes over each bin according to Ref. [26] (In Fig. 22, the zigzag pattern seen in the quadrupole power spectrum indeed comes from the effect of inhomogeneous sampling). Another important source for the discrepancy may come from our measurement of bispectrum from N-body simulations. Indeed, in measuring bispectrum for each configuration, we assume that the angle θ_{12} (see Fig. 9 for definition) is fixed over each Fourier bin, but this would be a crude approximation especially at large scales (low-k modes). To see the impact of these systematics, the data set 2 is useful, because the triangles in this data set is chosen as $0.0 \leq \cos\theta_{23} (\equiv \hat{\boldsymbol{k}}_2 \cdot \hat{\boldsymbol{k}}_3)$ and $k_3 < 0.05h^{-1}\text{Mpc}$. In Fig. 23, we see the discrepancy between measurement and the best-fit template including other data sets.

Finally, we compare the parameter estimation results of our improved model with other PT models. Fig. 25 shows the k_{max} dependance of the best fit values, the statistical uncertainty at 68% confidence levels of fitting parameters, and, χ^2_{red}, from maximum likelihood analysis and MCMC with TNS model of power spectrum, tree, SPT one-loop and our improved model of bispectrum, and these results at $k_{max} = 0.15h^{-1}\text{Mpc}$ is summarized in Table 10. Here, the χ^2_{red} is calculated dividing the chi-square in the exponent in Eqs.(176) and (177) by the degrees of freedom. To reduce the systematics mentioned above, we only use the triangles satisfying the conditions, $k_{2min} + k_{3min} > k_{1max}$, where k_{imin} (k_{imax}) is the

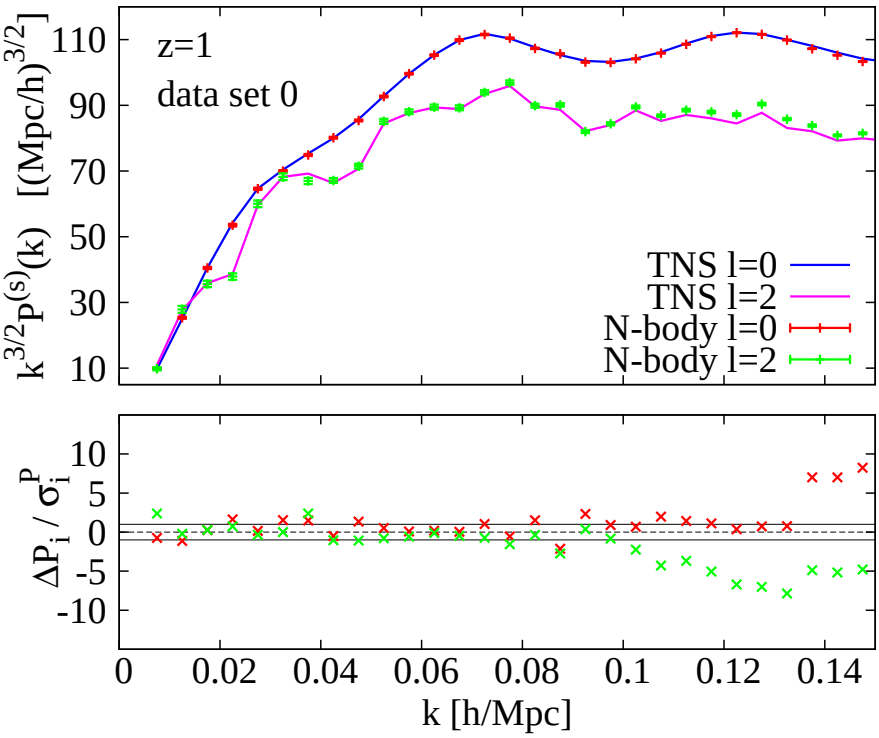

Figure 22: Redshift-space power spectrum multiplied by $k^{3/2}$ for matter fields (top) and fractional difference between the best-fit theoretical model and measured result from simulations, normalized by the standard error, $(P^{(\mathrm{s})}_{\ell,\mathrm{sim}} - P^{(\mathrm{s})}_{\ell,\mathrm{model}})/\sigma^P$, (bottom). The results are then plotted as function of wave number k at $z = 1$. In top panel, red (green) points with error bars and blue (magenta) line indicate the results of power spectrum monopole (quadrupole) from simulations and TNS model, respectively. The red (green) points in bottom panel are the fractional error of power spectrum monopole (quadrupole). In plotting the predictions, the best-fit values of the parameters, f and σ'_v, obtained from the maximum likelihood analysis with $k_{\mathrm{max}} = 0.15\,h\,\mathrm{Mpc}^{-1}$ are used.

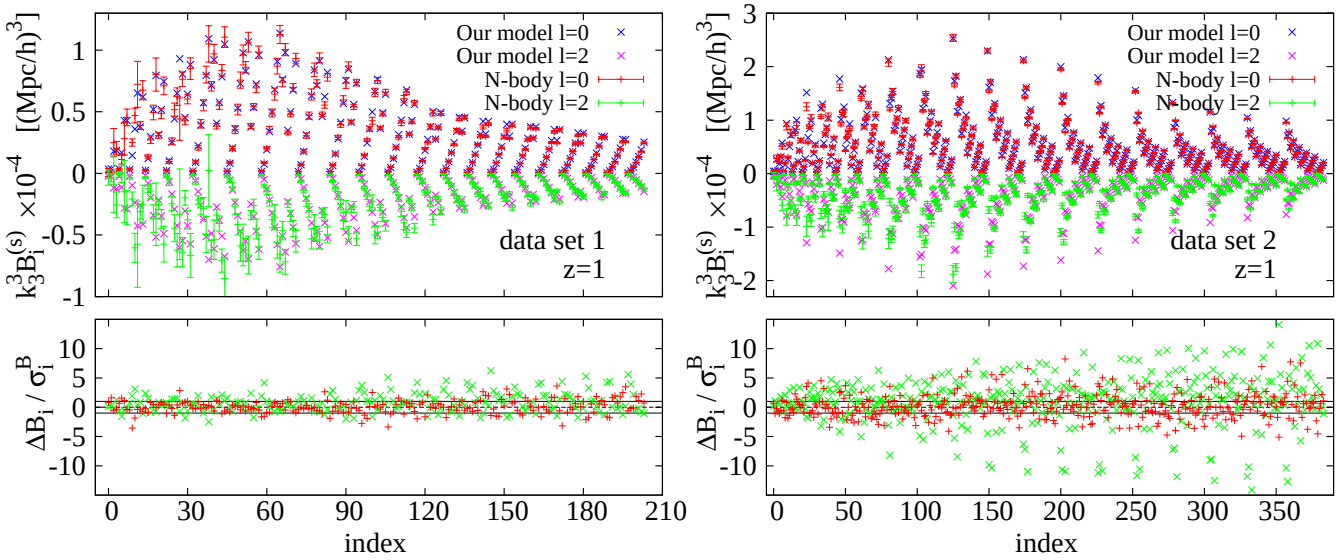

Figure 23: Redshift-space bispectrum multiplied by k_3^3 in matter fields (top) and its fractional difference between the theoretical model and simulation result normalized by statistical error of simulation , $(B^{(s)}_{\ell,\mathrm{sim}} - B^{(s)}_{\ell,\mathrm{model}})/\sigma^B$, (bottom), plotted as function of triangle index of data set 1 (left) and 2 (right) at $z = 1$. The horizontal axis means the index of triangles, and $B_i^{(s)}$ is the bispectrum corresponding to the bin which has ith index. In top panel, red (green) points with error bars and blue (magenta) line indicate the results of bispectrum monopole (quadrupole) from simulations and our theoretical model, respectively. The red (green) points in bottom panel are the fractional error of bispectrum monopole (quadrupole). In plotting the predictions, the best-fit values of the parameters f and σ_v' obtained from the maximum likelihood analysis with $k_{\mathrm{max}} = 0.15\,h\,\mathrm{Mpc}^{-1}$ are used.

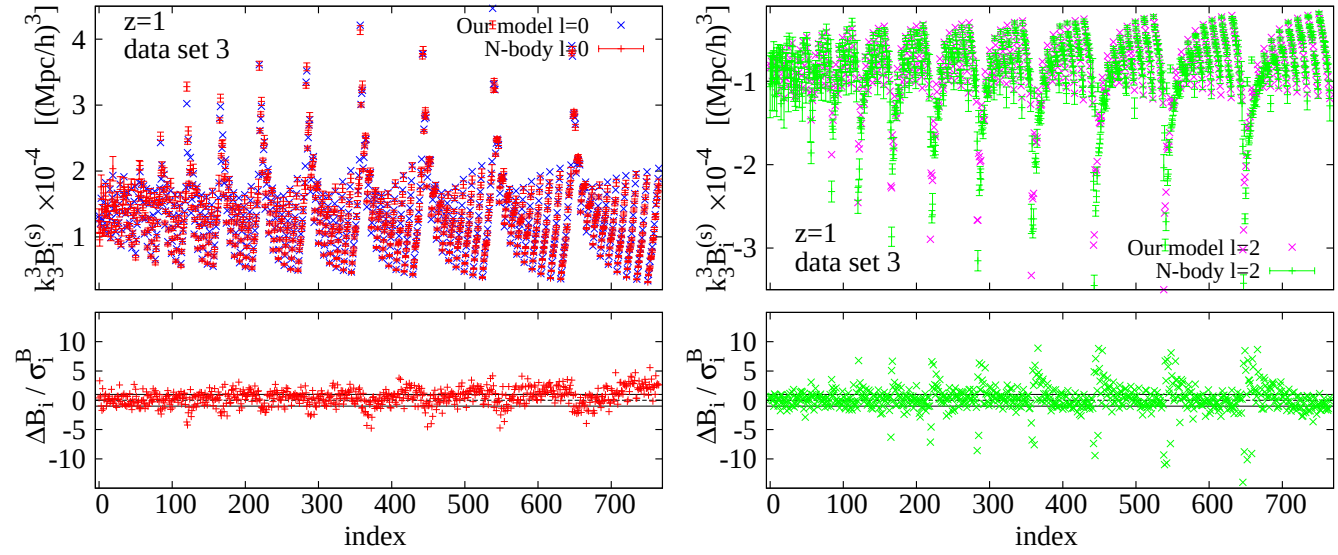

Figure 24: Same as Fig.23, but here we show the results of data set 3. Left and right panels show the results of monopole and quadrupole of bispectrum, respectively.

	$P^{(s)}_{\rm model}$: 1-loop	$B^{(s)}_{\rm model}$: 1-loop	$B^{(s)}_{\rm model}$: SPT,1-loop	$B^{(s)}_{\rm model}$: tree	fiducial/linear
f	$0.8582^{+0.0005}_{-0.0005}$	$0.8984^{+0.0011}_{-0.0011}$	$0.9184^{+0.0014}_{-0.0013}$	$0.7560^{+0.0009}_{-0.0005}$	0.8698
σ'_v	$3.380^{+0.006}_{-0.006}$	$4.171^{+0.014}_{-0.014}$	$4.761^{+0.016}_{-0.015}$	$0.186^{+0.001}_{-0.000}$	3.164

Table 10: The best-fit values and the marginalized 1 σ errors of the parameters f and σ'_v from redshift-space power spectrum and bispectrum in matter fields at $z = 1$. The results are obtained from the maximum likelihood analysis with MCMC technique up to $k_{\rm max} = 0.15\ h{\rm Mpc}^{-1}$. In this analysis, the bispectra which do not satisfy the conditions, $k_{2,\rm min} + k_{3,\rm min} > k_{1,\rm max}$ and $\cos\theta_{12} > -0.9$ are removed.

minimum (maximum) wavelength of the bin k_i, and $\cos\theta_{12} > -0.9$. Here, we do not assume any survey condition, and just check the accuracy of estimation. That is the covariance matrices of power spectrum and bispectrum are just those evaluated over 380 simulations (i.e., $V_{\rm sim}/V_{\rm surv} = 1$ in Eqs.(180) and (181)).

Due to a large number of realization data, we can get the best fit values with sufficiently small uncertainty, with which we can address the accuracy of theoretical template by few percent level. From the Fig. 25 and Table 10, we see that the TNS model can reproduce the fiducial value of growth rate f within 3% accuracy in any $k_{\rm max}$, and $\sigma'_v = f\sigma_v$ is almost consistent with linear theory prediction. For references, Fig. 25 and Table 10 also show the results based on the tree-level PT and SPT one-loop models. As increasing $k_{\rm max}$, the best-fit value of f obtained from the tree PT model starts to deviate from fiducial one by more than 10%. One the other hand, SPT one-loop model reasonably reproduces the fiducial value of f within almost 3% accuracy. This demonstrates that one-loop contribution to the redshift-space bispectrum is quite important to estimates the cosmological parameters correctly. A closer look at the estimated f, however, reveals a small but non-negligible systematic offset from the fiducial value. In both cases, the resultant values of $\chi^2_{\rm red}$ are larger than that of our improved model. We thus conclude that our improved model of bispectrum is the best among the three PT models, and gives a consistent result with the likelihood analysis using power spectrum.

5.6 Results in halo fields

Let us next consider the halo catalogs. The dark matter halo is the self-gravitating bound object composed of dark matter. After halo is formed, the mass of halo continuously grows

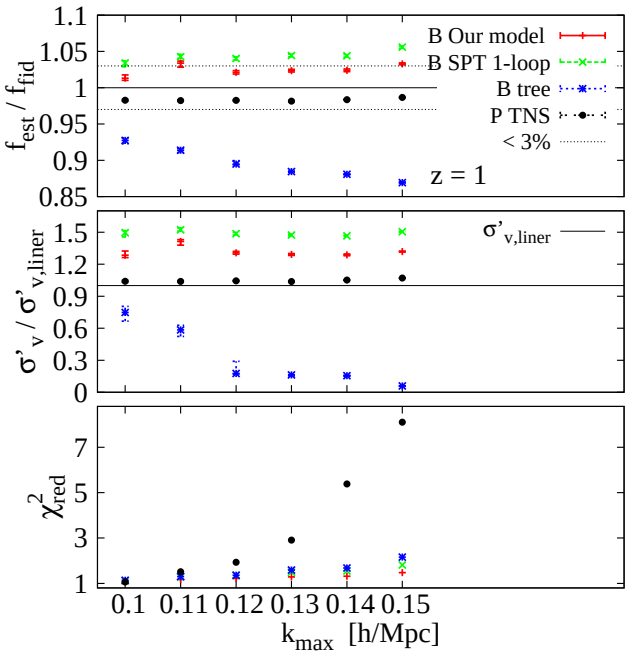

Figure 25: Best-fit value with 1 σ error of the parameters f (top) and σ'_v (middle), and the reduced chi-square (bottom), plotted against maximum wavenumber $k_{\rm max}$ at $z = 1$. Red, green and black symbols respectively represent the results from the bispectrum from the SPT one-loop, our improved model and tree calculation removing the bispectra which do not satisfy the conditions, $k_{2,\rm min} + k_{3,\rm min} > k_{1,\rm max}$ and $\cos\theta_{12} > -0.9$. On the other hand, black symbols are obtained from the power spectrum based on TNS model by Ref. [11].

through the accretion and merger processes. Baryonic material will be therefore dragged gravitationally by the dark matter halo, and baryons will concentrate towards its deep potential well. The halos are thus regarded as the sites of galaxy formation, and in this respect, the statistics of halo distribution are expected to be close to those of the observed galaxy distribution. Hence, the test against halo catalogs is an important next step toward practical application.

One important difference between halo and dark matter catalogs is that the halo distribution is not a perfect tracer of dark matter distribution, and we need to incorporate the effect of clustering bias into the theoretical template. This is rather essential for our case with PT-based template for the dark matter distribution.

5.6.1 Linear bias model

Here, we discuss a simple recipe to incorporate the effect of clustering bias into our PT-based template. The clustering bias for halos, in comparison with dark matter distribution, is basically described by the so-called extended Press-Schechter formalism that is constructed based on the assumption of peak-background split [83]. With this treatment, the fluctuation of number density of halos, $\delta_{\rm h}$, is generally expressed as a nonlinear function of dark matter density field $\delta_{\rm m}$ (e.g.,Refs. [84, 85]). However, the nonlinearity of halo bias partly comes from gravitational evolution, and for our interest of large scales, the nonlinearity is supposed to be weak. In this respect, the assumption of linear bias may be validated. In what follows, adopting the same approach by Ref. [86] as examined in the power spectrum, we assume the linear but scale-dependent bias in the form:

$$\delta_{\rm h}(\boldsymbol{k}) = b(\boldsymbol{k})\delta_{\rm m}(\boldsymbol{k}). \tag{182}$$

Here, b is the linear bias parameter, in the absence of primordial non-Gaussianity, it is expected to be constant on large scales [87]. It is shown in Refs. [86, 13] that the halo power spectrum is well described by the linear bias Eq.(182) on top of the following scale-dependent function:

$$b^2(k) = b_0^2 \frac{1 + Qk^2}{1 + Ak}, \tag{183}$$

where, b_0, Q and A are regarded as nuisance parameters to be determined by fitting the template to the measured data.

The scale dependent function in Eq.(183) is known to empirically work well in weakly non-linear regime, and has been used for the data analysis in 2dF Galaxy Redshift Survey

[88] and SDSS-II DR7 LRG catalog [13]. Also, Ref. [89] shows that combining TNS model with the linear bias with Eq.(183), the growth rate can be estimated in a good accuracy from the halo catalog.

5.6.2 Results

Similarly to the matter field case, let us first examine the analysis assuming the hypothetical survey of the volume $1\,h^{-3}\,\mathrm{Gpc}^3$ at $z = 1$. Incorporating the bias prescription in Chap. 5.6.1 into PT-based template, we check if the growth rate f is estimated correctly from the halo power spectrum and bispectrum. Note that in this study, we have in total five parameters to be determined, i.e., f, $\sigma_{\rm v}' = f\sigma_{\rm v}$, b_0, A and Q. The result of likelihood analysis is shown in Fig. 26 and Table 11. Note that the statistical error are estimated based on the covariance matrices given at Eqs.(180) and (181) with $V_{\rm sim}/V_{\rm surv} = 350/1$. We here use all the data set shown in Table 8. Similar to the matter field case, there is a strong degeneracy between f and σ_v'. Combining bispectrum helps to partly break the degeneracy, tightening the constraint on f, as we saw in previous section. Quantitatively, the statistical uncertainty at 68% confidence limit of f is reduced by more than 30% if we combinin the bispectrum. Still, the fiducial value of f is estimated correctly within the confidence region.

However, as summarized in Table 11, the best-fit value of the growth rate from the bispectrum data rather differs from the one from the power spectrum data, and largely deviates from the fiducial value. In Figs. 27, 28 and 29, the best-fit power spectrum and bispectrum templates are compared with measured results from halo catalogs, showing a large discrepancy in the squeezed and flattened-shape triangles for the bispectrum. As we have already seen in the matter field case, this would be probably due to the effect of inhomogeneous sampling in both measurement and theoretical template. A great difference is that this effect does not affect the parameter estimation in matter field case, but now in the halo case, it leads to a biased estimation of f. One possible reason may be that the incomplete prescription for halo bias leads to a spurious parameter degeneracy between growth rate and bias parameters, which results in a biased estimation.

In order to reduce the impact of this flaw, one simple approach is to remove the squeezed and flattened-shape bispectra from the parameter estimation analysis. Fig. 30 and Table 12 presents the results removing the bispectra which do not satisfy the conditions, $k_{2,\rm min} + k_{3,\rm min} > k_{1,\rm max}$ and $\cos\theta_{12} > -0.9$. Fig. 30 summarizes the best-fit values of f and marginalized 1σ errors, plotted as function of $k_{\rm max}$. Here, to estimate the statistical error,

we simply adopt the covariance evaluated from the 350 realizations of halo catalogs (that is, Eqs.(180) and (181) with $V_{\rm sim}/V_{\rm surv} = 1$).

Then, with the improved one-loop templates (black and red), the resultant best-fit values of the growth rate and other parameters, obtained from power spectrum and bispectrum, become almost consistent with each other. As a result, the fiducial value is recovered well within the 3% accuracy. The $\chi^2_{\rm red}$ is also reasonably small even at $k_{\rm max} = 0.15\,h\,{\rm Mpc}^{-1}$. On the other hand, bispectrum templates based on the tree-level PT and naive one-loop SPT yield biased estimation of f, inconsistent with the best-fit values obtained from the power spectrum data.

Having confirmed that removing the squeezed and flattened-shape configurations reduces systematics, we go back to the combined analysis of both power spectrum and bispectrum, and finally demonstrate how well we can properly estimate and constrain the growth rate with the limited number of triangles for bispectrum. Fig. 31 and Table 13 present the results, again assuming the hypothetical survey with the volume of $1\,h^{-3}\,{\rm Gpc}^3$ at $z = 1$. Removing the squeezed and flattened- shape triangles, the statistical power of bispectrum data is rather suppressed, and the improvement of the constraint on f is limited to 17% at most, although the best-fit value properly reproduces the fiducial one. The result clearly illustrates the importance of including all the configurations of the bispectrum to tightly constrain f. Thus, making the best use of the potential power of the bispectrum, halo bias prescription needs to be improved, together with a proper account of the effect of inhomogeneous sampling. Still, however, the improvement of the constraint on f is rather comparable to the result by Ref. [62], in which they combined the power spectrum with bispectrum monopole only, and used the data at $z = 0.57$ up to higher $k_{\rm max}$ ($\simeq 0.2\,h\,{\rm Mpc}^{-1}$). Despite the fact that the number of triangles used in the parameter estimation is reduced by $\sim 40\%$, the results in Fig. 31 and Table 13 are regarded as a considerable success, and it proves that including bispectrum quadrupole indeed plays an important role to tighten the constraint on f. We thus conclude that the data analysis including the anisotropic bispectrum data is crucial for future galaxy surveys, and the analysis and methods developed in this chapter, including the fast estimation of bispectrum and the accelerated calculation of PT-based template, are valuable and helpful.

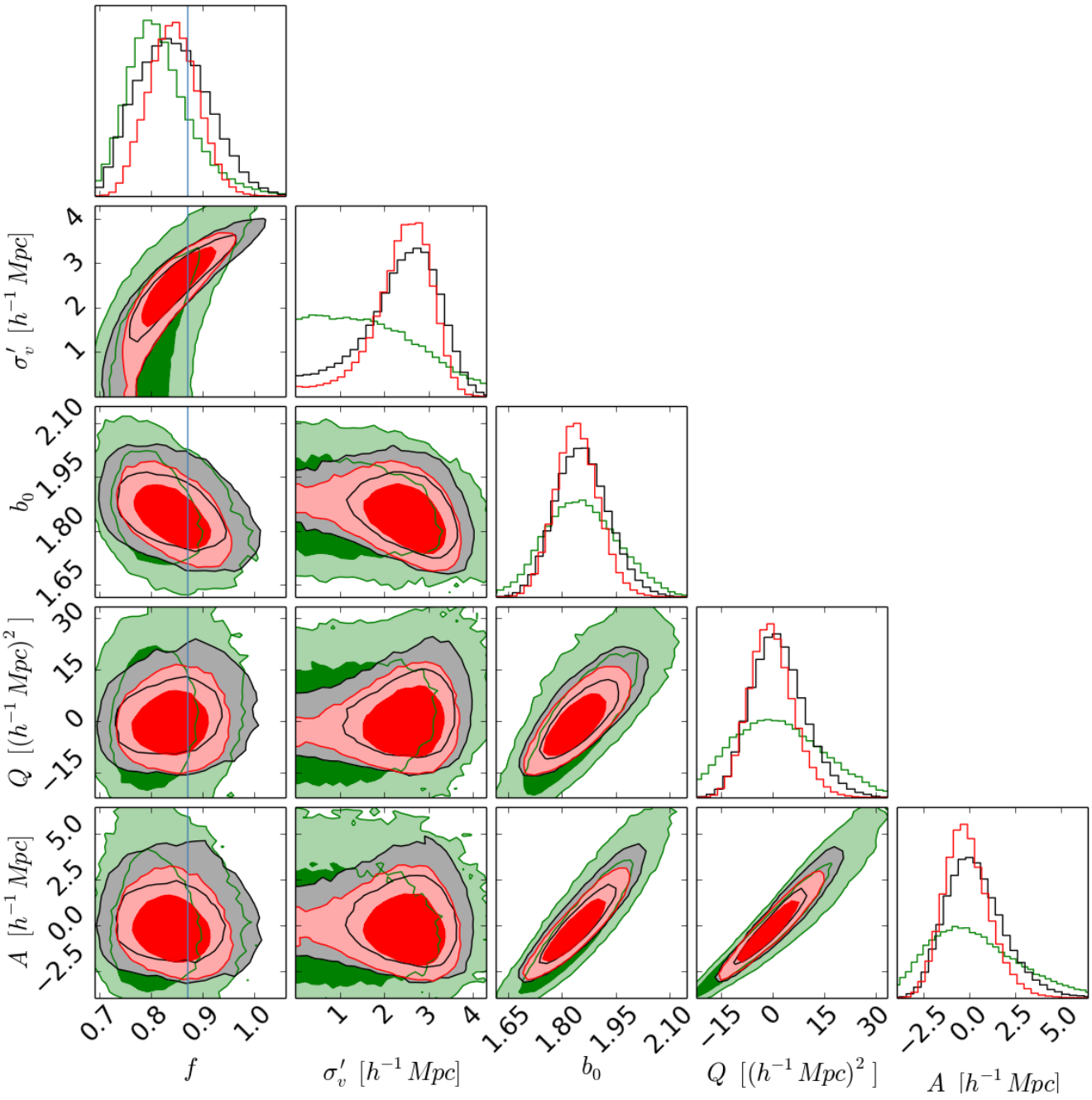

Figure 26: Constraint on the parameters f, σ_v', b_0, Q and A from the halo catalog, assuming a hypothetical survey with the volume 1 h^{-3} Gpc^3 at $z = 1$. The darker (lighter) green, black and red contour respectively shows the statistical uncertainty at 68% (95%) confident limit from bispectrum, power spectrum, and combination of them based on the improved PT templates. Blue vertical lines indicate the fiducial value of f.

	$P^{(s)}_{\rm model}$: 1-loop	$B^{(s)}_{\rm model}$: 1-loop	$P^{(s)}_{\rm model}$ + $B^{(s)}_{\rm model}$: 1-loop	fiducial/linear
f	$0.8568^{+0.0280}_{-0.0367}$	$0.7769^{+0.0352}_{-0.0155}$	$0.8590^{+0.0171}_{-0.0263}$	0.8698
σ'_v	$2.671^{+0.271}_{-0.425}$	$0.2833^{+0.9908}_{-0.0965}$	$2.712^{+0.180}_{-0.336}$	3.164
b_0	$1.817^{+0.045}_{-0.022}$	$1.822^{+0.054}_{-0.036}$	$1.815^{+0.034}_{-0.019}$	
Q	$-2.054^{+4.453}_{-2.487}$	$-8.546^{+9.304}_{-3.512}$	$-2.389^{+3.270}_{-2.238}$	
A	$-0.5802^{+0.9149}_{-0.4497}$	$-1.353^{+1.485}_{-0.654}$	$-0.6752^{+0.6619}_{-0.3838}$	

Table 11: Best fit values and the marginalized 1 σ errors of parameters f, $f\sigma_{\rm v}$, b_0, Q and A from redshift-space power spectrum, bispectrum and combination of power spectrum and bispectrum for halo fields assuming a hypothetical survey with the volume 1 $h^{-3}\,{\rm Gpc}^3$ at $z = 1$. The results are obtained $k_{\rm max} = 0.15\ h{\rm Mpc}^{-1}$.

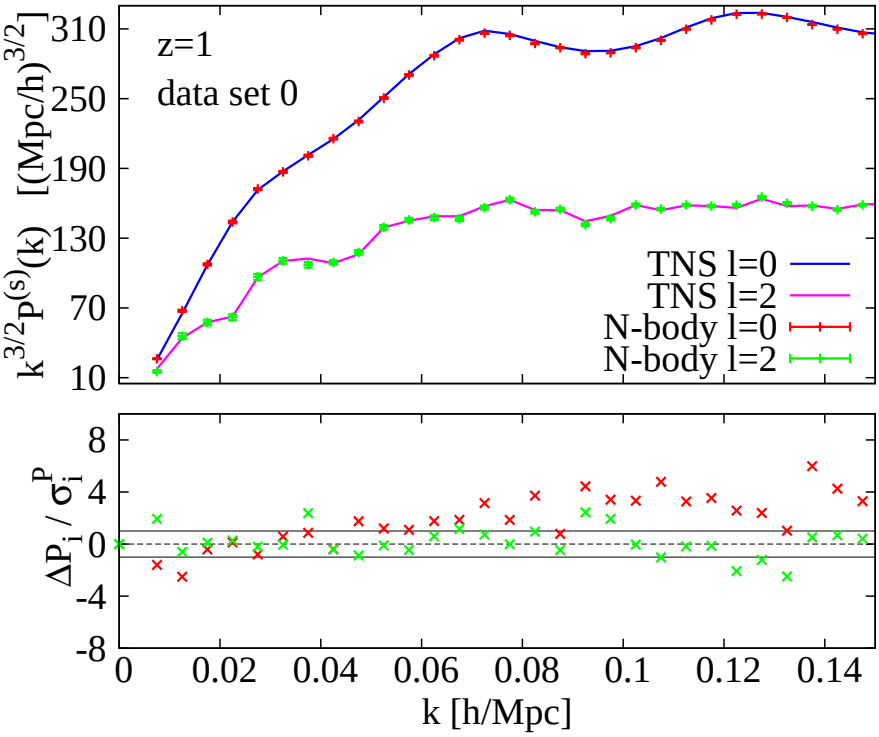

Figure 27: Same as Fig. 22, but in the case of halo power spectra. Five fitting parameters, f, σ'_v, b_0, Q and A. The best-fit power spectra are computed based on TNS model assuming linear bias relation at Eqs.(182) and (183).

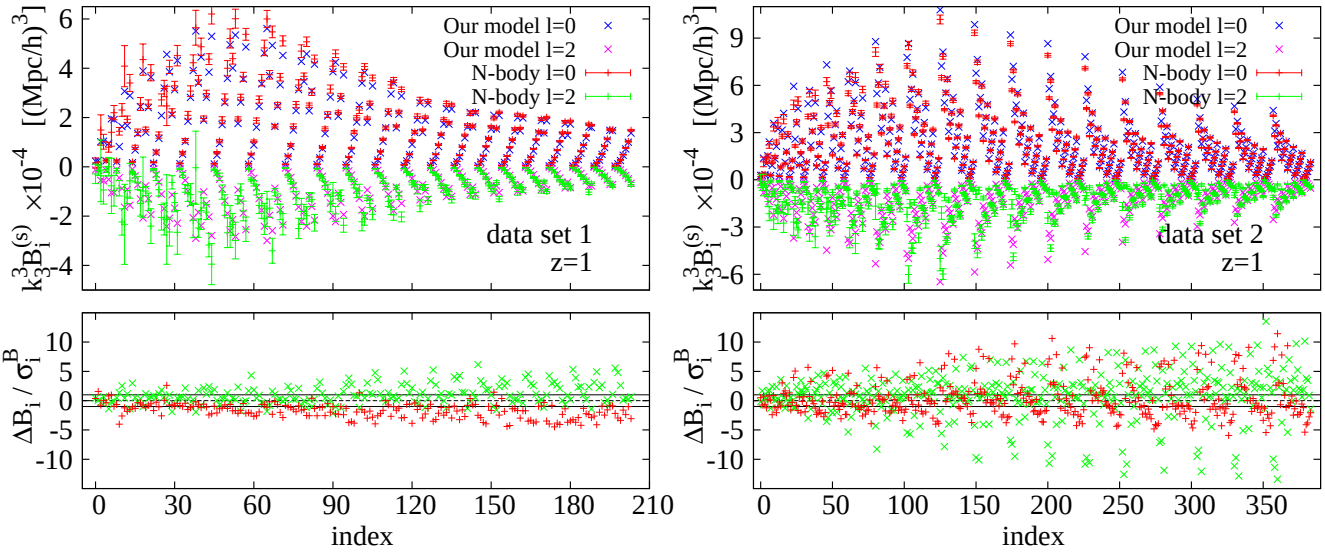

Figure 28: Same as Fig. 23, but in the case of halo catalog, based on our improved bispectrum template combined with linear bias prediction at Eqs.(182) and (183).

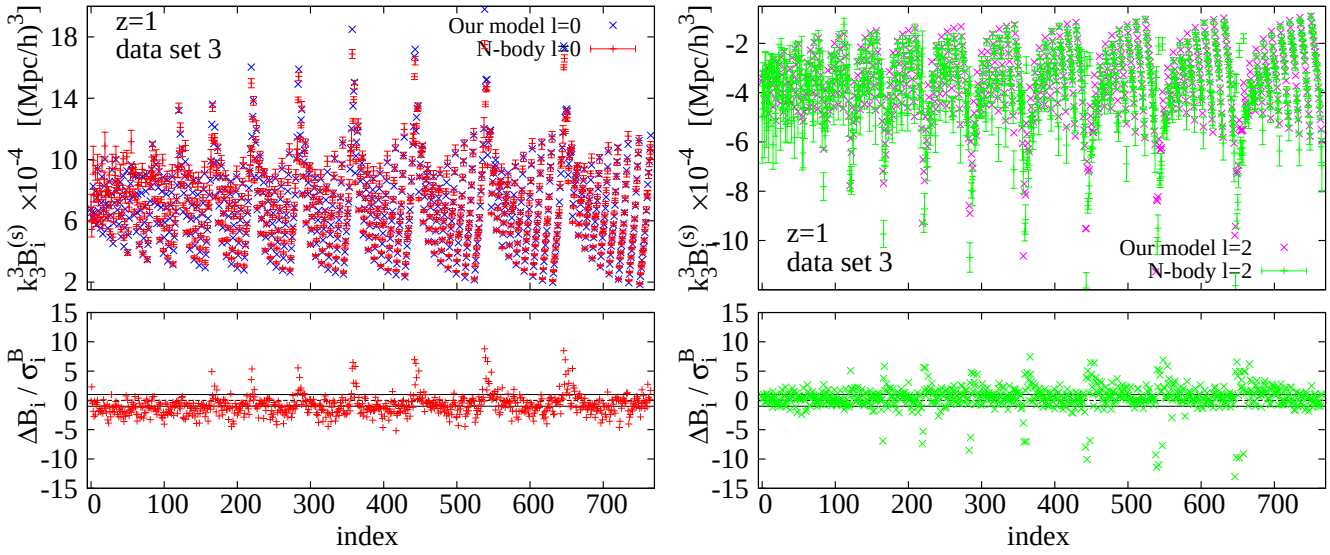

Figure 29: Same as Fig. 24, but in the case of halo catalog.

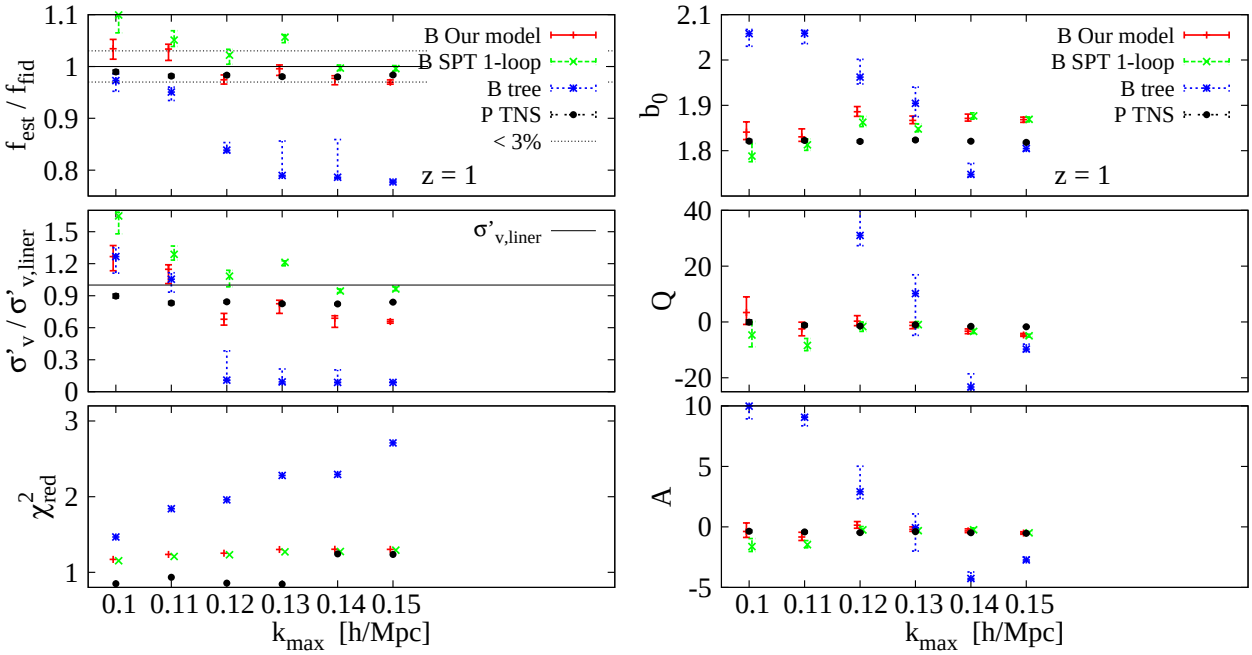

Figure 30: Best-fit values and $\chi^2_{\rm red}$ as function of $k_{\rm max}$ in the case of halo catalog. Dependance of bias parameters on the maximum wavenumber $k_{\rm max}$ is also shown at right panels.

	$P^{(s)}_{\rm model}$: 1-loop	$B^{(s)}_{\rm model}$: 1-loop	$B^{(s)}_{\rm model}$: SPT,1-loop	$B^{(s)}_{\rm model}$: tree	fiducial/linear
f	$0.8558^{+0.0016}_{-0.0016}$	$0.8433^{+0.0039}_{-0.0033}$	$0.8662^{+0.0050}_{-0.0039}$	$0.6760^{+0.0022}_{-0.0014}$	0.8698
σ'_v	$2.654^{+0.016}_{-0.017}$	$2.081^{+0.054}_{-0.047}$	$3.046^{+0.059}_{-0.050}$	$0.2762^{+0.0028}_{-0.0019}$	3.164
b_0	$1.820^{+0.002}_{-0.002}$	$1.868^{+0.006}_{-0.006}$	$1.869^{+0.005}_{-0.006}$	$1.805^{+0.010}_{-0.0051}$	
Q	$-1.526^{+0.179}_{-0.171}$	$-4.693^{+0.572}_{-0.485}$	$-4.942^{+0.537}_{-0.462}$	$-9.708^{+1.770}_{-0.874}$	
A	$-0.4866^{+0.0338}_{-0.0317}$	$-0.5069^{+0.1079}_{-0.1023}$	$-0.4887^{+0.1042}_{-0.0962}$	$-2.733^{+0.235}_{-0.114}$	

Table 12: The best-fit values and the marginalized 1 σ errors of the parameters f, $f\sigma_{\rm v}$, b_0, Q and A from redshift-space power spectrum and bispectrum in halo field at $z = 1$. The results are obtained from the maximum likelihood analysis with MCMC technique up to $k_{\rm max} = 0.15\ h{\rm Mpc}^{-1}$.

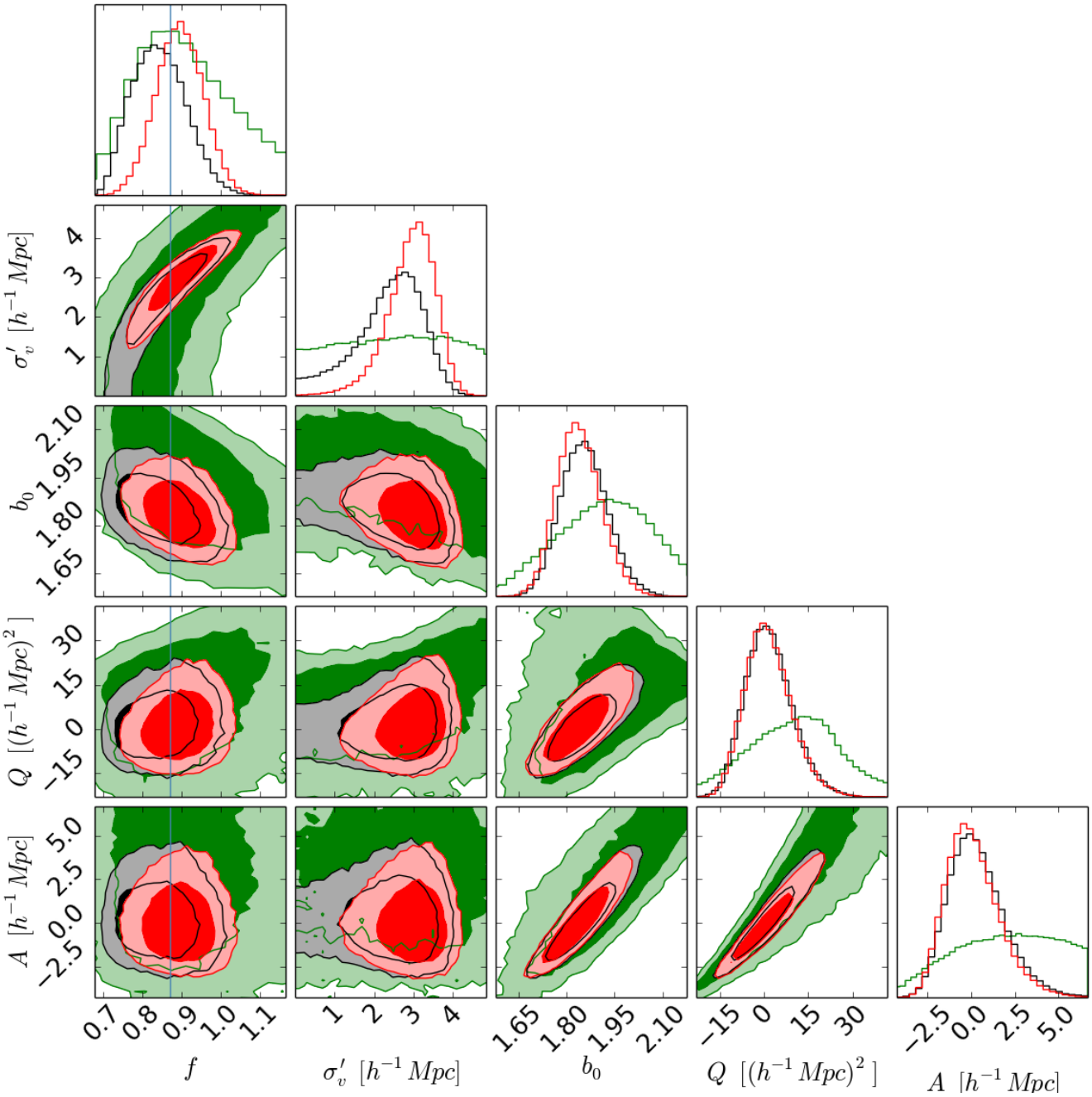

Figure 31: Same as Fig. 26, but the bispectra which do not satisfy the conditions, $k_{2,\mathrm{min}} + k_{3,\mathrm{min}} > k_{1,\mathrm{max}}$ and $\cos\theta_{12} > -0.9$ in this analysis are removed.

	$P^{(s)}_{\rm model}$: 1-loop	$B^{(s)}_{\rm model}$: 1-loop	$P^{(s)}_{\rm model}$ + $B^{(s)}_{\rm model}$: 1-loop	fiducial/linear
f	$0.8568^{+0.0280}_{-0.0367}$	$0.8420^{+0.0830}_{-0.0373}$	$0.8945^{+0.0268}_{-0.0265}$	0.8698
σ'_v	$2.671^{+0.271}_{-0.425}$	$2.027^{+1.178}_{-0.651}$	$2.988^{+0.243}_{-0.263}$	3.164
b_0	$1.817^{+0.045}_{-0.022}$	$1.859^{+0.091}_{-0.058}$	$1.810^{+0.038}_{-0.023}$	
Q	$-2.054^{+4.453}_{-2.487}$	$-5.977^{+14.262}_{-4.249}$	$-2.042^{+4.330}_{-2.397}$	
A	$-0.5802^{+0.9149}_{-0.4497}$	$-0.7531^{+2.5795}_{-0.8427}$	$-0.6506^{+0.8252}_{-0.4373}$	

Table 13: Same as Fig. 11, but the bispectra which do not satisfy the conditions, $k_{2,\rm min} + k_{3,\rm min} > k_{1,\rm max}$ and $\cos\theta_{12} > -0.9$ in this analysis are removed.

Chapter 6 Discussion and conclusion

Despite the considerable success of the standard cosmological model that consistently explains the cosmic expansion and structure formation, the origin of late-time cosmic acceleration has not yet been clarified. To clarify this, in precision cosmology era, a gigantic data will be obtained from upcoming surveys, and measurement of statistical quantities will be made very precisely. Toward future cosmological analysis, improving the accuracy of theoretical template is rather critical. So far, the cosmological constraints on gravity and/or dark energy, obtained from large-scale structure observations, has been mainly made with the theory and measurement of the two-point statistics. However, the large-scale galaxy distribution in the late-time universe exhibits gravity-induced non-Gaussianity, and the bispectrum, three-point cumulant is expected to contain significant cosmological informations together with power spectrum. In particular, the measurement of the bispectrum helps to tighten the constraints on dark energy and modified gravity through the redshift-space distortions (RSD).

In this thesis, toward a robust and severe test of gravity with redshift-space distortions (RSD) from future galaxy redshift surveys, we have presented a perturbation theory (PT) model of redshift-space bispectrum that can keep the non-perturbative damping effect of the redshift-space distortions (RSD) under control. Starting with the exact formula for redshift-space bispectrum, we rewrite the expression in terms of the cumulants to identify the non-perturbative term. Separating the non-perturbative term responsible for the so-called Fingers-of-God (FoG) damping effect, we derive the perturbative expressions for bispectrum valid at one-loop order. The resultant model has been constructed similarly to the TNS model in Ref. [11], and it incorporates the non-perturbative damping term on top of the terms that can be computed with standard PT.

Adopting the Gaussian form of damping function, we have performed a detailed comparison between the predictions of PT model with the measured results of the bispectrum from a suite of cosmological N-body simulations in matter field. Incorporating a single free parameter into the damping function, the one-loop PT model reproduces the simulation results fairly well at weakly nonlinear scales at $z = 0 - 1$. The fitted results of the parameter

σ_v are found to agree well with those obtained from the power spectrum, and the agreement generally holds irrespective of the shape of the triangles. On the other hand, even if we incorporate the damping function into the model, the tree-level PT predictions start to deviate from N-body results at rather low-k. Also, the fitted value σ_v does not match the one obtained from the power spectrum, and varies with triangular shapes.

We have further examined the validity of the ansatz imposed in the functional form of the damping function [Eq. (157)]. Combining the simulation data with standard PT results, we confirmed that the univariate ansatz for damping function $D_{\rm FoG}$ indeed hold for one-loop PT model, and its functional form is shown to be very close to the Gaussian, although the Lorentzian form looks slightly better. Note, however, that in the case of the tree-level PT model, univariate ansatz does not give a good description, and this can be a part of the reason why the failure of tree-level PT prediction appears at rather low-k. Hence, even at large scales, a careful modeling with one-loop correction is essential, and together with the model of power spectrum proposed by Ref. [11], the present one-loop model of bispectrum gives a coherent description for RSD.

From the maximum likelihood analysis using Markov-chain Monte Carlo technique (MCMC), we also investigate the impact of combining power spectrum and bispectrum for constraining growth rate and the accuracy of the estimation, using our improved model of bispectrum in the case of matter and halo fields. For practical data analysis, we develop a fast estimation method of bispectrum multipole as well as the accurate calculation method of the PT-based bispectrum template. Employing these methods, we demonstrate the estimation of growth rate from mock catalog made by N-body simulation assuming a hypothetical survey with the volume $1\,h^{-3}\,{\rm Gpc}^3$ at $z = 1$. Both case of the matter and halo field, the constraints on growth rate from combining power spectrum and bispectrum are 30% tighter than that from power spectrum alone, by solving the degeneracy of parameters between f and σ_v, and the best fit value of f is consistent with fiducial value with 1σ level. However, we find large discrepancy between the bispectrum from N-body simulation and our improved model at squeezed and flattened triangles. A possible reasons for this may be the discreteness of Fourier modes inside the bins and our measurement of bispectrum from N-body simulation. By removing the bispectra of squeezed and flattened triangles, our improved and SPT one-loop models of bispectrum can predict the growth rate accurately without power spectrum, while the best fit value of f from tree model of bispectrum starts to deviate from the fiducial value as increasing $k_{\rm max}$ in matter and halo fields. The

accuracy of estimated f from our improved model is slightly better than that from SPT one-loop model, and within 3% even if we take $k_{\rm max} = 0.15h^{-1}$Mpc. Removing the bispectra of squeezed and flattened triangles, the constraint on growth rate from combining power spectrum and bispectrum becomes week, but the constraint is still improved 17% compare to the analysis of power spectrum alone in halo fields. Despite the fact that the number of triangles is reduced by $\sim 40\%$, this improvement of the constraint on f is rather comparable to the result by Ref. [62], in which they combined the power spectrum with bispectrum monopole only, and used the data at $z = 0.57$ up to higher $k_{\rm max}$ ($\simeq 0.2\,h\,{\rm Mpc}^{-1}$). It proves that including bispectrum quadrupole indeed plays an important role to tighten the constraint on f. We thus conclude that the data analysis including the anisotropic bispectrum data is crucial for future galaxy surveys, and the analysis and methods developed in this thesis, including the fast estimation of bispectrum and the accelerated calculation of PT-based template, are valuable and helpful.

Finally, we note that toward the practical application to real applications, there still remain several issues to be addressed. One is the improvement of the PT prediction. Including the higher-order (two-loop) corrections or applying the resummation technique, the applicable range of PT is expected to become wider, and a more tighter test of gravity will be made. Effective field theory approach may also help to improve the prediction (e.g., Refs. [90, 91, 92, 93]). Another issue is the estimation of statistical error covariance of bispectrum, which is crucial and necessary for unbiased and robust cosmological data analysis. The N-body measurement of the covariance is, however, known to be computationally extensive (e.g., Refs. [56, 57] for weak lensing case), and a clever approach, involving the analytic treatment, may have to be developed, for instance. The cross covariance between power spectrum and bispectrum is also important for the precise estimation of growth rate. In this thesis, we treat the power spectrum and bispectrum is independent, but the constraint on parameters from their combination can be weaken by considering the cross covariance of them. The treatment of bispectra of squeezed and flattened triangles are also the important issue. To perform further tight and accurate constraint by combining bispectrum, we need more careful treatment for these bispectra. One final big issue is the galaxy biasing. Throughout the thesis, we have employed the linear bias model, but the observations imply that the galaxy bias has the non-linearity and stochasticity. Especially, the second order bias effect appears in the leading order of bispectrum. Incorporating the realistic galaxy bias model is thus very crucial.

Bibliography

[1] E. G. Adelberger, Blayne R. Heckel, and A. E. Nelson. Tests of the gravitational inverse square law. *Ann. Rev. Nucl. Part. Sci.*, Vol. 53, pp. 77–121, 2003.

[2] Ayumu Terukina, Lucas Lombriser, Kazuhiro Yamamoto, David Bacon, Kazuya Koyama, and Robert C. Nichol. Testing chameleon gravity with the Coma cluster. *JCAP*, Vol. 1404, p. 013, 2014.

[3] M. Davis and P. J. E. Peebles. A survey of galaxy redshifts. V - The two-point position and velocity correlations. *Astrophys. J.*, Vol. 267, pp. 465–482, April 1983.

[4] N. Kaiser. Clustering in real space and in redshift space. *Mon. Not. Roy. Astron. Soc.*, Vol. 227, pp. 1–27, 1987.

[5] A. J. S. Hamilton. Measuring Omega and the real correlation function from the redshift correlation function. *Astrophys. J.*, Vol. 385, pp. L5–L8, 1992.

[6] Roman Scoccimarro. Redshift-space distortions, pairwise velocities and nonlinearities. *Phys. Rev.*, Vol. D70, p. 083007, 2004.

[7] J. C. Jackson. A critique of Rees's theory of primordial gravitational radiation. *Mon. Not. Roy. Astron. Soc.*, Vol. 156, p. 1P, 1972.

[8] D. J. Eisenstein and W. Hu. Baryonic Features in the Matter Transfer Function. *Astrophys. J.*, Vol. 496, pp. 605–614, March 1998.

[9] A. Meiksin, Martin J. White, and J. A. Peacock. Baryonic Signatures in Large-Scale Structure. 1998.

[10] Daniel J. Eisenstein, et al. Detection of the Baryon Acoustic Peak in the Large-Scale Correlation Function of SDSS Luminous Red Galaxies. *Astrophys. J.*, Vol. 633, pp. 560–574, 2005.

[11] Atsushi Taruya, Takahiro Nishimichi, and Shun Saito. Baryon Acoustic Oscillations in 2D: Modeling Redshift-space Power Spectrum from Perturbation Theory. *Phys. Rev.*, Vol. D82, p. 063522, 2010.

[12] B. A. Reid, L. Samushia, M. White, W. J. Percival, M. Manera, N. Padmanabhan, A. J. Ross, A. G. Sánchez, S. Bailey, D. Bizyaev, A. S. Bolton, H. Brewington, J. Brinkmann, J. R. Brownstein, A. J. Cuesta, D. J. Eisenstein, J. E. Gunn, K. Honscheid, E. Malanushenko, V. Malanushenko, C. Maraston, C. K. McBride, D. Muna, R. C. Nichol, D. Oravetz, K. Pan, R. de Putter, N. A. Roe, N. P. Ross, D. J. Schlegel, D. P. Schneider, H.-J. Seo, A. Shelden, E. S. Sheldon, A. Simmons, R. A. Skibba, S. Snedden, M. E. C. Swanson, D. Thomas, J. Tinker, R. Tojeiro, L. Verde, D. A. Wake, B. A. Weaver, D. H. Weinberg, I. Zehavi, and G.-B. Zhao. The clustering of galaxies in the SDSS-III Baryon Oscillation Spectroscopic Survey: measurements of the growth of structure and expansion rate at z = 0.57 from anisotropic clustering. *Mon. Not. Roy. Astron. Soc.*, Vol. 426, pp. 2719–2737, November 2012.

[13] Akira Oka, Shun Saito, Takahiro Nishimichi, Atsushi Taruya, and Kazuhiro Yamamoto. Simultaneous constraints on the growth of structure and cosmic expansion from the multipole power spectra of the SDSS DR7 LRG sample. *Mon. Not. Roy. Astron. Soc.*, Vol. 439, pp. 2515–2530, 2014.

[14] Florian Beutler, et al. The clustering of galaxies in the SDSS-III Baryon Oscillation Spectroscopic Survey: Testing gravity with redshift-space distortions using the power spectrum multipoles. 2013.

[15] Eric V. Linder. Redshift Distortions as a Probe of Gravity. *Astropart. Phys.*, Vol. 29, pp. 336–339, 2008.

[16] Hee-Jong Seo and Daniel J. Eisenstein. Probing dark energy with baryonic acoustic oscillations from future large galaxy redshift surveys. *Astrophys. J.*, Vol. 598, pp. 720–740, 2003.

[17] Chris Blake and Karl Glazebrook. Probing dark energy using baryonic oscillations in the galaxy power spectrum as a cosmological ruler. *Astrophys. J.*, Vol. 594, pp. 665–673, 2003.

[18] Karl Glazebrook and Chris Blake. Measuring the cosmic evolution of dark energy with baryonic oscillations in the galaxy power spectrum. *Astrophys. J.*, Vol. 631, pp. 1–20, 2005.

[19] Y.-S. Song, A. Taruya, E. Linder, K. Koyama, C. G. Sabiu, G.-B. Zhao, F. Bernardeau, T. Nishimichi, and T. Okumura. Consistent modified gravity analysis of anisotropic galaxy clustering using BOSS DR11. *Physical Review D*, Vol. 92, No. 4, p. 043522, August 2015.

[20] Beth A. Reid and Martin White. Towards an accurate model of the redshift space clustering of halos in the quasilinear regime. *Mon. Not. Roy. Astron. Soc.*, Vol. 417, pp. 1913–1927, 2011.

[21] Zvonimir Vlah, Uros Seljak, Patrick McDonald, Teppei Okumura, and Tobias Baldauf. Distribution function approach to redshift space distortions. Part IV: perturbation theory applied to dark matter. *JCAP*, Vol. 1211, p. 009, 2012.

[22] Takahiko Matsubara. Resumming Cosmological Perturbations via the Lagrangian Picture: One-loop Results in Real Space and in Redshift Space. *Phys. Rev.*, Vol. D77, p. 063530, 2008.

[23] Takahiko Matsubara. Nonlinear perturbation theory with halo bias and redshift-space distortions via the Lagrangian picture. *Phys. Rev.*, Vol. D78, p. 083519, 2008. [Erratum: Phys. Rev.D78,109901(2008)].

[24] Jordan Carlson, Beth Reid, and Martin White. Convolution Lagrangian perturbation theory for biased tracers. *Mon. Not. Roy. Astron. Soc.*, Vol. 429, p. 1674, 2013.

[25] Takahiko Matsubara. Integrated Perturbation Theory and One-loop Power Spectra of Biased Tracers. *Phys. Rev.*, Vol. D90, No. 4, p. 043537, 2014.

[26] A. Taruya, T. Nishimichi, and F. Bernardeau. Precision modeling of redshift-space distortions from a multipoint propagator expansion. *Physical Review D*, Vol. 87, No. 8, p. 083509, April 2013.

[27] H. Gil-Marín, C. Wagner, F. Fragkoudi, R. Jimenez, and L. Verde. An improved fitting formula for the dark matter bispectrum. *JCAP*, Vol. 2, p. 047, February 2012.

[28] R. Scoccimarro and H. M. P. Couchman. A fitting formula for the non-linear evolution of the bispectrum. *Mon. Not. Roy. Astron. Soc.*, Vol. 325, pp. 1312–1316, August 2001.

[29] R. E. Smith, R. K. Sheth, and R. Scoccimarro. Analytic model for the bispectrum of galaxies in redshift space. *Phys. Rev.*, Vol. 78, No. 2, p. 023523, July 2008.

[30] Kazuhiro Yamamoto, Yue Nan, and Chiaki Hikage. An analytic halo approach to the bispectrum of galaxies in redshift space. 2016.

[31] C. Rampf and Y. Y. Y. Wong. Lagrangian perturbations and the matter bispectrum II: the resummed one-loop correction to the matter bispectrum. *JCAP*, Vol. 6, p. 018, June 2012.

[32] P. A. R. Ade, et al. Planck 2015 results. XIII. Cosmological parameters. *Astron. Astrophys.*, Vol. 594, p. A13, 2016.

[33] Steven Winberg. COSMOLOGY. *OXFORD UNIVERSITY PRESS*, 2008.

[34] V. Silveira and I. Waga. Decaying Λ cosmologies and power spectrum. *Phys. Rev.*, Vol. 50, pp. 4890–4894, October 1994.

[35] R. Teyssier. Cosmological hydrodynamics with adaptive mesh refinement. A new high resolution code called RAMSES. *Astronomy & Astrophysics*, Vol. 385, pp. 337–364, April 2002.

[36] S. Prunet, C. Pichon, D. Aubert, D. Pogosyan, R. Teyssier, and S. Gottloeber. Initial Conditions For Large Cosmological Simulations. *The Astrophysical Journal Supplement Series*, Vol. 178, pp. 179–188, October 2008.

[37] Roman Scoccimarro, Stephane Colombi, James N. Fry, Joshua A. Frieman, Eric Hivon, and Adrian Melott. Nonlinear evolution of the bispectrum of cosmological perturbations. *Astrophys. J.*, Vol. 496, p. 586, 1998.

[38] M. Crocce, S. Pueblas, and R. Scoccimarro. Transients from Initial Conditions in Cosmological Simulations. *Mon. Not. Roy. Astron. Soc.*, Vol. 373, pp. 369–381, 2006.

[39] Volker Springel. The Cosmological simulation code GADGET-2. *Mon. Not. Roy. Astron. Soc.*, Vol. 364, pp. 1105–1134, 2005.

[40] Volker Springel, Naoki Yoshida, and Simon D. M. White. GADGET: A Code for collisionless and gasdynamical cosmological simulations. *New Astron.*, Vol. 6, p. 79, 2001.

[41] F. Bernardeau, S. Colombi, E. Gaztañaga, and R. Scoccimarro. Large-scale structure of the Universe and cosmological perturbation theory. *Physics Reports*, Vol. 367, pp. 1–248, September 2002.

[42] Eric V. Linder. Cosmic growth history and expansion history. *Phys. Rev.*, Vol. D72, p. 043529, 2005.

[43] Massimo Pietroni. Flowing with Time: a New Approach to Nonlinear Cosmological Perturbations. *JCAP*, Vol. 0810, p. 036, 2008.

[44] Ryuichi Takahashi. Third Order Density Perturbation and One-loop Power Spectrum in a Dark Energy Dominated Universe. *Prog. Theor. Phys.*, Vol. 120, pp. 549–559, 2008.

[45] T. Hiramatsu and A. Taruya. Chasing the nonlinear evolution of matter power spectrum with a numerical resummation method: Solution of closure equations. *Phys. Rev.*, No. 10, p. 103526, May 2009.

[46] Roman Scoccimarro, H. M. P. Couchman, and Joshua A. Frieman. The Bispectrum as a signature of gravitational instability in redshift-space. *Astrophys. J.*, Vol. 517, pp. 531–540, 1999.

[47] Ichihiko Hashimoto, Yann Rasera, and Atsushi Taruya. Precision cosmology with redshift-space bispectrum: a perturbation theory based model at one-loop order. *Phys. Rev.*, Vol. D96, No. 4, p. 043526, 2017.

[48] L. Guzzo, et al. A test of the nature of cosmic acceleration using galaxy redshift distortions. *Nature*, Vol. 451, pp. 541–545, 2008.

[49] Teppei Okumura, et al. The Subaru FMOS galaxy redshift survey (FastSound). IV. New constraint on gravity theory from redshift space distortions at $z \sim 1.4$. *Publ. Astron. Soc. Jap.*, Vol. 68, No. 3, id. 38, p. 24, 2016.

[50] S. de la Torre, L. Guzzo, J. A. Peacock, E. Branchini, A. Iovino, B. R. Granett, U. Abbas, C. Adami, S. Arnouts, J. Bel, M. Bolzonella, D. Bottini, A. Cappi, J. Coupon, O. Cucciati, I. Davidzon, G. De Lucia, A. Fritz, P. Franzetti, M. Fumana, B. Garilli, O. Ilbert, J. Krywult, V. Le Brun, O. Le Fèvre, D. Maccagni, K. Małek, F. Marulli, H. J. McCracken, L. Moscardini, L. Paioro, W. J. Percival, M. Polletta, A. Pollo, H. Schlagenhaufer, M. Scodeggio, L. A. M. Tasca, R. Tojeiro, D. Vergani, A. Zanichelli, A. Burden, C. Di Porto, A. Marchetti, C. Marinoni, Y. Mellier, P. Monaco, R. C. Nichol, S. Phleps, M. Wolk, and G. Zamorani. The VIMOS Public Extragalactic Redshift Survey (VIPERS) . Galaxy clustering and redshift-space distortions at z $\simeq$ 0.8 in the first data release. *Astron. Astrophys.*, Vol. 557, p. A54, September 2013.

[51] Florian Beutler, et al. The clustering of galaxies in the completed SDSS-III Baryon Oscillation Spectroscopic Survey: Anisotropic galaxy clustering in Fourier-space. *Submitted to: Mon. Not. Roy. Astron. Soc.*, 2016.

[52] Chris Blake, Sarah Brough, Matthew Colless, Carlos Contreras, Warrick Couch, et al. The WiggleZ Dark Energy Survey: the growth rate of cosmic structure since redshift z=0.9. *Mon. Not. Roy. Astron. Soc.*, Vol. 415, p. 2876, 2011.

[53] Planck Collaboration, P. A. R. Ade, N. Aghanim, M. Arnaud, M. Ashdown, J. Aumont, C. Baccigalupi, A. J. Banday, R. B. Barreiro, J. G. Bartlett, and et al. Planck 2015 results. XIII. Cosmological parameters. *Astron. Astrophys.*, Vol. 594, p. A13, September 2016.

[54] Planck Collaboration, P. A. R. Ade, N. Aghanim, M. Arnaud, M. Ashdown, J. Aumont, C. Baccigalupi, A. J. Banday, R. B. Barreiro, J. G. Bartlett, and et al. Planck 2015 results. XIII. Cosmological parameters. *ArXiv e-prints*, February 2015.

[55] Emiliano Sefusatti, Martin Crocce, Sebastian Pueblas, and Roman Scoccimarro. Cosmology and the Bispectrum. *Phys. Rev.*, Vol. D74, p. 023522, 2006.

[56] I. Kayo, M. Takada, and B. Jain. Information content of weak lensing power spectrum and bispectrum: including the non-Gaussian error covariance matrix. *Mon. Not. Roy. Astron. Soc.*, Vol. 429, pp. 344–371, February 2013.

[57] Masanori Sato and Takahiro Nishimichi. Impact of the non-Gaussian covariance of the weak lensing power spectrum and bispectrum on cosmological parameter estimation. *Phys. Rev.*, Vol. D87, p. 123538, 2013.

[58] Bradley Greig, Eiichiro Komatsu, and J. Stuart B. Wyithe. Cosmology from clustering of Lyman-alpha galaxies: breaking non-gravitational Lyman-alpha radiative transfer degeneracies using the bispectrum. *Mon. Not. Roy. Astron. Soc.*, Vol. 431, p. 1777, 2013.

[59] J. Byun, A. Eggemeier, D. Regan, D. Seery, and R. E. Smith. Towards optimal cosmological parameter recovery from compressed bispectrum statistics. *ArXiv e-prints*, May 2017.

[60] Yong-Seon Song, Atsushi Taruya, and Akira Oka. Cosmology with anisotropic galaxy clustering from the combination of power spectrum and bispectrum. *JCAP*, Vol. 1508, No. 08, p. 007, 2015.

[61] P. Gagrani and L. Samushia. Information Content of the Angular Multipoles of Redshift-Space Galaxy Bispectrum. *Mon. Not. Roy. Astron. Soc.*, January 2017.

[62] Hctor Gil-Marn, Will J. Percival, Licia Verde, Joel R. Brownstein, Chia-Hsun Chuang, Francisco-Shu Kitaura, Sergio A. Rodrguez-Torres, and Matthew D. Olmstead. The clustering of galaxies in the SDSS-III Baryon Oscillation Spectroscopic Survey: RSD measurement from the power spectrum and bispectrum of the DR12 BOSS galaxies. *Mon. Not. Roy. Astron. Soc.*, Vol. 465, No. 2, pp. 1757–1788, 2017.

[63] David W. Pearson and Lado Samushia. A Detection of the Baryon Acoustic Oscillation Features in the SDSS BOSS DR12 Galaxy Bispectrum. 2017.

[64] Yue Nan, Kazuhiro Yamamoto, and Chiaki Hikage. Higher multipoles of the galaxy bispectrum in redshift space. 2017.

[65] Hctor Gil-Marn, et al. The clustering of galaxies in the SDSS-III Baryon Oscillation Spectroscopic Survey: RSD measurement from the LOS-dependent power spectrum of DR12 BOSS galaxies. *Mon. Not. Roy. Astron. Soc.*, Vol. 460, No. 4, pp. 4188–4209, 2016.

[66] R. Scoccimarro. Fast estimators for redshift-space clustering. *Phys. Rev. D*, Vol. 92, No. 8, p. 083532, October 2015.

[67] L. Blot, P. S. Corasaniti, J.-M. Alimi, V. Reverdy, and Y. Rasera. Matter power spectrum covariance matrix from the DEUS-PUR ΛCDM simulations: mass resolution and non-Gaussian errors. *Mon. Not. Roy. Astron. Soc.*, Vol. 446, pp. 1756–1764, January 2015.

[68] Y. Rasera, P.-S. Corasaniti, J.-M. Alimi, V. Bouillot, V. Reverdy, and I. Balmès. Cosmic-variance limited Baryon Acoustic Oscillations from the DEUS-FUR ΛCDM simulation. *Mon. Not. Roy. Astron. Soc.*, Vol. 440, pp. 1420–1434, May 2014.

[69] Ryuichi Takahashi, et al. Simulations of Baryon Acoustic Oscillations I: Growth of Large-Scale Density Fluctuations. *Mon. Not. Roy. Astron. Soc.*, Vol. 389, p. 1675, 2008.

[70] Katrin Heitmann, Martin White, Christian Wagner, Salman Habib, and David Higdon. The Coyote Universe I: Precision Determination of the Nonlinear Matter Power Spectrum. *Astrophys. J.*, Vol. 715, pp. 104–121, 2010.

[71] Katrin Heitmann, David Higdon, Martin White, Salman Habib, Brian J. Williams, and Christian Wagner. The Coyote Universe II: Cosmological Models and Precision Emulation of the Nonlinear Matter Power Spectrum. *Astrophys. J.*, Vol. 705, pp. 156–174, 2009.

[72] E. Lawrence, K. Heitmann, M. White, D. Higdon, C. Wagner, S. Habib, and B. Williams. The Coyote Universe. III. Simulation Suite and Precision Emulator for the Nonlinear Matter Power Spectrum. *Astrophys. J.*, Vol. 713, pp. 1322–1331, April 2010.

[73] Katrin Heitmann, Earl Lawrence, Juliana Kwan, Salman Habib, and David Higdon. The Coyote Universe Extended: Precision Emulation of the Matter Power Spectrum. *Astrophys. J.*, Vol. 780, p. 111, 2014.

[74] A. Schneider, R. Teyssier, D. Potter, J. Stadel, J. Onions, D. S. Reed, R. E. Smith, V. Springel, F. R. Pearce, and R. Scoccimarro. Matter power spectrum and the challenge of percent accuracy. *JCAP*, Vol. 4, p. 047, April 2016.

[75] Takahiro Nishimichi, et al. Modeling Nonlinear Evolution of Baryon Acoustic Oscillations: Convergence Regime of N-body Simulations and Analytic Models. *Publ. Astron. Soc. Jap.*, Vol. 61, p. 321, 2009.

[76] Tobias Baldauf, Lorenzo Mercolli, Mehrdad Mirbabayi, and Enrico Pajer. The Bispectrum in the Effective Field Theory of Large Scale Structure. *JCAP*, Vol. 1505, No. 05, p. 007, 2015.

[77] Roman Scoccimarro. Fast Estimators for Redshift-Space Clustering. *Phys. Rev.*, Vol. D92, No. 8, p. 083532, 2015.

[78] M. Davis, G. Efstathiou, C. S. Frenk, and S. D. M. White. The evolution of large-scale structure in a universe dominated by cold dark matter. *Astrophysical Journal*, Vol. 292, pp. 371–394, May 1985.

[79] Volker Springel, Simon D. M. White, Giuseppe Tormen, and Guinevere Kauffmann. Populating a cluster of galaxies. 1. Results at z = 0. *Mon. Not. Roy. Astron. Soc.*, Vol. 328, p. 726, 2001.

[80] D. Foreman-Mackey, D. W. Hogg, D. Lang, and J. Goodman. emcee: The MCMC Hammer. *Publications of the Astronomical Society of the Pacific*, Vol. 125, p. 306, March 2013.

[81] Daniel Foreman-Mackey. corner.py: Scatterplot matrices in python. *The Journal of Open Source Software*, Vol. 24, , 2016.

[82] M. Takada, R. S. Ellis, M. Chiba, J. E. Greene, H. Aihara, N. Arimoto, K. Bundy, J. Cohen, O. Doré, G. Graves, J. E. Gunn, T. Heckman, C. M. Hirata, P. Ho, J.-P. Kneib, O. Le Fèvre, L. Lin, S. More, H. Murayama, T. Nagao, M. Ouchi, M. Seiffert, J. D. Silverman, L. Sodré, D. N. Spergel, M. A. Strauss, H. Sugai, Y. Suto, H. Takami, and R. Wyse. Extragalactic science, cosmology, and Galactic archaeology with the Subaru Prime Focus Spectrograph. *Publications of the Astronomical Society of Japan*, Vol. 66, p. R1, February 2014.

[83] H. J. Mo and S. D. M. White. An analytic model for the spatial clustering of dark matter haloes. *Mon. Not. Roy. Astron. Soc.*, Vol. 282, pp. 347–361, September 1996.

[84] James N. Fry and Enrique Gaztanaga. Biasing and hierarchical statistics in large scale structure. *Astrophys. J.*, Vol. 413, pp. 447–452, 1993.

[85] Vincent Desjacques, Donghui Jeong, and Fabian Schmidt. Large-Scale Galaxy Bias. 2016.

[86] T. Nishimichi and A. Taruya. Baryon acoustic oscillations in 2D. II. Redshift-space halo clustering in N-body simulations. *Physical Review D*, Vol. 84, No. 4, p. 043526, August 2011.

[87] Nick Kaiser. On the Spatial correlations of Abell clusters. *Astrophys. J.*, Vol. 284, pp. L9–L12, 1984.

[88] Shaun Cole, et al. The 2dF Galaxy Redshift Survey: Power-spectrum analysis of the final dataset and cosmological implications. *Mon. Not. Roy. Astron. Soc.*, Vol. 362, pp. 505–534, 2005.

[89] Takashi Ishikawa, Tomonori Totani, Takahiro Nishimichi, Ryuichi Takahashi, Naoki Yoshida, and Motonari Tonegawa. On the Systematic Errors of Cosmological-Scale Gravity Tests using Redshift Space Distortion: Non-linear Effects and the Halo Bias. *Mon. Not. Roy. Astron. Soc.*, Vol. 443, No. 4, pp. 3359–3367, 2014.

[90] D. Baumann, A. Nicolis, L. Senatore, and M. Zaldarriaga. Cosmological non-linearities as an effective fluid. *JCAP*, Vol. 7, p. 51, July 2012.

[91] J. J. M. Carrasco, M. P. Hertzberg, and L. Senatore. The effective field theory of cosmological large scale structures. *Journal of High Energy Physics*, Vol. 9, p. 82, September 2012.

[92] M. P. Hertzberg. Effective field theory of dark matter and structure formation: Semi-analytical results. *Physical Review D*, Vol. 89, No. 4, p. 043521, February 2014.

[93] Tobias Baldauf, Lorenzo Mercolli, and Matias Zaldarriaga. Effective field theory of large scale structure at two loops: The apparent scale dependence of the speed of sound. *Physical Review D*, Vol. 92, No. 12, p. 123007, 2015.

Appendix A Perturbative calculations for D_1 and D_2 terms

In this Appendix, we present the perturbative expressions for the D_1 and D_2 terms defined in Eq. (150), relevant at one-loop order calculations.

First note that Eq. (150) is expressed in terms of the real-space quantities, including the auto- and cross-power spectra and bispectra of density and velocity fields. For convenience, we introduce the two-component multiplet:

$$\Psi_a(\boldsymbol{k}) = \Big(\delta(\boldsymbol{k}),\, \theta(\boldsymbol{k})\Big), \tag{184}$$

with θ being the dimensionless velocity divergence defined in real space by $\theta(\boldsymbol{x}) = -\nabla \cdot \boldsymbol{v}/(f\,aH)$. Then the auto- and cross-power spectra and bispectra are given by

$$(2\pi)^3\delta_{\rm D}(\boldsymbol{k}_1 + \boldsymbol{k}_2)\, P_{ab}(k_1) \equiv \langle \Psi_a(\boldsymbol{k}_1)\Psi_b(\boldsymbol{k}_2)\rangle, \tag{185}$$

$$(2\pi)^3\delta_{\rm D}(\boldsymbol{k}_1 + \boldsymbol{k}_2 + \boldsymbol{k}_3)\, B_{abc}(\boldsymbol{k}_1, \boldsymbol{k}_2, \boldsymbol{k}_3) \equiv \langle \Psi_a(\boldsymbol{k}_1)\Psi_b(\boldsymbol{k}_2)\Psi_c(\boldsymbol{k}_3)\rangle, \tag{186}$$

where subscripts a, b, c run from 1 to 2.

Since the integrand of the D_1 and D_2 terms respectively involves $B_{abc}P_{de}$ and $P_{ab}P_{cd}P_{ef}$, the leading-order non-vanishing contributions become $O(P_{\rm L}^3)$. This is the same order as in the one-loop redshift-space bispectrum. Hence, the tree-level calculations of P_{ab} and B_{abc} are sufficient for a consistent one-loop treatment of redshift-space bispectrum. That is,

$$P_{ab}(k) \simeq P_{\rm L}(k), \tag{187}$$

$$B_{abc}(\boldsymbol{k}_1, \boldsymbol{k}_2, \boldsymbol{k}_3) \simeq 2\Big\{\mathcal{F}_a(\boldsymbol{k}_2, \boldsymbol{k}_3)\, P_{\rm L}(k_2)P_{\rm L}(k_3) + \mathcal{F}_b(\boldsymbol{k}_1, \boldsymbol{k}_3)\, P_{\rm L}(k_1)P_{\rm L}(k_3) + \mathcal{F}_c(\boldsymbol{k}_1, \boldsymbol{k}_2)\, P_{\rm L}(k_1)P_{\rm L}(k_2)\Big\}, \tag{188}$$

where the kernel $\mathcal{F}_a$ is the standard PT kernels at second-order, given by $\mathcal{F}_a = (F_2, G_2)$. Below, we will separately present the explicit expressions for D_1 and D_2 terms. In doing

so, we use the following expressions for the cumulants:

$$\langle A_1A_2A_3\rangle_c = \int \frac{d^3\boldsymbol{p}_1 d^3\boldsymbol{p}_2}{(2\pi)^6}\, e^{i\{\boldsymbol{p}_1\cdot\boldsymbol{r}_{13}+\boldsymbol{p}_2\cdot\boldsymbol{r}_{23}\}} \sum_{a,b,c=1}^{2} f^{a+b+c-3}\mu_{p_1}^{2(a-1)}\mu_{p_2}^{2(b-1)}\mu_{p_3}^{2(c-1)}\, B_{abc}(\boldsymbol{p}_1,\boldsymbol{p}_2,\boldsymbol{p}_3), \tag{189}$$

$$\langle (j_4A_4+j_5A_5)^2\rangle_c = -f^2\int \frac{d^3\boldsymbol{p}}{(2\pi)^3}\,\frac{\mu_p^2}{p^2}\,P_{22}(p) \times\Big\{(k_1\mu_1)^2+(k_2\mu_2)^2+(k_3\mu_3)^2+2\big(k_1k_2\mu_1\mu_2e^{i\boldsymbol{p}\cdot\boldsymbol{r}_{12}}+k_1k_3\mu_1\mu_3e^{i\boldsymbol{p}\cdot\boldsymbol{r}_{13}}+k_2k_3\mu_2\mu_3e^{i\boldsymbol{p}\cdot\boldsymbol{r}_{23}}\big)\Big\}, \tag{190}$$

$$\langle A_1A_2\rangle_c = \int \frac{d^3\boldsymbol{p}}{(2\pi)^3}\, e^{i\boldsymbol{p}\cdot\boldsymbol{r}_{12}}\Big\{P_{11}(p)+2f\mu_p^2\,P_{12}(p)+f^2\mu_p^4P_{22}(p)\Big\}, \tag{191}$$

$$\langle (j_4A_4+j_5A_5)A_3)\rangle_c = -f\int \frac{d^3\boldsymbol{p}}{(2\pi)^3}\,\frac{\mu_p}{p}\Big\{P_{12}(p)+f\mu_p^2P_{22}(p)\Big\}\Big\{k_1\mu_1\,e^{i\boldsymbol{p}\cdot\boldsymbol{r}_{13}}+k_2\mu_2\,e^{i\boldsymbol{p}\cdot\boldsymbol{r}_{23}}+k_3\mu_3\Big\} \tag{192}$$

with the quantities μ_i and μ_p respectively defined by $\mu_i = (\boldsymbol{k}_i\cdot\hat{\boldsymbol{z}})/k_i$ and $\mu_p = (\boldsymbol{p}\cdot\hat{\boldsymbol{z}})/p$.

A.1 D_1 term

According to Eq. (150), the D_1 term is explicitly written as

$$D_1(\boldsymbol{k}_1,\boldsymbol{k}_2,\boldsymbol{k}_3) = \frac{1}{2}\int d^3\boldsymbol{r}_{13}d^3\boldsymbol{r}_{23}\, e^{i(\boldsymbol{k}_1\cdot\boldsymbol{r}_{13}+\boldsymbol{k}_2\cdot\boldsymbol{r}_{23})}\,\langle A_1A_2A_3\rangle_c\,\langle (j_4A_4+j_5A_5))^2\rangle_c. \tag{193}$$

Substituting Eq. (189) and (190) into the above, we obtain

$$\begin{aligned} D_1(\boldsymbol{k}_1,\boldsymbol{k}_2,\boldsymbol{k}_3) = &-\frac{f^2}{2}\Big\{(k_1\mu_1)^2+(k_2\mu_2)^2+(k_3\mu_3)^2\Big\}\sigma_{\rm v,lin}^2\,C_1(\boldsymbol{k}_1,\boldsymbol{k}_2,\boldsymbol{k}_3) \\ &- f^2\int \frac{d^3\boldsymbol{p}}{(2\pi)^3}\frac{\mu_p^2}{p^2}P_{22}(p)\Big\{(k_1k_2\mu_1\mu_2)\,C_1(\boldsymbol{k}_1+\boldsymbol{p},\,\boldsymbol{k}_2-\boldsymbol{p},\,\boldsymbol{k}_3) \\ &+(k_1k_3\mu_1\mu_3)\,C_1(\boldsymbol{k}_1+\boldsymbol{p},\,\boldsymbol{k}_2,\,\boldsymbol{k}_3-\boldsymbol{p})+(k_2k_3\mu_2\mu_3)\,C_1(\boldsymbol{k}_1,\,\boldsymbol{k}_2+\boldsymbol{p},\,\boldsymbol{k}_3-\boldsymbol{p})\Big\} \end{aligned} \tag{194}$$

with the quantity $\sigma_{\rm v,lin}$ being the linear theory estimate of the one-dimensional velocity dispersion, given by

$$\sigma_{\rm v,lin}^2 \equiv \int \frac{d^3\boldsymbol{p}}{(2\pi)^3}\frac{\mu_p^2}{p^2}\,P_{22}(p) \simeq \int \frac{dp}{6\pi^2}\,P_{\rm L}(p). \tag{195}$$

Here, the function C_1 is the same one as defined in Eq. (136) with (137), and is explicitly given by

$$C_1(\boldsymbol{k}_1,\boldsymbol{k}_2,\boldsymbol{k}_3) = \sum_{a,b,c=1}^{2}\mu_1^{2(a-1)}\mu_2^{2(b-1)}\mu_3^{2(c-1)}\,B_{abc}(\boldsymbol{k}_1,\boldsymbol{k}_2,\boldsymbol{k}_3). \tag{196}$$

A.2 D_2 term

From Eq. (150), the D_2 term is expressed in terms of the cumulants below:

$$D_2(\boldsymbol{k}_1,\boldsymbol{k}_2,\boldsymbol{k}_3) = \frac{1}{2}\int d^3\boldsymbol{r}_{13} d^3\boldsymbol{r}_{23}\, e^{i(\boldsymbol{k}_1\cdot\boldsymbol{r}_{13}+\boldsymbol{k}_2\cdot\boldsymbol{r}_{23})}\,\langle (j_4A_4+j_5A_5))^2\rangle_c$$
$$\times\Big[\langle A_1A_2\rangle_c\,\langle (j_4A_4+j_5A_5))A_3\rangle_c + \langle A_1A_3\rangle_c\,\langle (j_4A_4+j_5A_5))A_2\rangle_c + \langle A_2A_3\rangle_c\,\langle (j_4A_4+j_5A_5))A_1\rangle_c\Big]. \tag{197}$$

Substituting Eqs. (190)-(192) into the above expression, after lengthy calculation, we obtain

$$D_2(\boldsymbol{k}_1,\boldsymbol{k}_2,\boldsymbol{k}_3) = -\frac{f^2}{2}\{(k_1\mu_1)^2+(k_2\mu_2)^2+(k_3\mu_3)^2\}\,\sigma^2_{\rm v,lin}\,C_2(\boldsymbol{k}_1,\boldsymbol{k}_2,\boldsymbol{k}_3)$$
$$+ f^3(k_1\mu_1)(k_2\mu_2)(k_3\mu_3)\;J_2(\boldsymbol{k}_1,\boldsymbol{k}_2,\boldsymbol{k}_3) + f^3\;K_2(\boldsymbol{k}_1,\boldsymbol{k}_2,\boldsymbol{k}_3). \tag{198}$$

Here, the function C_2 is the same one as defined in Eq. (136) with (138). The explicit expressions for the functions C_2, J_2 and K_2 are given below:

$$C_2(\boldsymbol{k}_1,\boldsymbol{k}_2,\boldsymbol{k}_3) = -f\,(k_1\mu_1)\Big\{X(\boldsymbol{k}_2)Y(\boldsymbol{k}_3)+X(\boldsymbol{k}_3)Y(\boldsymbol{k}_2)\Big\}+\text{cyc.} \tag{199}$$

$$J_2(\boldsymbol{k}_1,\boldsymbol{k}_2,\boldsymbol{k}_3) = \int\frac{d^3\boldsymbol{p}}{(2\pi)^3}\,\frac{\mu_p^2}{p^2}P_{22}(p)\Big\{X(\boldsymbol{k}_2-\boldsymbol{p})Y(\boldsymbol{k}_1+\boldsymbol{p})+X(\boldsymbol{k}_1+\boldsymbol{p})Y(\boldsymbol{k}_2-\boldsymbol{p})\Big\}+\text{cyc.} \tag{200}$$

$$K_2(\boldsymbol{k}_1,\boldsymbol{k}_2,\boldsymbol{k}_3) = \int\frac{d^3\boldsymbol{p}}{(2\pi)^3}\,\frac{\mu_p^2}{p^2}P_{22}(p)\Big[\Big\{(k_1\mu_1)^2(k_2\mu_2)\,X(\boldsymbol{k}_2-\boldsymbol{p})+(k_1\mu_1)(k_2\mu_2)^2\,X(\boldsymbol{k}_1-\boldsymbol{p})\Big\}\,Y(\boldsymbol{k}_3)$$
$$+(X\;\leftrightarrow\;Y)\;\Big]+\text{cyc.} \tag{201}$$

with the functions X and Y defined by

$$X(\boldsymbol{p}) = P_{11}(p)+2f\,\mu_p^2\,P_{12}(p)+f^2\,\mu_p^4\,P_{22}(p), \tag{202}$$

$$Y(\boldsymbol{p}) = \frac{\mu_p}{p}\Big\{P_{12}(p)+f\,\mu_p^2\,P_{22}(p)\Big\}. \tag{203}$$

Appendix B Multipole expansion of redshift-space bispectrum

In Chap. 4.3 and 4.4, we have applied the multipole expansion to the redshift-space bispectrum, and evaluated its monopole and quadrupole moments. In this Appendix, we present the definition of our multipole expansion which differs from the one frequently used in the literature (e.g., [46, 66, 30, 61]). The newly defined bispectrum multipoles have several nice properties, which we will discuss below.

The redshift-space bispectrum is characterized as a function of five variables. Three of them characterize the shape of triangle, i.e., the length of two wave vectors $\boldsymbol{k}_1$ and $\boldsymbol{k}_2$, and the angle between them, $\theta_{12} \equiv \cos^{-1}(\hat{\boldsymbol{k}}_1 \cdot \hat{\boldsymbol{k}}_2)$. The two remaining variables describe the orientation of the triangle with respect to the line-of-sight. We denote them by ω and ϕ. In Ref. [46], the dependance of the orientation of the triangle are conveniently described by decomposing into spherical harmonics:

$$B_{\rm s}(\boldsymbol{k}_1, \boldsymbol{k}_2, \boldsymbol{k}_3) = \sum_{\ell=0}^{\infty} \sum_{m=-\ell}^{\ell} B_{\rm s}^{(\ell,m)}(k_1, k_2, \theta_{12}) Y_{\ell m}(\omega, \phi). \tag{204}$$

Similar to Ref. [46], we focus on the $m = 0$ multipoles, which correspond to averaging over ϕ. Then, the above equation leads to

$$\int_0^{2\pi} \frac{d\phi}{2\pi} B_{\rm s}(\boldsymbol{k}_1, \boldsymbol{k}_2, \boldsymbol{k}_3) = \sum_{\ell=0}^{\infty} B_{\rm s}^{(\ell)}(k_1, k_2, \theta_{12}) P_\ell(\mu), \tag{205}$$

were $P_\ell(\mu)$ is the Legendre polynomials. The variable μ represents the directional cosine of the orientation, $\mu = \cos\omega$. This is rewritten with

$$B_{\rm s}^{(\ell)}(k_1, k_2, \theta_{12}) = \frac{2\ell+1}{2} \int_{-1}^{1} d\mu\, P_\ell(\mu) \int_0^{2\pi} \frac{d\phi}{2\pi} B_{\rm s}(\boldsymbol{k}_1, \boldsymbol{k}_2, \boldsymbol{k}_3). \tag{206}$$

In the above, the bispectrum multipole, $B_{\rm s}^{(\ell)}$, is the quantity of our interest, but at this moment, Eq. (206) is ambiguous because we do not yet specify what is ω and ϕ. To describe the orientation of the triangle, a simple way is to choose $\boldsymbol{k}_1$ specifically, and define the orientation angle as $\mu = \cos\omega = \hat{\boldsymbol{k}}_1 \cdot \hat{\boldsymbol{z}}$ [46]. Then, we set ϕ to the azimuthal angle

around $\boldsymbol{k}_1$. In this case, however, the resultant bispectrum multipoles $B_{\rm s}^{(\ell)}(k_1, k_2, \theta_{12})$ are not fully symmetric under the permutation of order, k_1, k_2 and k_3.

Here, we give alternative definitions of ω and ϕ to preserve the symmetry of bispectrum multipoles. This is shown in Fig. 9. Given two vectors $\boldsymbol{k}_1$ and $\boldsymbol{k}_2$, we define the orientation of the triangle by the angle between line-of-sight direction and the vector normal to the triangle, i.e., $\hat{\boldsymbol{k}}_1 \times \hat{\boldsymbol{k}}_2$. That is,

$$\mu = \cos\omega = \frac{(\hat{\boldsymbol{k}}_1 \times \hat{\boldsymbol{k}}_2) \cdot \hat{\boldsymbol{z}}}{\sin\theta_{12}}. \tag{207}$$

The remaining angle ϕ may be defined as the azimuthal angle around the vector $\hat{\boldsymbol{k}}_1 \times \hat{\boldsymbol{k}}_2$. Since this is perpendicular to the plane of the triangle, we have

$$\cos\phi = \frac{\left\{\hat{\boldsymbol{z}} \times (\hat{\boldsymbol{k}}_1 \times \hat{\boldsymbol{k}}_2)\right\} \cdot \hat{\boldsymbol{k}}_1}{\sin\omega}. \tag{208}$$

One may suspect that the above definition still breaks the symmetry. Indeed, the vectors $\boldsymbol{k}_1$ and $\boldsymbol{k}_2$ can be arbitrarily chosen among three vectors, and we can even exchange $\hat{\boldsymbol{k}}_1 \longleftrightarrow \hat{\boldsymbol{k}}_2$. Then the orientation angle is changed to $\omega \to \pi - \omega$. Nevertheless, the bispectrum multipole $B_{\rm s}^{(\ell)}$ is invariant. This is because only the ℓ = even modes of the bispectrum become non-vanishing, and we have $P_\ell(\cos\omega) = P_\ell(\cos(\pi - \omega))$ for ℓ = even.

Once accepting the new definition, the measurement of the bispectrum multipoles is straightforward:

- In harmonic space, we first pick up the three density fields, $\delta(\boldsymbol{k}_1)$, $\delta(\boldsymbol{k}_2)$, and $\delta(\boldsymbol{k}_3)$, with the vectors satisfying $\boldsymbol{k}_1 + \boldsymbol{k}_2 + \boldsymbol{k}_3 = \boldsymbol{0}$. Here, labels of $\boldsymbol{k}_1$, $\boldsymbol{k}_2$ and $\boldsymbol{k}_3$ are arbitrary.

- Choosing the two vectors among the three, we calculate the directional cosine μ according to Eq. (207).

- Multiplying the bispectrum estimator by the Legendre polynomial $P_\ell(\mu)$.

- Repeating the above three steps for the same triangle configuration but with different μ, we average the *weighted* bispectrum estimator over μ. Further multiplying the averaged bispectrum by the factor $(2\ell + 1)/2$, we finally obtain the bispectrum multipole, $B_{\rm s}^{(\ell)}$, which is characterized by the length of two vectors, and the angle between them [see Eq. (206)].

Appendix C Review of TNS model

In this section, we present the PT model of redshift-space power spectrum which keeps the non-perturbative damping effect described by Ref. [11]. The strategy is similar to our improved bispectrum model, i.e. decomposing the contributions into non-perturbative part and the terms which can be evaluated with PT calculation, starting with the exact expression, Eq. (122).

Let us begin by rewriting Eq. (122) in the form

$$P^{(\mathrm{s})}(\boldsymbol{k}) = \int d\boldsymbol{r} e^{i(\boldsymbol{k}\boldsymbol{r})} \langle A_1 A_2 e^{j' A'} \rangle, \tag{209}$$

where the quantities A_1 and A_2 is similar to the bispectrum case shown at Eq.(125) and (126), while A' and j' are respectively defined by

$$A' = u_z(\boldsymbol{r}_1) - u_z(\boldsymbol{r}_2), \tag{210}$$

$$j' = -ik\mu f, \tag{211}$$

with $\mu = \boldsymbol{k} \cdot \hat{\boldsymbol{z}}/k$. Using Eq.(132), we express the moment given above in terms of the cumulants. To be specific, we assume that the vector fields given above are three components, i.e., $\boldsymbol{A} = \{A_1, A_2, A'\}$ and $\boldsymbol{j} = \{j_1, j_2, j'\}$. Then, taking the derivative two times with respect to j_1, j_2, we set $j_1 = j_2 = 0$. We obtain

$$\langle A_1 A_2 e^{j' A'} \rangle = \exp\left\{ \langle e^{j' A'} \rangle_{\mathrm{c}} \right\} \left[\langle A_1 A_2 e^{j' A'} \rangle_{\mathrm{c}} + \langle A_1 e^{j' A'} \rangle_{\mathrm{c}} \langle A_2 e^{j' A'} \rangle_{\mathrm{c}} \right]. \tag{212}$$

This equation is indeed what we want to derive, and the left hand side is exactly the same one as in the integrand of Eq. (209).

Here, we employ the proposition mentioned at Chap. 4.3. From the proposition (i), the overall exponential factor is factorized outside the integral. We have

$$\begin{aligned} P^{(\mathrm{s})}(k,\mu) \longrightarrow\ & D_{\mathrm{FoG}}(k,\mu) \int d\boldsymbol{r} \\ & \times e^{i\boldsymbol{k}\boldsymbol{r}} \left[\langle A_1 A_2 e^{j' A'} \rangle_{\mathrm{c}} + \langle A_1 e^{j' A'} \rangle_{\mathrm{c}} \langle A_2 e^{j' A'} \rangle_{\mathrm{c}} \right], \end{aligned} \tag{213}$$

We then expand the terms in the square bracket. Up to the second order in j', we obtain

$$P^{(\mathrm{s})}_{\mathrm{model}}(k,\mu) = D_{\mathrm{FoG}}(k,\mu) \int d\boldsymbol{r}\, e^{i\boldsymbol{k}\boldsymbol{r}} \times \left[\langle A_1 A_2\rangle_{\mathrm{c}} + j'\langle A_1 A_2 A'\rangle_{\mathrm{c}} + (j')^2\langle A_1 A_2\rangle_{\mathrm{c}}\langle A_1 A'\rangle_{\mathrm{c}} + \frac{(j')^2}{2}\langle A_1^2 A_2 A'\rangle_{\mathrm{c}}\right]. \tag{214}$$

The $\frac{(j')^2}{2}\langle A_1^2 A_2 A'\rangle_{\mathrm{c}}$ term in above expression do not contribute significantly. Finally, TNS model is given by:

$$P^{(\mathrm{s})}_{\mathrm{model}}(k,\mu) = D_{\mathrm{FoG}}(k,\mu) \int d\boldsymbol{r}\, e^{i\boldsymbol{k}\boldsymbol{r}}\Big[P_{11}(k) + 2f\mu^2 P_{12}(k) + f^2\mu^4 P_{22}(k) + A(k,\mu) + B(k,\mu)\Big]. \tag{215}$$

$$\begin{aligned} A(k,\mu) &\equiv j' \int d\boldsymbol{r} e^{i\boldsymbol{k}\boldsymbol{r}}\langle A_1 A_2 A'\rangle_{\mathrm{c}}, \\ &= -k\mu \int \frac{d\boldsymbol{p}}{(2\pi)^3}\frac{\mu_p}{p}[B_\sigma(\boldsymbol{p}, \boldsymbol{k}-\boldsymbol{p}, -\boldsymbol{k}) - B_\sigma(\boldsymbol{p}, \boldsymbol{k}, -\boldsymbol{k}-\boldsymbol{p})], \qquad (216) \\ B(k,\mu) &\equiv (j')^2 \int d\boldsymbol{r} e^{i\boldsymbol{k}\boldsymbol{r}}\langle A_1 A_2\rangle_{\mathrm{c}}\langle A_1 A'\rangle_{\mathrm{c}}, \\ &= (fk\mu)^2 \int \frac{d\boldsymbol{p}}{(2\pi)^3} F(\boldsymbol{p})F(\boldsymbol{k}-\boldsymbol{p}), \qquad (217) \\ F(\boldsymbol{p}) &\equiv \frac{\mu_p}{p}\left[P_{12}(p) + \mu_p^2 f P_{22}(p)\right]. \qquad (218) \end{aligned}$$

Here, we define the cross bispectrum:

$$\left\langle \theta(\boldsymbol{k}_1)\left\{\delta(\boldsymbol{k}_2) + f\frac{k_{2z}^2}{k_2^2}\theta(\boldsymbol{k}_2)\right\}\left\{\delta(\boldsymbol{k}_3) + f\frac{k_{3z}^2}{k_3^2}\theta(\boldsymbol{k}_3)\right\}\right\rangle_{\mathrm{c}} \equiv (2\pi)^3\delta_{\mathrm{D}}(\boldsymbol{k}_1+\boldsymbol{k}_2+\boldsymbol{k}_3)B_\sigma(\boldsymbol{k}_1,\boldsymbol{k}_2,\boldsymbol{k}_3). \tag{219}$$

The power spectrum is expanded by Legendre polynomials:

$$P^{(\mathrm{s})}_\ell(k,\mu) = \int_0^{2\pi}\frac{d\phi}{2\pi}\int_0^1 d\mu P^{(\mathrm{s})}(k,\mu)\mathcal{P}_\ell(\mu). \tag{220}$$